Summer 2003

Nonlinear Response and Fatigue Estimation of Aerospace Curved Surface Panels to Acoustic and Thermal Loads

Adam Przekop
Old Dominion University

NONLINEAR RESPONSE AND FATIGUE ESTIMATION OF AEROSPACE CURVED SURFACE PANELS TO ACOUSTIC AND THERMAL LOADS

by

Adam Przekop
M.Sc. January 1998, Warsaw University of Technology, Warsaw, Poland

A Dissertation Submitted to the Faculty of
Old Dominion University in Partial Fulfillment of the
Requirement for the Degree of

DOCTOR OF PHILOSOPHY

AEROSPACE ENGINEERING

OLD DOMINION UNIVERSITY
August 2003

Approved by:

_____
Chuh Mei (Director)

_____
Travis L. Turner (Member)

_____
Robert L. Ash (Member)

_____
Brett Newman (Member)

ABSTRACT

NONLINEAR RESPONSE AND FATIGUE ESTIMATION

OF AEROSPACE CURVED SURFACE PANELS

TO ACOUSTIC AND THERMAL LOADS

Adam Przekop

Old Dominion University, 2003

Director: Dr. Chuh Mei

This work presents a finite element modal formulation for large amplitude free vibration of arbitrary laminated composite shallow shells. The system equations of motion are formulated first in the physical structural-node degrees of freedom (DOF). Then, the system is transformed into general Duffing-type modal equations with modal amplitudes of coupled linear bending-inplane modes. The linear bending-inplane coupling is due to the shell curvature as well as unsymmetric lamination stacking. Multiple modes, inplane inertia, and the first-order transverse shear deformation for composites are considered in the formulation. A triangular shallow shell finite element is developed from an extension of the triangular Mindlin (MIN3) element with the improved shear correction factor. Time numerical integration is employed to determine nonlinear frequency of vibration. An iterative procedure to determine the judicious initial conditions for periodic panel response is developed and presented. By neglecting the inplane inertia effect, the general Duffing modal equations in functions of modal amplitudes of linear bending modes only are also formulated and presented. This approach is used for comparison of results with existing classic analytical methods. The

differences in characterizing a shallow shell behavior with modal amplitudes of coupled linear bending-inplane and bending only modes are demonstrated and discussed.

Then the finite element modal formulation for large amplitude random response of shallow shell panels to acoustic excitation and elevated temperature is presented. Reduced order integration is used to determine strains. Rainflow counting method and S-N curves are combined by means of damage accumulation theory to predict panel fatigue life. Factors contributing the softening effect, namely unsymmetrical lamination and curvature are investigated along with their impact on the fatigue life. Two types of excitation inputs are considered. Responses and fatigue life estimations to simulated band-limited Gaussian white noise and to in-flight recorded pressure fluctuation microphone data are presented and compared.

ACKNOWLEDGEMENTS

I would like to express gratitude and appreciation to my advisor Dr. Chuh Mei not only for his invaluable guidance, encouragement, advice, and patience through the entire course of this study, but also for being a great mentor during my time at ODU. I wish to sincerely thank my guidance and dissertation committee members, Dr. Travis Turner, Dr. Robert Ash, Dr. Brett Newman, and Dr. Thomas Alberts for their valuable time and constructive comments. I am also very grateful to Dr. Stephen Rizzi for his support during final preparation of my dissertation while working within his project.

Furthermore, I would like to thank my family members, and especially my parents, for words of encouragement that gave me lasting motivation to complete my doctorate degree.

Warm thanks to my circle of friends, Grzegorz Oleszczuk, Przemek and Arletta Praszczalek, and Slawek Cerbin, for companionship and great times away from my research.

Finally, I would like to thank all of my colleagues at ODU, especially Bob Carson, Xinyun Guo, Salim Azzouz, and Si-bok Yu for creating friendly and supporting environment.

Adam Przekop

August 2003

TABLE OF CONTENTS

LIST OF TABLES

LIST OF FIGURES

NOMENCLATURE

A	Element area
a	Panel length
[A]	Laminate membrane stiffness matrix
b	Panel width
[B]	Laminate membrane bending coupling stiffness matrix
[C]	Interpolation function matrix
D	Damage
[D]	Laminate bending stiffness matrix
E	Young's modulus
E[ ]	Expected value
f	Frequency
{F}	Surface traction
G	Kirchoff's modulus
H	Nondimensional thickness
[H]	Displacement function matrix
h	Panel thickness
K	Fatigue material property (experimental)
[K]	System linear stiffness matrix
[k]	Element linear stiffness matrix
[K1]	System first order nonlinear stiffness matrix
[k1]	Element first order nonlinear stiffness matrix
[K2]	System second order nonlinear stiffness matrix

[k2] Element second order nonlinear stiffness matrix

kur Kurtosis

[M] System mass matrix

{M} Moment resultant vector

m Mean value

[m] Element mass matrix

N Number of load cycles

n Number of cycles

[N1] First order nonlinear incremental system stiffness matrix

[n1] First order nonlinear incremental element stiffness matrix

[N2] Second order nonlinear incremental system stiffness matrix

[n2] Second order nonlinear incremental element stiffness matrix

{N} Force resultant vector

{M} Moment resultant vector

P Probability

{P} System force vector

{p} Element force vector

[Q] Lamina reduced stiffness matrix

$[\bar{Q}]$ Transformed lamina reduced stiffness matrix

{q} Modal coordinates vector

R Shell radius / Correlation function

{R} Shear force resultant vector

r Nondimensional radius

S Stress / Sectral density

skew Skewness

T Temperature

[T] Transformation matrix

t Time

tr Trace

u Inplane displacement along x-axis

v Inplane displacement along y-axis

W Virtual work / Normal deflection

w Transverse displacement

(x, y, z) Curvelinear coordinates

Greek symbols

α Thermal expansion coefficient / shear correction factor

β Fatigue material property (experimental)

Δ Incremental value

$\{\varepsilon\}$ Strain vector

$[\Phi]$ Modal matrix

$\{\Phi\}$ System eigenvector

$\{\gamma\}$ Shear strain vector

$\{\kappa\}$ Bending curvature vector

μ Up-crossing intensity

ν	Poisson's ratio
$[\theta]$	Slope matrix
ρ	Mass density
σ	Standard deviation
σ^2	Variance
$\{\sigma\}$	Stress vector
τ	Shear stress
ω	Frequency
ψ	Rotational displacement
ξ	Area coordinates
ζ	Modal damping

Subscripts and Superscripts

b	Out-of-plane (transverse and rotation)
c	Center / Cut-off
cr	Critical
ext	External
f	Fatigue life
h	Across the thickness
int	Internal
k	k^{th} layer
L	Linear

m	Membrane (inplane)
max	Maximum
min	Minimum
RFC	Rainflow counting
q	First order nonlinear in modal coordinates
qq	Second order nonlinear in modal coordinates
R	Curvature
s	Shear
T	Transposed
ΔT	Thermal
t	Transverse
x	Rotation around x-axis
y	Rotation around y-axis
$\overline{X}$	Modal value of quantity X
$\dot{X}, \ddot{X}$	First and second derivative of quantity X with respect to time

Subscripts and Superscripts

EL	Equivalent Linearization
FE	Finite Element
FSDT	First Order Shear Deformation Theory
OASPL	Overall Sound Pressure Level
PDE	Partial Differential Equation

PDF	Probability Density Function
PSD	Power Spectral Density
PTVC	Peak Through Valley Counting
RFC	Rainflow Counting
RMS	Root Mean Square
SPL	Sound Pressure Level
V/STOL	Vertical/Short Take-Off and Landing

1. Introduction

The surface skin panels of a modern aircraft and spacecraft are exposed to high levels of random pressure loads. These loads may be acoustic in nature due to the jet or rocket engine noise impingement. However, these loads may also be due to boundary layer pressure fluctuations or oscillating shock waves. Random pressure loads are very likely to be accompanied by elevated thermal environments that are produced by aerodynamic heating typical for flight with high Mach numbers. The combination of random pressure fluctuations and thermal loads that create very severe conditions for surface skin panels might also be a consideration for low speed aircraft, i.e. helicopters or Short/Vertical Take-Off and Landing (S/VTOL) designs powered by jet engines.

Sonic fatigue was one of the major design considerations for the F-35 Joint Strike Fighter that is currently going into production. There are also several other projects presently under development or conceptual studies that will encounter sonic fatigue. Among them is a group of Reusable Launch Vehicles (RLV), including X-43C, Crew Return Vehicle (CRV), and Liquid Fly Bach Booster (LFBB), as well as Next Generation Launch Technology (NGLT) and Quiet Supersonic Platform (QSP). All these vehicles will be exposed to high levels of random pressure fluctuation at elevated temperature.

It is known that curved panels may exhibit soft-spring behavior at large deflections unlike, hard-spring behavior for the flat plates. Therefore it would be expected that the root mean square (RMS) deflection, and subsequently strains, of a curved panel exhibiting soft-spring would be larger than those obtained from the linear structural theory. Large amplitude random response to and life estimation of curved panels exposed to acoustic excitations have not been investigated in the literature. The

objective of this work is to study non-linear random response of shallow shell panels to acoustic and thermal loads and to investigate the soft-spring effects on panel response and fatigue life. Complicated response characteristics being a result of nonlinear structural response to simultaneously applied pressure and thermal loads are anticipated. Therefore before imposing any kind of static, dynamic or random loading on a structure and investigating the interaction between the external loads and structural response, a fundamental study of free vibrations is very useful to help understanding the response characteristics.

1.1 Fundamental Studies – Free Vibrations of Shallow Shells

Shallow shells are common structural components in many fields of engineering. Various theories of shells have been described and outlined in many monographs, for example references.[1-3] A review of vibration of shallow shells covering the advances since 1970s is given by Liew et al.[4] Marguerre curved plate theory is used by Cummings[5] to study large amplitude vibration of a freely supported cylindrical shell segment. Perturbation and exact elliptic integral methods were employed for the panel frequency. Leissa and Kadi[6] derived the nonlinear partial differential equations (PDE) of motion for doubly curved shallow shells and studied curvature effects on period of free vibration. They employed the general elliptic equation and the Galerkin method for shells of rectangular boundary supported by shear diaphragms. Donnell's shell theory was applied by Hui[7] for simply supported cylindrical panels with geometric imperfections. Using the Galerkin procedure, the nonlinear vibration frequency was obtained from the Duffing equation with perturbation methods. Fu and Chia[8] presented a multi-mode solution for

nonlinear free vibration of anti-symmetric angle-ply shallow cylindrical panels with edges elastically supported against rotation. Effects of transverse shear deformation and geometric imperfection were included in their analysis. The harmonic balance method was employed in determining nonlinear frequency of vibration. The Donnell-Mushtari-Vlasov shell theory was used by Raouf and Palazotto[9] to model curved orthotropic cylindrical panels with simply supported edges. The spatial domain was discretized using the Galerkin procedure, and a perturbation method was used to evaluate nonlinear natural frequency. Kobayashi and Leissa[10] derived governing equations for nonlinear vibration of doubly curved shallow shells based on first order shear deformation theory. Applying the Galerkin procedure, the governing equations were reduced to an elliptic ordinary differential equation in time. Period of vibration for shells with rectangular boundaries supported by shear diaphragms was obtained using the Gauss-Lagrange integration method. Shin[11] studied the large amplitude vibration of symmetrically laminated moderately thick doubly curved shallow open shells with simply supported edges. By applying a Galerkin approximation, five governing equations of motion were reduced to a single nonlinear time-dependent differential equation. The Runge-Kutta time integration scheme was then employed to obtain the nonlinear frequency. Abe et al.[12] investigated nonlinear vibration of clamped laminated shallow shells by considering the first two modes (1^{st} symmetrical and 1^{st} antisymmetrical) and applying the Galerkin procedure to the equations of motion. The authors did not treat internal resonance between the first and the second modes, thus the second mode was neglected in determining nonlinear free vibration frequency for the first mode. The influence of the first mode on nonlinear vibration of the second mode was investigated, and the shooting

method[13] was employed for initial conditions. Pillai and Rao[14], and Bhimaraddi[15] were concerned about the softening effect in flat plates due to antisymmetrical lamination. Alhazza and Nayfeh[16] studied forced vibration of shells and found that solution characteristics may severely change as a function of the number of modes retained in the analysis. Their results, however, utilizing the multiple scale method is limited to relatively small nonlinearities.

All the aforementioned studies have shown both hard- and/or soft-spring behaviors for shallow shells with different geometries, materials and boundary conditions. Based on an exhaustive literature search, it is interesting to note that the classical analyses of large amplitude free vibration of shallow shells[5-12] have all neglected the inplane inertia terms due to mathematical difficulties. Also problems with obtaining the initial conditions for the steady periodic response resulted in the prevailing number of investigations using a single mode approximation.[5-7,9-11,14,15] Moreover, classical solutions were usually obtained for geometries based on rectangular plan-form, isotropic or orthotropic materials, and fully simply supported or fully clamped boundary conditions. By neglecting the inplane inertia terms and using classic analytical method for large amplitude free vibration of shallow shells, it leads to the case that the linear inplane modes are also dropped out from the analysis. The nonlinear Duffing modal equations are thus in functions of linear bending modal amplitudes only. For shallow shell structures, however, the linear bending and inplane modes are inherently physically coupled due to curvature, and to characterize their nonlinear large amplitude behavior with linear bending modes may yield inaccurate results.

The highly versatile finite element methods, on the other hand, have a capability to address coupled linear bending and inplane modes for flat unsymmetrically laminated composite plates (due to laminate stiffness $[B] \neq 0$). The nonlinear general Duffing equations as functions of modal amplitudes of coupled linear bending-inplane modes were reported by Shi et al.[17] Abdel-Motaglay et al.[18] studied panel flutter with inplane inertia neglected and expressed the nonlinear Duffing equations as functions of linear bending modal amplitudes. One of the objectives of the present work using the versatile finite element approach is to investigate the accuracy in predicting nonlinear vibration frequency of shallow shells by neglecting inplane inertia terms with a single bending mode approximation.

1.2 Historical Background on Random Response and Sonic Fatigue

Traditionally, structural design relies on deterministic analysis. Suitable dimensions, material properties, and loads are assumed, and an analysis is then performed to provide a more or less detailed description of the structure. However, fluctuations of the loads and variability of the material properties contribute to an uncertainty of the analysis and statistical tools need to be employed to assess a risk of failure. The term *fatigue* is understood in a broad sense, including crack nucleaction and growth to the final failure under cyclic and/or sustained loads and actions. In addition to the classic high-cycle and low-cycle fatigue, such phenomena as creep fatigue, corrosion fatigue, stress corrosion cracking, etc., are also considered to be fatigue processes. Fatigue and related phenomena are the most frequent causes of structural component failures that result in the

interruption of operation and the accompanying economic loss up to major accidents with disastrous consequences.[19]

The systematic study of fatigue was initiated by Wöhler, who in the period between 1858-1860 performed the first systematic experimentation on damage to materials under cyclic loading. In particular, Wöhler introduced the concept of the fatigue curve, i.e., the S-N diagram where a characteristic magnitude of cyclic stress is plotted against the cycle number until fatigue failure.[19]

In the past, aircraft designers were aware of the fatigue phenomena but lacked detailed understanding and knowledge of the underlying mechanisms. In the late nineteen fifties, incidents were reported in which aircraft structures close to high intensity jet exhausts suffered minor damage.[20,21] Skin cracking was noticed and failures of small cleats and internal support structure occurred in a few cases. These incidents alerted industry and research centers to the possibility of problems as the performance of aircraft and jet engines increased. Several aircraft manufacturers and the research centers set up comprehensive tests on large parts of aircraft structures in which it was possible to reproduce representative structure around the region of maximum noise intensity. In parallel, theoretical work and experiments on simple structures such as rectangular plates and shells had begun. Simple theoretical models of the structure and the excitation process were proposed. However, theoretical and computational tools available at that time were insufficient to predict fatigue life for a complex airframe structure subject to broad-band frequency random pressure fluctuations, very often exhibiting non-Gaussian and non-white characteristics. The lack of a comprehensive theoretical approach led to the development of design guides and data sheets for industry. Extensive programs

aimed to develop those tools were sponsored by USAF[22-26] and Advisory Group for Aerospace Research and Development (AGARD).[27-30] USAF sponsored programs led to design of nomographs for every type structure in common use, while activity sponsored by AGARD provided a larger range of test results but focused on the primary structure.

The need for the abovementioned development - which took place between the mid fifties and early seventies - was primarily due to the rapidly increasing noise of jet engines as the required thrust increased. In the early seventies the higher bypass jet engine configurations allowed designers to boost the power of the jet turbines further without increasing the noise level. This factor caused some stagnation in the field of sonic fatigue. New interest arose during the mid eighties with the first attempts to introduce composite materials into the airframe structure. Also aerodynamic heating brought higher operating temperatures to some aircraft and spacecraft designs. Thermal effects had to be added to the fatigue life estimation. The main advantage of laminated structures is their strength to weight ratio. Better structural efficiency of composite materials often yields higher deflections under the external loads. Large deflections combined with an elevated temperature environment expose the structure to very severe working conditions. Also in many cases the possibility of thermal buckling - which dramatically influences composite surface panel response - needed to be investigated. Some new design guidelines were created,[31] but due to variety of possible layered structure configurations it became apparent that a comprehensive semi-empirical approach cannot be fully and efficiently developed.

This turned the attention of researchers to available and improved computational techniques. The nonlinear random response of isotropic plates subjected to a uniformly

distributed truncated Gaussian white noise was reported by Arnold and Vaicaitis.[32] The Monte Carlo numerical simulation was applied to the nonlinear modal equations obtained from the von Karman large deflection plate equations with the application of Galerkin's method. The extension of this work into composite plates was presented by Vaicaitis and Kavallieratos.[33] Nonlinear random response of composite plates of arbitrary shape in an elevated thermal environment were investigated by Mei and Chen[34] using the equivalent linearization (EL) method. Mei et al.,[35] and Dhainaut,[36] using a FE modal formulation and numerical simulation investigated random response and fatigue life of composite panels subjected to white and non-white excitations. Lee[37] improved the EL technique for stochastic Duffing oscillators. Also Rizzi and Muravyov[38,39] used the EL method and commercial FE codes for random response prediction of geometrically nonlinear structures. McEwan et al.[40] combined a backward elimination regression procedure with the singular value decomposition technique to allow identification of an accurate and parsimonious system model. Experimental results for flat isotropic and composite panels to thermal and vibration shaker excitation were reported by Ng and Clevenson,[41] Murphy,[42] and Istenes et al.[43]

1.3 Random Response to Combined Acoustic and Thermal Environment

It is known that curved panels may exhibit soft-spring behavior at large deflections unlike, hard-spring behavior for flat plates. Therefore, would be expected that the root mean square (RMS) deflection, and subsequently strains, of a curved panel exhibiting soft-spring would be larger than those obtained from the linear structural theory. Large amplitude random response and life estimation of curved panels to

acoustic excitations have not been investigated in the literature. The objective of this work is to study non-linear random response of shallow shell panels to acoustic and thermal loads and to investigate the soft-spring effects on panel response and fatigue life.

1.3.1 Acoustic Loads

High frequency random pressure fluctuations of the acoustic type on aerospace structures are generally caused by the turbulent mixing in a high-speed jet efflux. Also a turbulent boundary layer and oscillating shock waves or flow buffeting can be recognized as being pseudo-acoustic loads.[21]

1.3.1.1 Jet and Rocket Pressure Loads

In this area researchers were primarily concerned about the field pressure caused by high velocity jet efflux and sound radiation. The first approach of a quantitative description of this phenomenon was made by Lighthill in 1952.[44,45] The statistical description of jet/rocket efflux gives a relatively smooth power spectrum with a peak between 100 and 600 Hz. The resonant frequency is inversely proportional to the diameter of the nozzle. The magnitude is approximately proportional to the fourth power of the jet velocity. A more accurate description requires knowledge of pressure distribution over the structural surface. The most common and convenient way of describing the spatial pressure distribution is the one by means of cross-spectral density over the distance from the surface. At the turn of the sixties and seventies, the increased interest in Vertical/Short Take-Off and Landing configurations (VTOL/STOL) resulted in research directed towards this field. Lansing et al.[46] considered the jet exhaust impinges

on the structure or the ground and enhancement of the pressure field on the aircraft structure due to this factor. There was shown that in the extreme cases the pressure loading on the aircraft surface could almost be doubled. More on the ground reflection effects was presented by Scholton.[47]

1.3.1.2 Turbulent Boundary Layers

The pressure fluctuations under a turbulent boundary layer are also a potential source of structural damage. According to the results presented by Coe and Chyu[48,49] for supersonic flow, the overall pressure level is not usually as high as that for the extreme jet cases and the spectrum is relatively flat out to a high frequency. Comparison with subsonic flow[50] measurements and some supersonic flow work[51] show a trend of decreasing pressures with increasing Mach numbers.

1.3.1.3 Separated Flow and Oscillating Shocks

Separated flow, cavities and oscillating shocks can also contribute to structural fatigue. This area is still not thoroughly explored. Some model-scale experimental results have been presented by Coe and Chyu.[48,49] As the normal boundary layer flow is disturbed, the mean pressure increases and the form of the spectrum changes. In the low frequency range the magnitude of the mean pressure increment by up to three orders can be observed. Beneath oscillating shock waves, further magnitude increments of one order are measured.

1.3.2 Thermal Loads

Aerothermal loads exerted on the external surface of the flight vehicle can be divided into pressure, skin friction (shearing stress), and aerodynamic heating (heat flux).[52] Pressure and skin friction play important roles in aerodynamic performance of the vehicle, but aerodynamic heating creates a predominant thermal load at high speeds. Elevated temperatures can degrade elastic properties (i.e. Young's modulus) of the material, decreasing their ability to withstand design loads. Simultaneously, the allowable stresses are reduced and time dependent material behavior such as creep comes into play. In addition, thermal stresses are introduced because of the restrained thermal expansion or contraction. Such stresses increase deformation, change buckling loads and alter flutter behavior.

An estimation of the surface aerodynamic heating has been much of a challenge for researchers over the decades. Under the assumption that the atmosphere is a continuum the set of Navier-Stokes (N-S) equations need to be solved. For two-dimensional flow, the N-S equations governing viscous, compressible flow are a set of four nonlinear partial differential equations (PDE) with mixed hyperbolic, parabolic, and/or elliptic behavior. A solution to the N-S equations with appropriate boundary conditions provides distributions of the density, two velocity components, pressure and temperature throughout the fluid. Subsequently, Fourier's Law can be used to compute aerodynamic heating. First approaches for approximated aerodynamic heating solutions, were proposed by Van Driest[53] and Truitt[54] at the end of nineteen fifties.

Sonic fatigue is a fluid-structure interaction problem requiring simultaneous solution of the N-S equations and the structural dynamic equations. For large amplitude

deflections, the shape of the structure defining the fluid-structure interface is not known a priori, hence must be determined from the solution of the fluid and structure equations. A common approach is to decouple structural and fluid parts of the problem and still retain sufficient model fidelity. For a hypersonic flow a good approximation is achieved by applying so-called von Karman-Herrmann-Chu plate equation under prescribed pressure and temperature variations.[55] Although much progress has been made recently to solve the coupled fluid-structural problem, this approach is not in focus of this study.

To appreciate the thermal challenges let us compare some numerical trends. The maximum temperature recorded on the surface of X-1B plane traveling at M=1.94 (1957) was 185°F.[56] Only 8 years later, in 1965, the X-15 plane traveling at M=5.0, which is considered hypersonic flow, produced a surface temperature of 1325°F.[57] The maximum temperatures on the leading edges of the Space Shuttle (first flight in 1981) during re-entry exceeded 2650°F.[58] Researchers now developing the RLV-class vehicles must consider temperatures on the order of 4000°F.

1.3.3 Acoustic vs. Thermal Loads Over A Mission

Dealing with simultaneous loads introduces the question of loading variation over the duration of the flight. Will the most severe thermal loads occur at the same time when the acoustic pressure peaks? And if not, where is the maximum of the resultant function? In order to attempt to answer these questions one needs to consider separately the missions' profiles for the following air/spacecraft: (i) traditional rocket/jet engine design, (ii) VTOL/STOL configurations, (iii) suborbital flight vehicles, i.e. High Speed Civil Transport (HSCT), Reusable Launched Vehicles (RLV), Liquid Fly Back Boosters

(LFBB), and Crew Return Vehicles (CRV).

1.3.3.1 Traditional Rocket / Jet Powered Design

For the traditional rocket/jet powered designs, maximum acoustic loads occur for a very short time just before the initiation of roll of an aircraft. As soon as the vehicle begins to move the relative velocity of the jet stream in the stationary air reduces steadily which subsequently reduces surface pressure. Since the pressure is proportional to the fourth power of the relative velocity, the decrease is very rapid. The severe sonic environment is present usually for no more then 20 seconds.[20] Over such a short period of time the hot exhaust gases do not have enough time to heat up the structure significantly. Typical temperature and acoustic load variations are shown in the Figure 1.1.

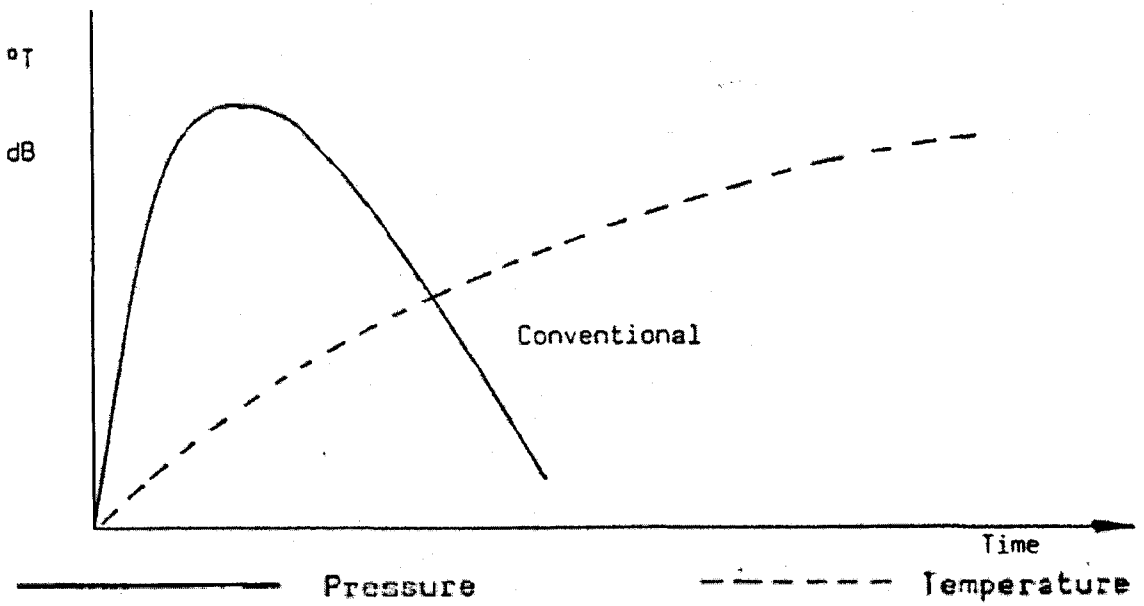

Figure 1.1 Typical Temperature and Acoustic Load Variation For Classical Rocket/Jet Powered Aircraft[20]

1.3.3.2 VTOL/STOL Configurations

The situation described in the previous section is not always the case for the Vertical/Short Take Off and Landing (VTOL/STOL) aircrafts. The take-off phase takes considerably longer so the maximum acoustic and thermal loads can coincide. Another possible state in flight where these conditions can occur is steady hover (zero vertical and horizontal speed, not necessarily involving take-off nor landing). Typical temperature and acoustic loads variation is shown in the Figure 1.2.

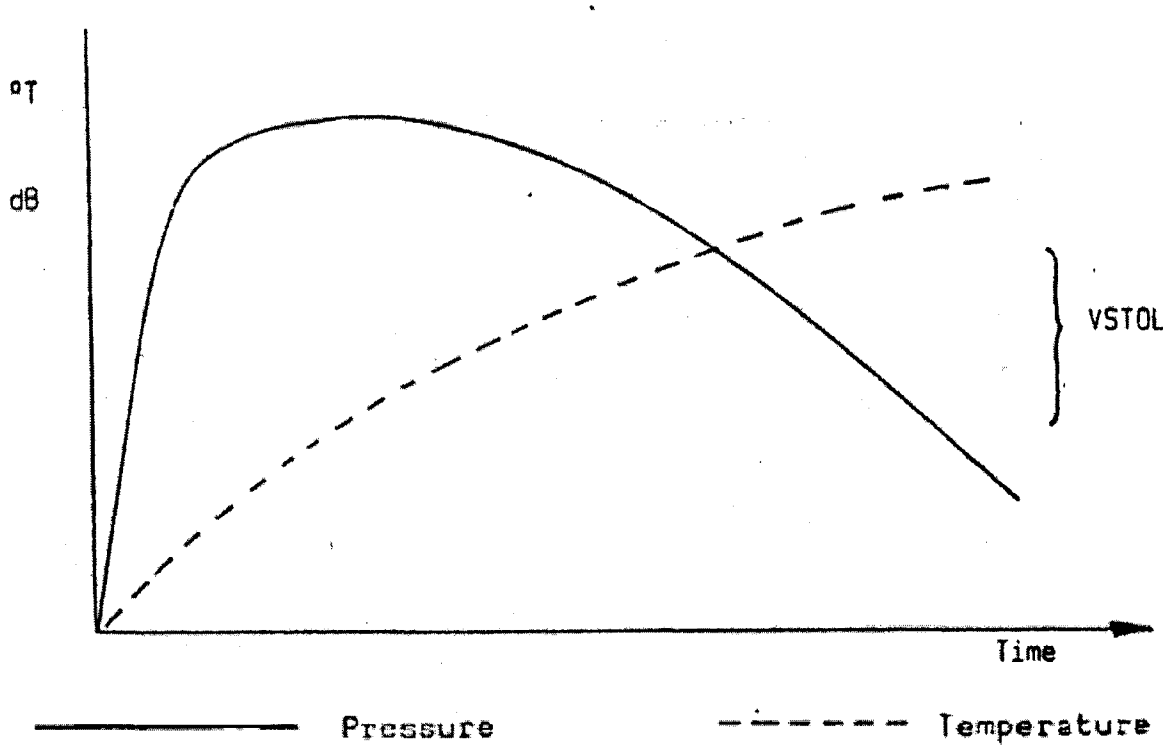

Figure 1.2 Typical Temperature and Acoustic Load Variation for VTOL/STOL Aircraft[20]

1.3.3.3 Suborbital and Reusable Spacecraft

For the new design of suborbital and reusable spacecraft the take-off/launch conditions conform with the traditional configuration described in Section 1.3.3.1.

Additional design considerations arise with the ascent/re-entry involving high levels random pressure fluctuation and extreme thermal conditions. Typical temperature and random pressure load variations are shown in Figure 1.3.

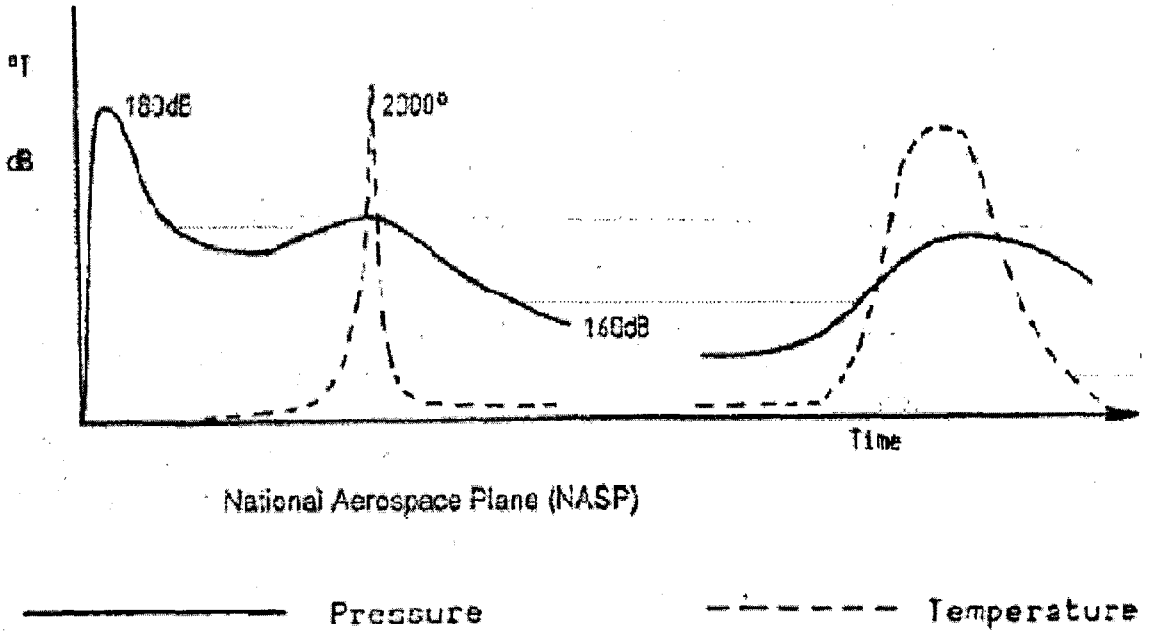

Figure 1.3 Typical Temperature and Acoustic Load Variation For Suborbital/Reusable Launcher Spacecraft[20]

1.4 Analytical Techniques for Predicting Random Response

This section, in addition to the historical background given in Section 1.2, presents some analytical methods not introduced thus far or described before in a rather brief manner. This section focuses on the principle of the method, rather than its placement in the chronological order, and only for that reason some information might seem to be repeated.

1.4.1 Fokker-Planck-Kolmogorov Equation Approach

The Fokker-Plank-Kolmogorov (FPK) equation approach gives an exact solution for a restricted class of simple problems. If the excitation is sufficiently broadband, modeling of the response as a multi-dimensional Markov process is feasible. The most general extension of the FPK equation approach to nonlinear second order equations was due to Caughey.[59]

The FPK equation can be derived by applying the Ito differentiation rule to an arbitrary function of the diffusion process. An alternative way of deriving the FPK equation can be based on the Smoluchowski-Chapman-Kolmogorov equation.

Most of the available exact solutions of the FPK equation correspond to the case in which the transition probability density becomes time-invariant and independent of the initial condition in the limit. Obtaining exact solutions for the non-stationary FPK equation is much more difficult. Available results are based on Fourier transforms and the method of separation of variables.[60] Difficulties in finding the transitional Probability Density Function (PDF) with the FPK method led to the development of a number of the approximate solutions that are presented below.

1.4.2 Perturbation Approaches

The perturbation method has been used extensively for the solution of weekly nonlinear systems. First applications of the perturbation method to determine the approximate response statistics of weakly nonlinear systems subject to random excitation are due to Lyon[61] (string, 1960) and Crandall[62] (discreet 1 DOF system, 1963), and Tung et al.[63] (discreet 2 DOF system).

The principle of the method assumes that the solution is sought as an expansion in a power series of some small parameter. Technically, the perturbation method can be used to estimate the response to any order of the above mentioned parameter. In practice, however, results are obtained to the first order of the parameter because the algebra for higher order estimates becomes very complex. The validity of the expansion of the response in powers of the parameter requires convergence of the series, which must depend upon the magnitude of the parameter itself. A rigorous proof of the convergence is not available. However comparison of the solutions with the results obtained by other methods shows that the perturbation method gives satisfactory results for the parameters $<<1$.[64] Since the value of this parameter is related to the magnitude of the nonlinearity of the system the method does not provide sufficient accuracy for systems exhibiting strong nonlinearities.[65]

Figure 1.4 compares the accuracy of the solutions obtained with perturbation and equivalent linearization techniques with the exact analytical solution. The x-axis represents the ratio between cubic (μ) and linear (k) stiffness terms coefficients of a hardening system, which is a measure of how strong the nonlinearity of the system is. The y-axis represents the ratio of variances of the nonlinear and linear solutions. Figure 1.4 shows that the perturbation technique will not give an accurate solution for systems exhibiting strong nonlinearities. The accuracy of the results obtained with the equivalent linearization technique is acceptable.

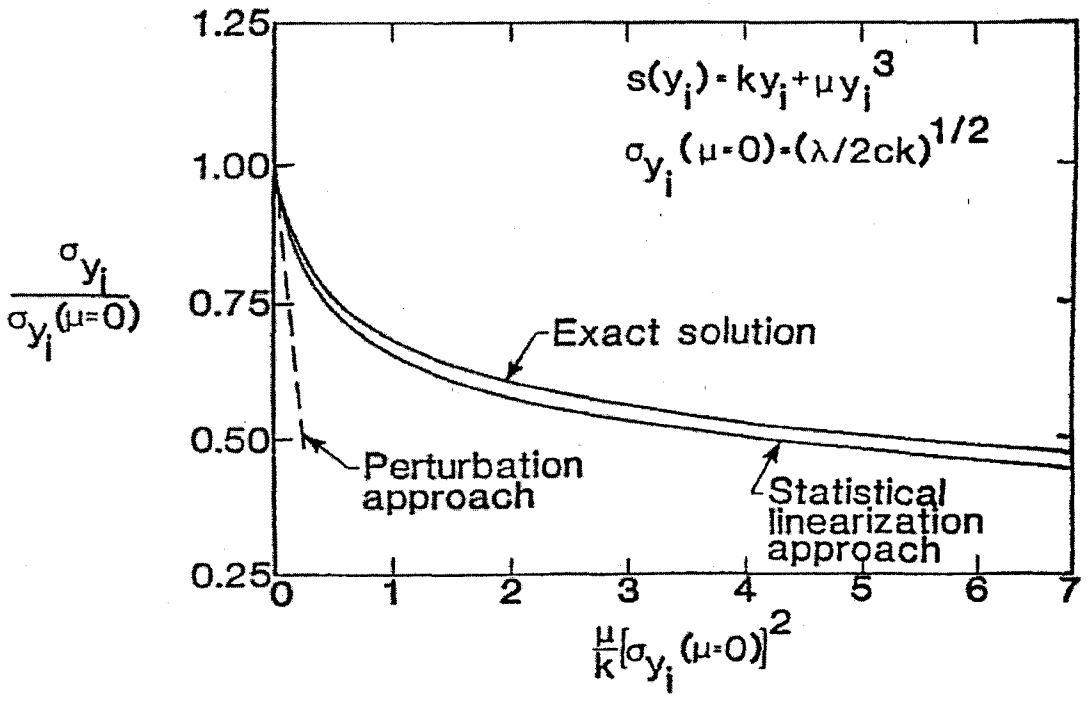

Figure 1.4 RMS Responses of Hardening System by Perturbation, EL, and FPK Approaches

1.4.3 Equivalent Linearization Approaches

The Equivalent Linearization (EL) method was developed by Krylov and Bogoliubov in 1943 for deterministic vibration problems. For the first time the method was applied to random excitation by Booton[66] in 1954. While Booton used an electrical circuit as a physical model to be investigated, first application for the acoustic excitation was due to Caughey[67] in 1963. The method was expanded into multi-modes by Atalik and Utku[68] in 1976. In 1980 Sakata and Kimura[69] developed the procedure to calculate non-stationary response due to non-white excitation, but the assumption of Gaussian distribution could not be dropped. The normal distribution assumption was needed in order to estimate higher order statistical moments.

In general, the concept of the EL method is to replace a nonlinear system with its linear equivalent such that the difference between two systems is minimized. The method is capable of handling all kinds of nonlinearities including inertia, damping and stiffness. As for the forcing function, similar to that mentioned before, the method can handle non-white Gaussian excitations.

1.4.4 Numerical Simulation

The Monte Carlo Simulation (MCS) for random vibration problem was developed by Shinozuka[70] in 1972 and extended subsequently with help of his coworkers into a wide range of structural nonlinearities.[71,72] Using the large number of generated sample excitations, the corresponding response samples are calculated. These response samples are then used to estimate corresponding response statistics. The method is capable of handling both stationary and non-stationary responses, but the computational cost needs to be recognized as a major drawback of this approach.

1.4.5 Partial Differential Equation (PDE) / Galerkin Method

From the mid eighties, the Galerkin method (PDE and modal approach) was widely applied in conjunction with the numerical simulation (i.e. Monte Carlo Method) for prediction of the response of isotropic[32,73,74] and symmetrically laminated composite panels.[33] PDE/Galerkin method was also used in conjunction with the Equivalent Linearization (EL) method[37,55,75] for isotropic structure. Although the significant progress in the analytical approaches, the use of PDE/Galerkin approach was still limited to simple panel platform of rectangular shape and simple boundary condition. These

limitations could be easily waived with use of the Finite Element (FE) method.

1.5 Fatigue Life of an Aircraft/Spacecraft Structure

Despite an extensive search no reference was found regarding analytical estimation of fatigue life of shallow shell structure to combined acoustic and thermal loads. The available literature is limited to flat panels, and was reported i.e. by Vaicaitis,[73] Dhainaut,[36] and Chen et al.[76]

1.5.1 High-Cycle vs. Low-Cycle Fatigue

Aircraft/Spacecraft structures are exposed to two different kinds of cyclic loading. So-called Low-Cycle Fatigue (LCF) is associated with a single mission performed by the vehicle including taxing, take-off, climbing, cruise, descending/re-entry and landing where for instance, the fuselage can be thought of as working as a pressurized vessel. High-Cycle Fatigue (HSF) is associated with occurrences such as gusts or control excitations, which takes place many times during one mission. The transient range of cycles between those two categories of fatigue can be placed usually from 10^1 to 10^5 cycles. There is enough historical evidence to prove the statement that both processes can cause fatal consequences.

1.5.2 S-N Curves

The concept of Stress-Life Diagrams (S-N Curves) has been established by Wöhler in the middle of the 19th century. The diagrams present stress (S) versus number of cycles (N) needed to cause the failure. Since fatigue is a probabilistic process, several curves are made available for different testing arrangements. Each curve corresponds to a

particular reliability of the test, which is, i.e., a function of the number of specimens that have been tested. Those curves are known as S-N-P curves, where P stands for probability of failure. Graphically, a typical S-N curve can be represented as shown in Figure 1.5. K and β are material properties and in fact they are approximated by their expected values $E[K]$ and $E[\beta]$, respectively. S_∞ is the fatigue limit and below the value no failure will be encountered regardless of the number of applied cycles.

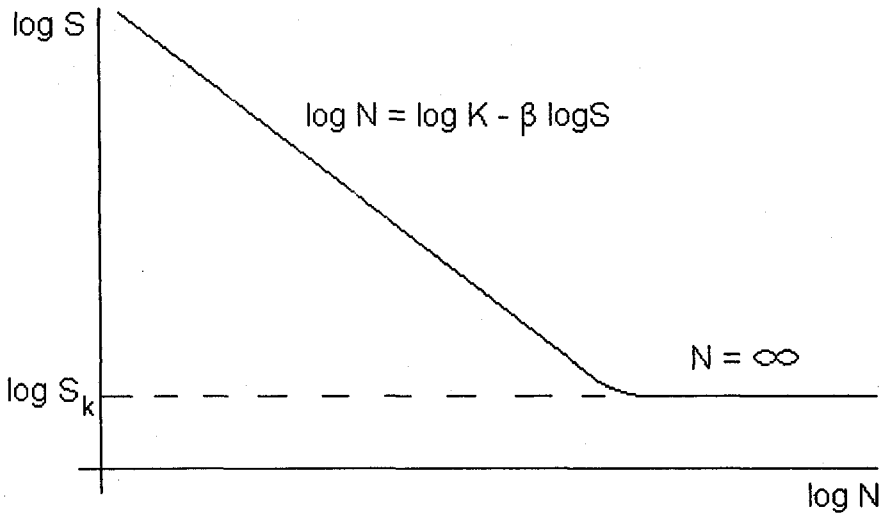

Figure 1.5 S-N Curve

Note here that the S-N curve does not reflect any physical phenomena occurring in the material structure and represents a purely empirical approach to specimen damage.

1.5.3 Peak Counting Methods

Since large amplitude response characteristics of a thin-walled structure in an elevated thermal environment are expected to be non-Gaussian, the frequency domain methods of estimating the fatigue life could not be applied. The crucial step in estimating the fatigue life based on maximum strain time history is the selection of a peak counting method.[77] For that reason this section is treated with particular attention.

The simplest peak counting method assumes that characteristic points of the response time history (of strains or stresses) are all the maximum values of the response and all the minimum values of the response (Figure 1.6). The restriction may be made that only maximum values above the mean load and minimum values below the mean load are counted.

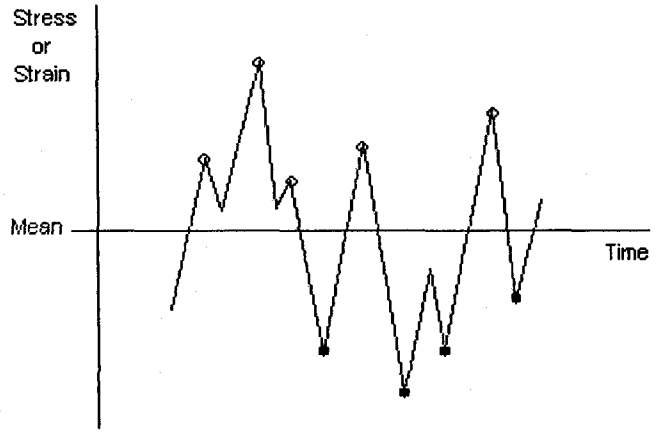

Figure 1.6 The Simple Peak Count Method

Among more sophisticated methods of peak counting[78] one could list: (i) The Range Count Method, (ii) The Mean-Crossing Peak Count Method, (iii) The Range-Mean Count Method, (iv) The Range-Pair Count Method, (v) The Level-Crossing Count Method, (vi) The Fatiguemeter Count Method, and (vii) Rainflow Counting Method.

The Mean-Crossing Count Method assumes that between two successive mean-crossing only one count is made (Figure 1.7).

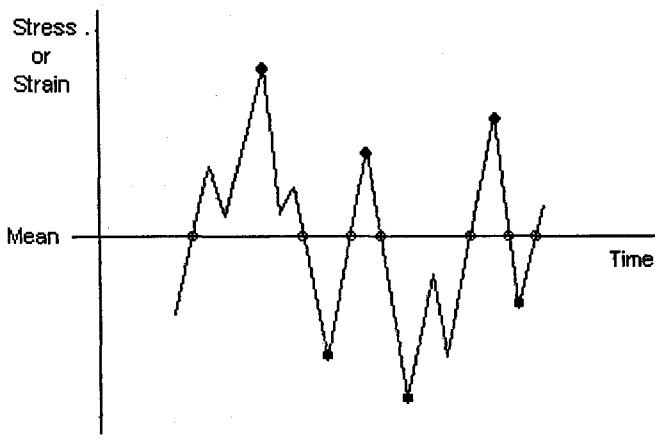

Figure 1.7 The Mean-Crossing Peak Count Method

For the Range Count Method a range is defined as the difference between two successive peak values of the variable *y*, the range being positive when a minimum is followed by a maximum and negative if the inverse is true. The method is illustrated in Figure 1.8. Results may be presented as *h(r)* or *H(r)*.

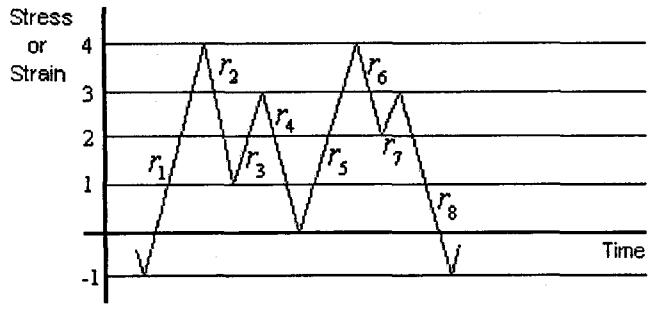

Positive Ranges:
$r_1 = 5, r_3 = 2, r_5 = 4, r_7 = 1$

Negative Ranges:
$r_2 = -3, r_4 = -3, r_6 = -2, r_8 = -4$

Figure 1.8 The Range Count Method

In contrast with both previous methods this method gives direct information on response variations, which have actually occurred. However, it fails to give information on the magnitude of the response peaks. This latter remark does not apply to the Range-Mean Counting Method. For this method, range values, r, are counted in the same way as for the Range Counting Method. However, for each range the corresponding mean value m of this range is counted in addition to the value of r. Figure 1.9 illustrates the procedure. The number of exceedings $H(r,m)$ is associated with a two-dimensional distribution function. Consequently it should contain more information than the analytical methods based on one-dimensional distribution function.

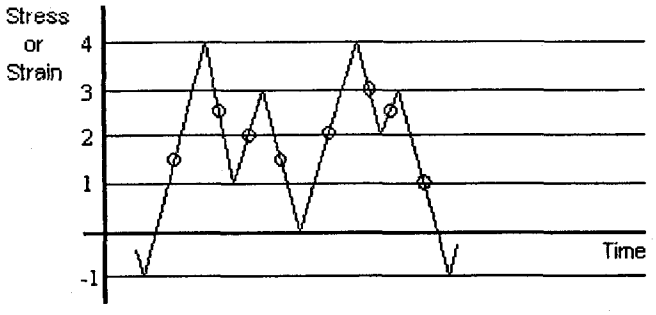

Results of Counts:
$r = 5, \quad m = 1.5$
$r = -3, \; m = 2.5$
$r = 2, \quad m = 2$
$r = -3, \; m = 1.5$
$r = 4, \quad m = 2$ *etc.*

Figure 1.9 The Range-Mean Count Method

For the Range-Pair Count Method, ranges are counted in pairs. The range r has meaning in terms of the response variation or increment starting from a minimum or a maximum of the response. Each range pair to be counted consists of a positive increment exceeding a prescribed value combined with the next exceeding of a negative response increment of the same magnitude. Figures 1.10a and 1.10b illustrate the counting method for a small and a large value of r, respectively. Intermediate response variations are

disregarded (grayed fields in the Figure 1.10b). The Strain-Range-Counter developed by Vickers Aircraft Ltd. is counting in accordance to this method.

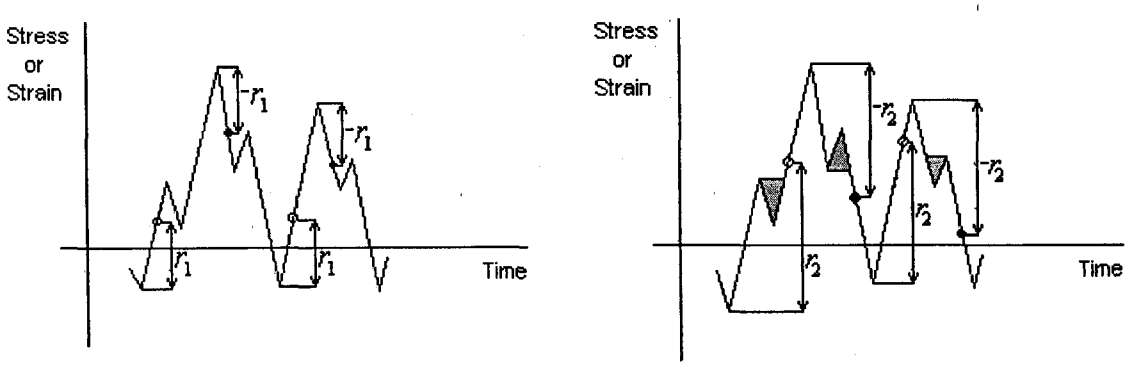

∘ - First condition for count, • - Second condition for count

Figure 1.10 The Range-Pair Count Method: (a) r_1 - Small Range, (b) r_2 - Large Range

For the Level-Crossing Count Method each time the varying response crosses a certain response level with a positive slope a count is made. This is done for number of response levels. The method is illustrated in Figure 1.11.

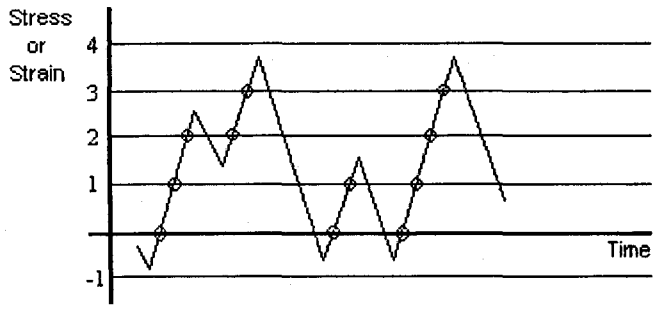

Figure 1.11 The Level Crossing Count Method

In the Fatiguemeter Count Method the principle of counting is much the same as for the Level-Crossing Count Method. Above and below the mean response the crossing of some pre-set levels are counted. However, in order to prevent small response variations from producing the counts a second condition must be met. To complete a count of a level crossing at a level above the mean response the response must have decreased to a lower pre-fixed level. This is illustrated in Figure 1.12. The procedure of completing a count of a level at another prefixed level implies that certain response variations are disregarded. Such variations are indicated in Figure 1.12 as grayed areas.

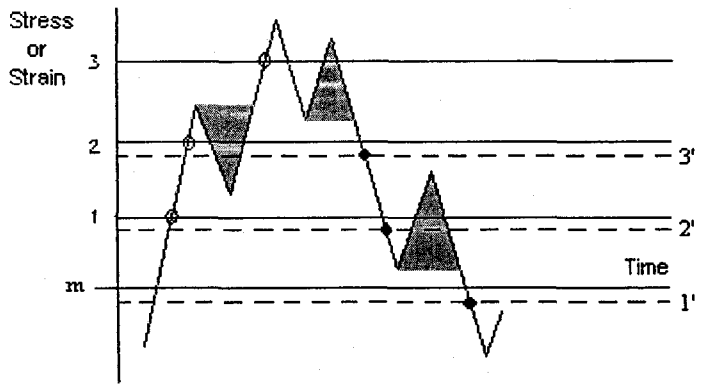

o - Counting Level Energized (1, 2, 3),
• - Counting Completed at Lower Level (1', 2', 3')

Figure 1.12 The Fatiguemeter Count Method

For the Rainflow Counting (RFC) Method, from each local maximum M_i one shall try to reach above the same level, in the backward (left) or forward (right) directions, with as small a downward excursion as possible. The minima, m_i^- and m_i^+ on each side are defined. That minimum which represents the smallest deviation from the maximum M_i is defined as the corresponding rainflow maximum m_i^{RFC}. The concept is illustrated in Figure 1.13.

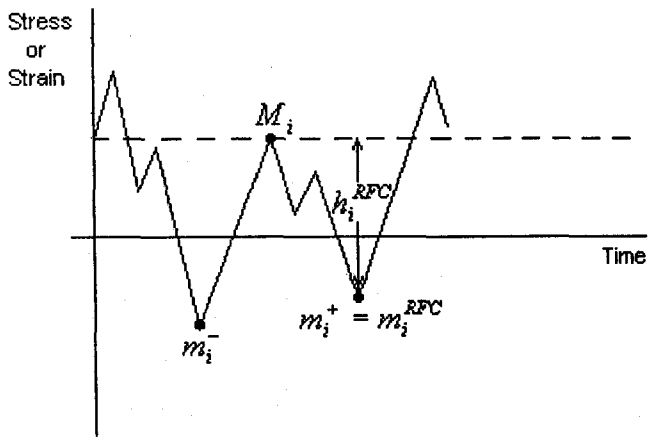

Figure 1.13 Rainflow Count Method

The RFC method was originally developed by Matsushi and Endo.[79] Later on, a new explicit definition of RFC redeveloped by Rychlik[80] became more popular.

The comprehensive study of the performance of counting methods to be applied for the fatigue life prediction has been conducted by Dowling.[77] Based on the experimental evidence it was concluded: "... the counting of all closed hysteresis loops as cycles by means of the rainflow counting method allows accurate life predictions. The use of any method of cycle counting other than range pair or rainflow methods can result in inconsistencies and gross differences between predicted and actual fatigue lives".

1.5.4 Cumulative Damage

As described in Section 1.5.2, the S-N curves provide the answer to the question how many cycles a structural member can withstand under certain level of applied loading. However, as demonstrated in Section 1.5.3 an applied load, represented by peaks counted by one of the methods introduced, might have a complicated time history. The question arises on how to account for complicated time histories where the amplitude

of stress varies with time. In other words, a model for the damage accumulation is needed.

The cumulative damage is a measure of a loss of a structure's ability to withstand applied cyclic loads. Most generally this concept can be postulated such that the cumulative damage increment in time, dD(t)/dt, is a function of load applied to the structure, S(t), and the cumulative damage experienced before this load, D(t).[81,82]

$$\frac{dD(t)}{dt} = f[D(t), S(t)] \tag{1.1}$$

However, fatigue damage theories were investigated[83] for step fatigue tests, with the conclusion that Palmgren-Miner theory[84,85] was as adequate as the more complex theories. Although fatigue theories make interesting studies, the Palmgren-Miner's theory is the easiest to use and to understand, and is suitable for application to the acoustic fatigue problem. The concept of Palmgren-Miner linear damage accumulation theory can be summarized as follows: for each stress amplitude the contribution to the total damage is calculated. For example, if stress amplitude S_k requires $N(S_k)$ cycles for the damage to occur, the contribution to the total damage due to n_k cycles at this amplitude, where $n_k < N(S_k)$, is equal $n_k / N(S_k)$, and the failure occurs when value of damage, D, reaches unity. Note that Eq. (1.1), when simplified by the assumption that the damage increment is independent on the total damage itself $\frac{dD(t)}{dt} \neq f[D(t)]$ and solved with zero initial conditions $D(0) = 0$, reduces to the Palmgren-Miner theory. Introducing the S-N curve into Palmgren-Miner damage accumulation theory the fatigue life can be predicted in the time domain.

Very comprehensive reviews of damage accumulation theories for fibre-reinforced composite materials were presented by Degrieck and Van Paepegem,[86] and the most recent advances in the nonlinear damage accumulation for composites are dealt with by Sarkani.[87]

The time domain approach is very general and can handle any arbitrary response history, including snap-through behavior. Despite these observations, for certain classes of loadings the frequency domain approach has its advantages. The restriction to be made while attempting to estimate the fatigue life via the frequency domain is that the response is Gaussian. Slightly non-Gaussian distributions can also be handled by performing transformations that bring the distribution to the Gaussian characteristics. This technique is the so-called Transformed Gaussian Process.[88,89] Another approach by Dirlik[90] is empirical and based on extensive computer simulations utilizing the Monte Carlo Method.

2. Finite Element Formulation

2.1 Element Displacement Functions

A typical triangular shallow shell element of an arbitrary shape is described by two radii - R_x and R_y as shown in Figure 2.1. The element used in this work is derived from MIN3 plate element.[91-92]

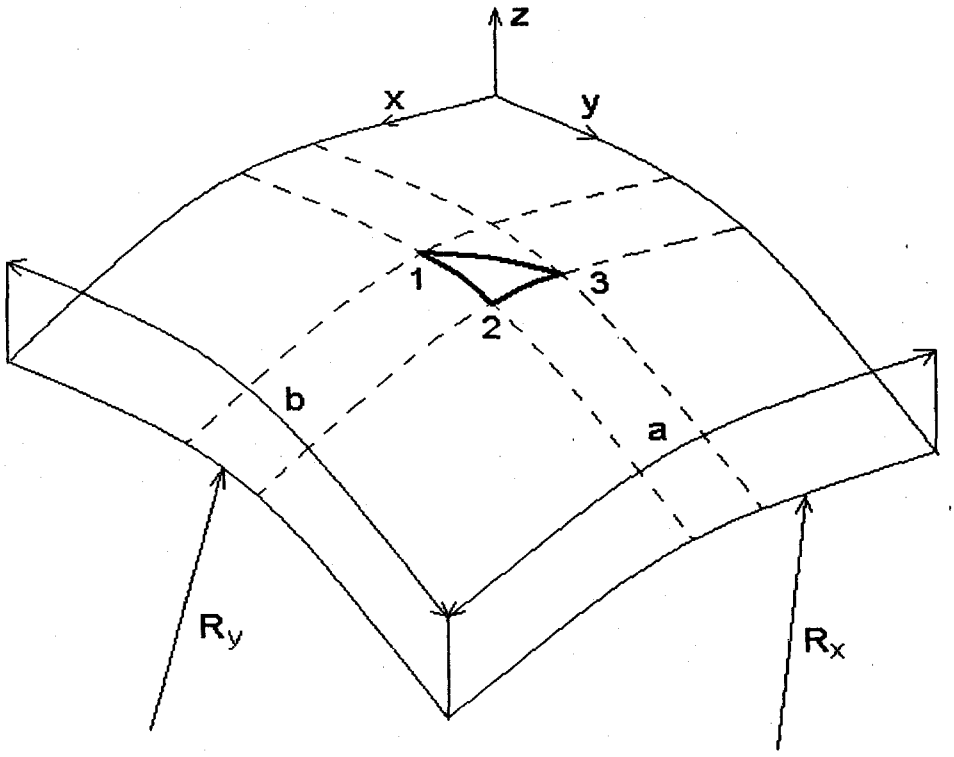

Figure 2.1 Triangular Shallow Shell Element

The displacement functions at any point (x, y, z) in the element are

$$u_x = u(x,y,t) + z\psi_y(x,y,t)$$

$$u_y = v(x,y,t) + z\psi_x(x,y,t) \qquad (2.1)$$

$$u_w = w(x,y,t)$$

where u,v,w are the displacements of the middle surface, and ψ_x and ψ_y are the rotations of the normals around the x and y axes due to bending only. The element nodal displacements are defined as

$$\{w\}^T = \{\lfloor w_t \rfloor \ \lfloor \psi \rfloor \ \lfloor w_m \rfloor\} \tag{2.2}$$

where the transverse, normal rotation and membrane (inplane) components are

$$\{w_t\}^T = \lfloor w_1 \quad w_2 \quad w_3 \rfloor \tag{2.3}$$

$$\{\psi\}^T = \lfloor \psi_{x1} \quad \psi_{x2} \quad \psi_{x3} \quad \psi_{y1} \quad \psi_{y2} \quad \psi_{y3} \rfloor \tag{2.4}$$

$$\{w_m\}^T = \lfloor u_1 \quad u_2 \quad u_3 \quad v_1 \quad v_2 \quad v_3 \rfloor \tag{2.5}$$

The interpolation functions[91-92] for the shallow shell element are

$$\begin{aligned} w(x,y,t) &= \lfloor H_w \rfloor \{w_t\} + \lfloor H_{w\psi} \rfloor \{\psi\} \\ &= \lfloor \xi_1 \quad \xi_2 \quad \xi_3 \rfloor \{w_t\} + \lfloor L_1 \quad L_2 \quad L_3 \quad M_1 \quad M_2 \quad M_3 \rfloor \{\psi\} \end{aligned} \tag{2.6}$$

$$\psi_x(x,y,t) = \lfloor H_{\psi x} \rfloor \{\psi\} = \lfloor \xi_1 \quad \xi_2 \quad \xi_3 \quad 0 \quad 0 \quad 0 \rfloor \{\psi\} \tag{2.7}$$

$$\psi_y(x,y,t) = \lfloor H_{\psi y} \rfloor \{\psi\} = \lfloor 0 \quad 0 \quad 0 \quad \xi_1 \quad \xi_2 \quad \xi_3 \rfloor \{\psi\} \tag{2.8}$$

$$u(x,y,t) = \lfloor H_u \rfloor \{w_m\} = \lfloor \xi_1 \quad \xi_2 \quad \xi_3 \quad 0 \quad 0 \quad 0 \rfloor \{w_m\} \tag{2.9}$$

$$v(x,y,t) = \lfloor H_v \rfloor \{w_m\} = \lfloor 0 \quad 0 \quad 0 \quad \xi_1 \quad \xi_2 \quad \xi_3 \rfloor \{w_m\} \tag{2.10}$$

where ξ_1, ξ_2, ξ_3 are the area coordinates and the transformation between x, y and ξ_i is given by

$$\begin{Bmatrix} 1 \\ x \\ y \end{Bmatrix} = \begin{bmatrix} 1 & 1 & 1 \\ x_1 & x_2 & x_3 \\ y_1 & y_2 & y_3 \end{bmatrix} \begin{Bmatrix} \xi_1 \\ \xi_2 \\ \xi_3 \end{Bmatrix} \tag{2.11}$$

$$\begin{Bmatrix} \xi_1 \\ \xi_2 \\ \xi_3 \end{Bmatrix} = \frac{1}{2A} \begin{bmatrix} x_2 y_3 - x_3 y_2 & y_2 - y_3 & x_3 - x_2 \\ x_3 y_1 - x_1 y_3 & y_3 - y_1 & x_1 - x_3 \\ x_1 y_2 - x_2 y_1 & y_1 - y_2 & x_2 - x_1 \end{bmatrix} \begin{Bmatrix} 1 \\ x \\ y \end{Bmatrix} \tag{2.12}$$

where

$$A=\frac{1}{2}[(x_2-x_1)(y_3-y_1)-(x_3-x_1)(y_2-y_1)] \tag{2.13}$$

and

$$\begin{aligned} L_1&=\frac{1}{8}(b_3N_4-b_2N_6), & L_2&=\frac{1}{8}(b_1N_5-b_3N_4)\\ L_3&=\frac{1}{8}(b_2N_6-b_1N_5), & M_1&=\frac{1}{8}(a_2N_6-a_3N_4)\\ M_2&=\frac{1}{8}(a_3N_4-a_1N_5), & M_3&=\frac{1}{8}(a_1N_5-a_2N_6)\\ N_4&=4\xi_1\xi_2, & N_5&=4\xi_2\xi_3, & N_6&=4\xi_3\xi_1 \end{aligned} \tag{2.14}$$

where

$$\begin{aligned} a_1&=x_{32}, & a_2&=x_{13}, & a_3&=x_{21}\\ b_1&=y_{23}, & b_2&=y_{31}, & b_3&=y_{12}\\ x_{ij}&=x_i-x_j, & y_{ij}&=y_i-y_j \end{aligned} \tag{2.15}$$

and

$$\int_A \xi_1^{\,k}\xi_2^{\,l}\xi_3^{\,m}dA=2A\frac{k!l!m!}{(2+k+l+m)!} \tag{2.16}$$

2.2 Strain - Displacement Relations

The strain consists of two components

$$\{\varepsilon\}=\begin{Bmatrix}\varepsilon_x\\ \varepsilon_y\\ \gamma_{xy}\end{Bmatrix}=\{\varepsilon^0\}+z\{\kappa\} \tag{2.17}$$

where $\{\varepsilon^0\}$ is the inplane strain vector and $\{\kappa\}$ is the curvature vector. These components can be expressed by functions of displacement as[2]

$$\{\varepsilon^0\}=\{\varepsilon_m^0\}+\{\varepsilon_b^0\}+\{\varepsilon_R^0\}=$$
$$=\begin{Bmatrix} u_{,x} \\ v_{,y} \\ u_{,y}+v_{,x} \end{Bmatrix}+\frac{1}{2}\begin{Bmatrix} w_{,x}^2 \\ w_{,y}^2 \\ 2w_{,x}w_{,y} \end{Bmatrix}+\begin{Bmatrix} w/R_x \\ w/R_y \\ 0 \end{Bmatrix} \tag{2.18}$$

$$\{\kappa\}=\begin{Bmatrix} \psi_{y,x} \\ \psi_{x,y} \\ \psi_{y,y}+\psi_{x,x} \end{Bmatrix} \tag{2.19}$$

Therefore combining Equations (2.17) to (2.19) the expression for the strain becomes

$$\{\varepsilon\}=\{\varepsilon_m^0\}+\{\varepsilon_b^0\}+\{\varepsilon_R^0\}+z\{\kappa\}=$$
$$=\begin{Bmatrix} u_{,x} \\ v_{,y} \\ u_{,y}+v_{,x} \end{Bmatrix}+\frac{1}{2}\begin{Bmatrix} w_{,x}^2 \\ w_{,y}^2 \\ 2w_{,x}w_{,y} \end{Bmatrix}+\begin{Bmatrix} w/R_x \\ w/R_y \\ 0 \end{Bmatrix}+z\begin{Bmatrix} \psi_{y,x} \\ \psi_{x,y} \\ \psi_{y,y}+\psi_{x,x} \end{Bmatrix} \tag{2.20}$$

Defining the strain interpolation matrices

$$[C_m]=\begin{bmatrix} \lfloor H_u \rfloor_{,x} \\ \lfloor H_v \rfloor_{,y} \\ \lfloor H_u \rfloor_{,y}+\lfloor H_v \rfloor_{,x} \end{bmatrix} \tag{2.21}$$

$$[\theta]=\begin{bmatrix} w_{,x} & 0 \\ 0 & w_{,y} \\ w_{,y} & w_{,x} \end{bmatrix} \tag{2.22}$$

$$\{G\}=\begin{Bmatrix} w_{,x} \\ w_{,y} \end{Bmatrix} \tag{2.23}$$

$$[C_{\psi n}]=\begin{bmatrix} \lfloor H_w \rfloor_{,x} \\ \lfloor H_w \rfloor_{,y} \end{bmatrix} \tag{2.24}$$

$$[C_{\psi\psi}]=\begin{bmatrix} \lfloor H_{w\psi} \rfloor_{,x} \\ \lfloor H_{w\psi} \rfloor_{,y} \end{bmatrix} \tag{2.25}$$

$$\{C_R\}=\begin{Bmatrix} 1/R_x \\ 1/R_y \\ 0 \end{Bmatrix} \tag{2.26}$$

$$[C_t]=\begin{bmatrix} \lfloor H_{\psi y} \rfloor_{,x} \\ \lfloor H_{\psi x} \rfloor_{,y} \\ \lfloor H_{\psi y} \rfloor_{,y} + \lfloor H_{\psi x} \rfloor_{,x} \end{bmatrix} \tag{2.27}$$

one can write

$$\{\varepsilon^0\}=[C_m]\{w_m\}+\frac{1}{2}[\theta](\{C_{\psi t}\}\{w_t\}+[C_{\psi\psi}]\{\psi\})+\{C_R\}(\lfloor H_w \rfloor\{w_t\}+\lfloor H_{w\psi} \rfloor\{\psi\}) \tag{2.28}$$

$$\{\kappa\}=[C_t]\{\psi\} \tag{2.29}$$

The shear strain-displacement relation under First Order Shear Deformation Theory (Figure 2.2) is given by

$$\{\gamma\}=\begin{Bmatrix} \gamma_{yz} \\ \gamma_{xz} \end{Bmatrix}=\begin{Bmatrix} w_{,y} \\ w_{,x} \end{Bmatrix}+\begin{Bmatrix} \psi_x \\ \psi_y \end{Bmatrix}-\begin{Bmatrix} u/R_x \\ v/R_y \end{Bmatrix} \tag{2.30}$$

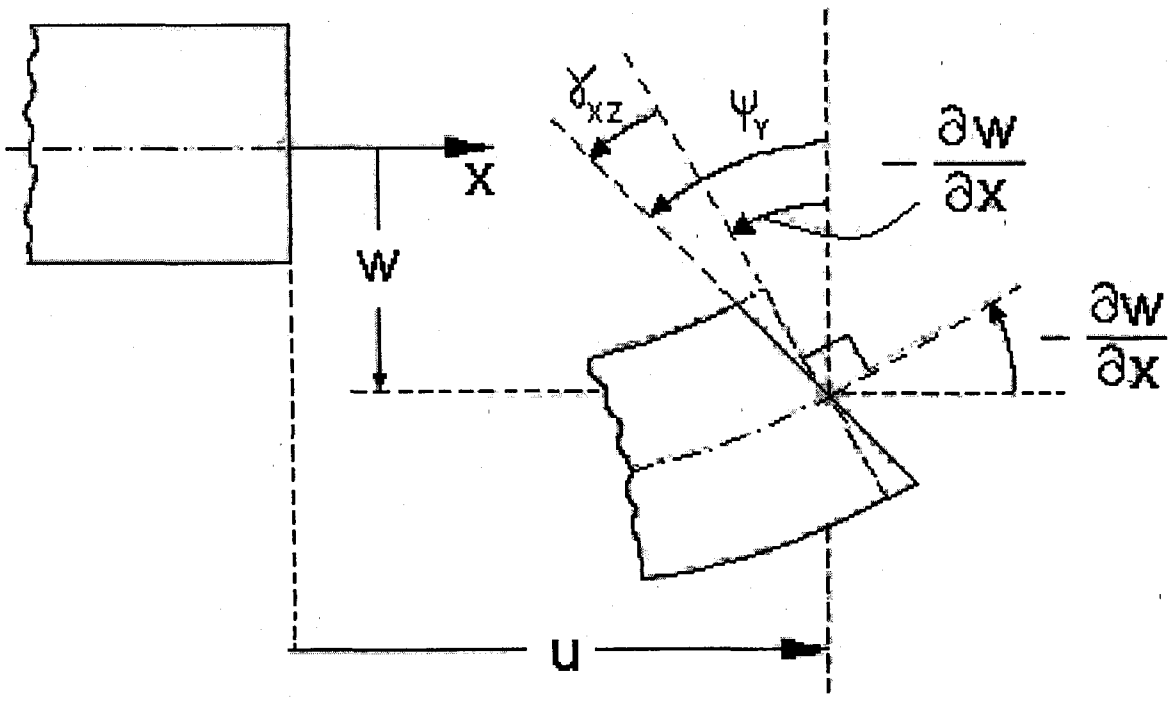

Figure 2.2 First Order Shear Deformation Theory

Defining the strain interpolation matrices

$$[C_n]=\begin{bmatrix}[H_w]_{,y}\\ [H_w]_{,x}\end{bmatrix} \tag{2.31}$$

$$[C_{n\psi}]=\begin{bmatrix}[H_{w\psi}]_{,y}+[H_{\psi x}]\\ [H_{w\psi}]_{,x}+[H_{\psi y}]\end{bmatrix} \tag{2.32}$$

$$[C_{nR}]=\begin{bmatrix}1/R_x & 0\\ 0 & 1/R_y\end{bmatrix} \tag{2.33}$$

$$[C_m]=\begin{bmatrix}[H_u]\\ [H_v]\end{bmatrix} \tag{2.34}$$

one can write

$$\{\gamma\} = [C_{\gamma t}]\{w_t\} + [C_{\gamma\psi}]\{\psi\} - [C_{\gamma R}][C_{\gamma m}]\{w_m\} \tag{2.35}$$

2.3 Constitutive Relations

For the k[th] layer of a laminate the stress-strain relations are given by

$$\{\sigma\}_k = \begin{Bmatrix}\sigma_x \\ \sigma_y \\ \tau_{xy}\end{Bmatrix}_k = \begin{bmatrix}\overline{Q}_{11} & \overline{Q}_{12} & \overline{Q}_{16} \\ \overline{Q}_{12} & \overline{Q}_{22} & \overline{Q}_{26} \\ \overline{Q}_{16} & \overline{Q}_{26} & \overline{Q}_{66}\end{bmatrix}_k \left(\begin{Bmatrix}\varepsilon_x \\ \varepsilon_y \\ \gamma_{xy}\end{Bmatrix} - \begin{Bmatrix}\alpha_x \\ \alpha_y \\ \alpha_{xy}\end{Bmatrix}_k \Delta T \right) = [\overline{Q}]_k (\{\varepsilon\} - \{\alpha\}_k \Delta T) \tag{2.36}$$

$$\{\tau\}_k = \begin{Bmatrix}\tau_{yz} \\ \tau_{xz}\end{Bmatrix}_k = \begin{bmatrix}\overline{Q}_{44} & \overline{Q}_{45} \\ \overline{Q}_{45} & \overline{Q}_{55}\end{bmatrix}_k \begin{Bmatrix}\gamma_{yz} \\ \gamma_{xz}\end{Bmatrix} = [\overline{Q}_s]_k \{\gamma\} \tag{2.37}$$

where the transformed reduced lamina stiffness matrices are

$$[\overline{Q}]_k = [T_\sigma]^{-1}[Q]_k[T_\varepsilon] \tag{2.38}$$

$$[\overline{Q}_s]_k = [T_{\sigma s}]^{-1}[Q_s]_k[T_{\varepsilon s}] \tag{2.39}$$

and the transformation matrices are given by

$$[T_\sigma] = \begin{bmatrix} c^2 & s^2 & 2cs \\ s^2 & c^2 & -2cs \\ -cs & cs & c^2 - s^2 \end{bmatrix} \tag{2.40}$$

$$[T_\varepsilon] = \begin{bmatrix} c^2 & s^2 & cs \\ s^2 & c^2 & -cs \\ -2cs & 2cs & c^2 - s^2 \end{bmatrix} \tag{2.41}$$

$$[T_{\sigma s}]=[T_{\varepsilon s}]=\begin{bmatrix} c & -s \\ s & c \end{bmatrix} \tag{2.42}$$

and

$$\{\alpha\}_k=\begin{Bmatrix}\alpha_x\\ \alpha_y\\ \alpha_{xy}\end{Bmatrix}_k=[T_\varepsilon]^T\begin{Bmatrix}\alpha_1\\ \alpha_2\\ 0\end{Bmatrix}_k \tag{2.43}$$

2.4 Resultant Laminate Forces and Moments

The resultant forces, moments and shear forces per unit length acting on a laminate are obtained by integration of the stresses in each layer through the laminate thickness

$$\{N\}=\int_{-\frac{h}{2}}^{\frac{h}{2}}\{\sigma\}_k\,dz \tag{2.44}$$

$$\{M\}=\int_{-\frac{h}{2}}^{\frac{h}{2}}\{\sigma\}_k\,z\,dz \tag{2.45}$$

$$\{R\}=\int_{-\frac{h}{2}}^{\frac{h}{2}}\{\tau\}_k\,dz \tag{2.46}$$

Introducing the extensional, coupling, bending and shear stiffness matrices, $[A],[B],[D]$ and $[A_s]$ respectively one can write

$$\begin{Bmatrix}N\\ M\end{Bmatrix}=\begin{bmatrix}[A] & [B]\\ [B] & [D]\end{bmatrix}\begin{Bmatrix}\varepsilon^0\\ \kappa\end{Bmatrix}-\begin{Bmatrix}N_{\Delta T}\\ M_{\Delta T}\end{Bmatrix} \tag{2.47}$$

$$\{R\}=[A_s]\{\gamma\} \tag{2.48}$$

where

$$[A]=\sum_{k=1}^{n}[\bar{Q}]_k(z_{k+1}-z_k) \tag{2.49}$$

$$[B]=\frac{1}{2}\sum_{k=1}^{n}[\bar{Q}]_k(z_{k+1}^2-z_k^2) \tag{2.50}$$

$$[D]=\frac{1}{3}\sum_{k=1}^{n}[\bar{Q}]_k(z_{k+1}^3-z_k^3) \tag{2.51}$$

$$[A_s]=\sum_{k=1}^{n}[\bar{Q}_s]_k(z_{k+1}-z_k) \tag{2.52}$$

and

$$\{N_{\Delta T}\}=\sum_{k=1}^{n}[\bar{Q}_k]\{\alpha\}_k\left[T_0(z_{k+1}-z_k)+\frac{1}{2}\frac{\Delta T_h}{h}(z_{z+1}^2-z_z^2)\right] \tag{2.53}$$

$$\{M_{\Delta T}\}=\sum_{k=1}^{n}[\bar{Q}_k]\{\alpha\}_k\left[\frac{1}{2}T_0(z_{z+1}^2-z_z^2)+\frac{1}{3}\frac{\Delta T_h}{h}(z_{z+1}^3-z_z^3)\right] \tag{2.54}$$

where T_o represents a uniform temperature increment, and ΔT_h the linear temperature gradient across the thickness of the panel.

2.5 Equations of Motion

Finite element equations of motion for a laminated composite shallow shell are derived utilizing the principle of virtual work.

$$\delta W=\delta W_{\text{int}}-\delta W_{ext}=0 \tag{2.55}$$

The work done by internal forces is given by

$$\delta W_{\text{int}}=\int_A\left(\{\delta\varepsilon^0\}^T\{N\}+\{\delta\kappa\}^T\{M\}+\alpha\{\delta\gamma\}^T\{R\}\right)dA \tag{2.56}$$

where α is the shear correction factor for the MIN3 element, defined as[92]

$$\alpha = \left(1 + \frac{1}{2}\frac{tr\left([k]_{\psi}^{s}\right)}{tr\left([k]_{\psi}\right)}\right)^{-1} \tag{2.57}$$

where [k] is a linear stiffness matrix, and [k^s] is the shear stiffness matrix, and they are both introduced later in this chapter.

From Eqs. (2.28), (2.29), and (2.35) one can obtain[18,36]

$$\begin{aligned}\{\delta\varepsilon^0\}^T &= \{\delta w_m\}^T [C_m]^T + \frac{1}{2}\{\delta w_t\}^T [C_{wt}]^T [\theta]^T + \frac{1}{2}\{w_t\}^T [C_{wt}]^T [\delta\theta]^T \\ &+ \frac{1}{2}\{\delta\psi\}^T [C_{\psi\psi}]^T [\theta]^T + \frac{1}{2}\{\psi\}^T [C_{\psi\psi}]^T [\delta\theta]^T \\ &+ \{\delta w_t\}^T [H_w]^T \{C_R\}^T + \{\delta\psi\}^T [H_{w\psi}]^T \{C_R\}^T \\ &= \{\delta w_m\}^T [C_m]^T + \{\delta w_t\}^T [C_{wt}]^T [\theta]^T + \{\delta\psi\}^T [C_{\psi\psi}]^T [\theta]^T \\ &+ \{\delta w_t\}^T [H_w]^T \{C_R\}^T + \{\delta\psi\}^T [H_{w\psi}]^T \{C_R\}^T\end{aligned} \tag{2.58}$$

$$\{\delta\kappa\}^T = \{\delta\psi\}^T [C_t]^T \tag{2.59}$$

$$\{\delta\gamma\}^T = \{\delta w_t\}^T [C_{\gamma t}]^T + \{\delta\psi\}^T [C_{\gamma\psi}]^T - \{\delta w_m\}^T [C_{\gamma m}]^T [C_{\gamma R}]^T \tag{2.60}$$

From Eqs.(2.47) and (2.48) one can obtain

$$\{N\} = [A]\{\varepsilon^0\} + [B]\{\kappa\} - \{N_{\Delta T}\} \tag{2.61}$$

$$\{M\} = [B]\{\varepsilon^0\} + [D]\{\kappa\} - \{M_{\Delta T}\} \tag{2.62}$$

$$\{R\} = [A_s]\{\gamma\} \tag{2.63}$$

Expanding the term of the work done by internal forces in Eq.(2.56) one obtains

$$\delta W_{\text{int}} = \int_A \Big[\{\delta w_m\}^T [C_m]^T + \{\delta w_t\}^T [C_{\psi t}]^T [\theta]^T + \{\delta\psi\}^T [C_{\psi\psi}]^T [\theta]^T$$
$$+ \{\delta w_t\}^T [H_w]^T \{C_R\}^T + \{\delta\psi\}^T [H_{w\psi}]^T \{C_R\}^T \Big([A][C_m]\{w_m\} + \frac{1}{2}[A][\theta][C_{\psi t}]\{w_t\}$$
$$+ \frac{1}{2}[A][\theta][C_{\psi\psi}]\{\psi\} + [A]\{C_R\}[H_w]\{w_t\} + [A]\{C_R\}[H_{w\psi}]\{\psi\} + [B][C_t]\{\psi\} - \{N_{\Delta T}\} \Big)$$
$$+ \{\delta\psi\}^T [C_t]^T \Big([B][C_m]\{w_m\} + \frac{1}{2}[B][\theta][C_{\psi t}]\{w_t\} + \frac{1}{2}[B][\theta][C_{\psi\psi}]\{\psi\} \qquad (2.64)$$
$$+ [B]\{C_R\}[H_w]\{w_t\} + [B]\{C_R\}[H_{w\psi}]\{\psi\} + [D][C_t]\{\psi\} - \{M_{\Delta T}\} \Big)$$
$$+ \alpha \Big(\{\delta w_t\}^T [C_{\gamma t}]^T + \{\delta\psi\}^T [C_{\gamma\psi}]^T - \{\delta w_m\}^T [C_{\gamma m}]^T [C_{\gamma R}]^T \Big)$$
$$\big([A_s][C_{\gamma t}]\{w_t\} + [A_s][C_{\gamma\psi}]\{\psi\} - [A_s][C_{\gamma R}][C_{\gamma m}]\{w_m\} \big) \Big] dA$$

Further expansion leads to

$$\delta W_{\text{int}} = \int_A \Big(\{\delta w_m\}^T [C_m]^T [A][C_m]\{w_m\} \qquad (2.65\text{-}1)$$

$$+ \frac{1}{2}\{\delta w_m\}^T [C_m]^T [A][\theta][C_{\psi t}]\{w_t\} \qquad (2.65\text{-}2)$$

$$+ \frac{1}{2}\{\delta w_m\}^T [C_m]^T [A][\theta][C_{\psi\psi}]\{\psi\} \qquad (2.65\text{-}3)$$

$$+ \{\delta w_m\}^T [C_m]^T [A]\{C_R\}[H_w]\{w_t\} \qquad (2.65\text{-}4)$$

$$+ \{\delta w_m\}^T [C_m]^T [A]\{C_R\}[H_{w\psi}]\{\psi\} \qquad (2.65\text{-}5)$$

$$+ \{\delta w_t\}^T [C_{\psi t}]^T [\theta]^T [A][C_m]\{w_m\} \qquad (2.65\text{-}6)$$

$$+ \frac{1}{2}\{\delta w_t\}^T [C_{\psi t}]^T [\theta]^T [A][\theta][C_{\psi t}]\{w_t\} \qquad (2.65\text{-}7)$$

$$+ \frac{1}{2}\{\delta w_t\}^T [C_{\psi t}]^T [\theta]^T [A][\theta][C_{\psi\psi}]\{\psi\} \qquad (2.65\text{-}8)$$

$$+ \{\delta w_t\}^T [C_{\psi t}]^T [\theta]^T [A]\{C_R\}[H_w]\{w_t\} \qquad (2.65\text{-}9)$$

$$+ \{\delta w_t\}^T [C_{\psi t}]^T [\theta]^T [A]\{C_R\}[H_{w\psi}]\{\psi\} \qquad (2.65\text{-}10)$$

$$+\{\delta\psi\}^T[C_{\psi\psi}]^T[\theta]^T[A][C_m]\{w_m\} \quad (2.65\text{-}11)$$

$$+\frac{1}{2}\{\delta\psi\}^T[C_{\psi\psi}]^T[\theta]^T[A][\theta][C_{\psi t}]\{w_t\} \quad (2.65\text{-}12)$$

$$+\frac{1}{2}\{\delta\psi\}^T[C_{\psi\psi}]^T[\theta]^T[A][\theta][C_{\psi\psi}]\{\psi\} \quad (2.65\text{-}13)$$

$$+\{\delta\psi\}^T[C_{\psi\psi}]^T[\theta]^T[A]\{C_R\}[H_w]\{w_t\} \quad (2.65\text{-}14)$$

$$+\{\delta\psi\}^T[C_{\psi\psi}]^T[\theta]^T[A]\{C_R\}[H_{w\psi}]\{\psi\} \quad (2.65\text{-}15)$$

$$+\{\delta w_t\}^T[H_w]^T\{C_R\}^T[A][C_m]\{w_m\} \quad (2.65\text{-}16)$$

$$+\frac{1}{2}\{\delta w_t\}^T[H_w]^T\{C_R\}^T[A][\theta][C_{\psi t}]\{w_t\} \quad (2.65\text{-}17)$$

$$+\frac{1}{2}\{\delta w_t\}^T[H_w]^T\{C_R\}^T[A][\theta][C_{\psi\psi}]\{\psi\} \quad (2.65\text{-}18)$$

$$+\{\delta w_t\}^T[H_w]^T\{C_R\}^T[A]\{C_R\}[H_w]\{w_t\} \quad (2.65\text{-}19)$$

$$+\{\delta w_t\}^T[H_w]^T\{C_R\}^T[A]\{C_R\}[H_{w\psi}]\{\psi\} \quad (2.65\text{-}20)$$

$$+\{\delta\psi\}^T[H_{w\psi}]^T\{C_R\}^T[A][C_m]\{w_m\} \quad (2.65\text{-}21)$$

$$+\frac{1}{2}\{\delta\psi\}^T[H_{w\psi}]^T\{C_R\}^T[A][\theta][C_{\psi t}]\{w_t\} \quad (2.65\text{-}22)$$

$$+\frac{1}{2}\{\delta\psi\}^T[H_{w\psi}]^T\{C_R\}^T[A][\theta][C_{\psi\psi}]\{\psi\} \quad (2.65\text{-}23)$$

$$+\{\delta\psi\}^T[H_{w\psi}]^T\{C_R\}^T[A]\{C_R\}[H_w]\{w_t\} \quad (2.65\text{-}24)$$

$$+\{\delta\psi\}^T[H_{w\psi}]^T\{C_R\}^T[A]\{C_R\}[H_{w\psi}]\{\psi\} \quad (2.65\text{-}25)$$

$$+\{\delta w_m\}^T[C_m]^T[B][C_t]\{\psi\} \quad (2.65\text{-}26)$$

$$+\{\delta w_t\}^T[C_{\psi t}]^T[\theta]^T[B][C_t]\{\psi\} \quad (2.65\text{-}27)$$

$$+\{\delta\psi\}^T[C_{\psi\psi}]^T[\theta]^T[B][C_t]\{\psi\} \quad (2.65\text{-}28)$$

$$+\{\delta w_t\}^T\lfloor H_w\rfloor^T\{C_R\}^T[B][C_t]\{\psi\} \quad (2.65\text{-}29)$$

$$+\{\delta\psi\}^T\lfloor H_{w\psi}\rfloor^T\{C_R\}^T[B][C_t]\{\psi\} \quad (2.65\text{-}30)$$

$$-\{\delta w_m\}^T[C_m]^T\{N_{\Delta T}\} \quad (2.65\text{-}31)$$

$$-\{\delta w_t\}^T[C_{\psi t}]^T[\theta]^T\{N_{\Delta T}\} \quad (2.65\text{-}32)$$

$$-\{\delta\psi\}^T[C_{\psi\psi}]^T[\theta]^T\{N_{\Delta T}\} \quad (2.65\text{-}33)$$

$$-\{\delta w_t\}^T\lfloor H_w\rfloor^T\{C_R\}^T\{N_{\Delta T}\} \quad (2.65\text{-}34)$$

$$-\{\delta\psi\}^T\lfloor H_{w\psi}\rfloor^T\{C_R\}^T\{N_{\Delta T}\} \quad (2.65\text{-}35)$$

$$+\{\delta\psi\}^T[C_t]^T[B][C_m]\{w_m\} \quad (2.65\text{-}36)$$

$$+\frac{1}{2}\{\delta\psi\}^T[C_t]^T[B][\theta][C_{\psi t}]\{w_t\} \quad (2.65\text{-}37)$$

$$+\frac{1}{2}\{\delta\psi\}^T[C_t]^T[B][\theta][C_{\psi\psi}]\{\psi\} \quad (2.65\text{-}38)$$

$$+\{\delta\psi\}^T[C_t]^T[B][C_R]\lfloor H_w\rfloor\{w_t\} \quad (2.65\text{-}39)$$

$$+\{\delta\psi\}^T[C_t]^T[B][C_R]\lfloor H_{w\psi}\rfloor\{\psi\} \quad (2.65\text{-}40)$$

$$+\{\delta\psi\}^T[C_t]^T[D][C_t]\{\psi\} \quad (2.65\text{-}41)$$

$$-\{\delta\psi\}^T[C_t]^T\{M_{\Delta T}\} \quad (2.65\text{-}42)$$

$$+\alpha\{\delta w_t\}^T[C_{\gamma t}]^T[A_s][C_{\gamma t}]\{w_t\} \quad (2.65\text{-}43)$$

$$+\alpha\{\delta w_t\}^T[C_{\gamma t}]^T[A_s][C_{\gamma\psi}]\{\psi\} \quad (2.65\text{-}44)$$

$$-\alpha\{\delta w_t\}^T[C_{\gamma t}]^T[A_s][C_{\gamma R}][C_{\gamma m}]\{w_m\} \quad (2.65\text{-}45)$$

$$+\alpha\{\delta\psi\}^T[C_{\gamma\psi}]^T[A_s][C_\gamma]\{w_t\} \tag{2.65-46}$$

$$+\alpha\{\delta\psi\}^T[C_{\gamma\psi}]^T[A_s][C_{\gamma\psi}]\{\psi\} \tag{2.65-47}$$

$$-\alpha\{\delta\psi\}^T[C_{\gamma\psi}]^T[A_s][C_{\gamma R}][C_{\gamma m}]\{w_m\} \tag{2.65-48}$$

$$-\alpha\{\delta w_m\}^T[C_{\gamma m}]^T[C_{\gamma R}]^T[A_s][C_\gamma]\{w_t\} \tag{2.65-49}$$

$$-\alpha\{\delta w_m\}^T[C_{\gamma m}]^T[C_{\gamma R}]^T[A_s][C_{\gamma\psi}]\{\psi\} \tag{2.65-50}$$

$$+\alpha\{\delta w_m\}^T[C_{\gamma m}]^T[C_{\gamma R}]^T[A_s][C_{\gamma R}][C_{\gamma m}]\{w_m\}\big)\,dA \tag{2.65-51}$$

Therefore, the membrane-normal linear stiffness matrices are

$$[k_m]=\int_A[C_m]^T[A][C_m]dA \tag{2.66}$$

$$[k_{m\psi}]=\int_A[C_m]^T[B][C_t]dA \tag{2.67}$$

$$[k_{\psi m}]=\int_A[C_t]^T[B][C_m]dA \tag{2.68}$$

$$[k_\psi]=\int_A[C_t]^T[D][C_t]dA \tag{2.69}$$

and shear linear stiffness matrices are

$$[k_t^s]=\alpha\int_A[C_\gamma]^T[A_s][C_\gamma]dA \tag{2.70}$$

$$[k_{t\psi}^s]=\alpha\int_A[C_\gamma]^T[A_s][C_{\gamma\psi}]dA \tag{2.71}$$

$$[k_{\psi t}^s]=\alpha\int_A[C_{\gamma\psi}]^T[A_s][C_\gamma]dA \tag{2.72}$$

$$[k_\psi^s]=\alpha\int_A[C_{\gamma\psi}]^T[A_s][C_{\gamma\psi}]dA \tag{2.73}$$

and shear linear stiffness matrices due to the shell geometry are

$$[k_{tm}^{sR}] = \alpha \int_A [C_{\gamma t}]^T [A_s][C_{\gamma R}][C_{\gamma m}]\,dA \tag{2.74}$$

$$[k_{mt}^{sR}] = \alpha \int_A [C_{\gamma m}]^T [C_{\gamma R}]^T [A_s][C_{\gamma t}]\,dA \tag{2.75}$$

$$[k_{\psi m}^{sR}] = \alpha \int_A [C_{\gamma \psi}]^T [A_s][C_{\gamma R}][C_{\gamma m}]\,dA \tag{2.76}$$

$$[k_{m\psi}^{sR}] = \alpha \int_A [C_{\gamma m}]^T [C_{\gamma R}]^T [A_s][C_{\gamma \psi}]\,dA \tag{2.77}$$

$$[k_{m}^{sR}] = \alpha \int_A [C_{\gamma m}]^T [C_{\gamma R}]^T [A_s][C_{\gamma R}][C_{\gamma m}]\,dA \tag{2.78}$$

The linear stiffness matrices due to the shell geometry are

$$[k_{t}^{R}] = \int_A [H_w]^T \{C_R\}^T [A]\{C_R\}[H_w]\,dA \tag{2.79}$$

$$[k_{t\psi}^{RB}] = \int_A [H_w]^T \{C_R\}^T [B][C_t]\,dA \tag{2.80}$$

$$[k_{t\psi}^{RA}] = \int_A [H_w]^T \{C_R\}^T [A]\{C_R\}[H_{w\psi}]\,dA \tag{2.81}$$

$$[k_{tm}^{R}] = \int_A [H_w]^T \{C_R\}^T [A][C_m]\,dA \tag{2.82}$$

$$[k_{\psi t}^{RB}] = \int_A [C_t]^T [B]\{C_R\}[H_w]\,dA \tag{2.83}$$

$$[k_{\psi t}^{RA}] = \int_A [H_{w\psi}]^T \{C_R\}^T [A]\{C_R\}[H_w]\,dA \tag{2.84}$$

$$[k_{\psi}^{RA}] = \int_A [H_{w\psi}]^T \{C_R\}^T [A]\{C_R\}[H_{w\psi}]\,dA \tag{2.85}$$

$$[k_{\psi}^{RB}]^T = \int_A [H_{w\psi}]^T \{C_R\}^T [B][C_t]\,dA \tag{2.86}$$

$$[k_{\psi}^{RB}] = \int_A [C_t]^T [B]\{C_R\}[H_{w\psi}]\,dA \tag{2.87}$$

$$[k^R_{\psi m}] = \int_A [H_{w\psi}]^T \{C_R\}^T [A][C_m]dA \tag{2.88}$$

$$[k^R_{mt}] = \int_A [C_m]^T [A]\{C_R\}[H_w]dA \tag{2.89}$$

$$[k^R_{m\psi}] = \int_A [C_m]^T [A]\{C_R\}[H_{w\psi}]dA \tag{2.90}$$

Expanding parts of the integrals of Eqs. (2.65-32) and (2.65-33), one can show that

$$[\theta]^T \{N_{\Delta T}\} = [N_{\Delta T}]\{G\} = [N_{\Delta T}][C_{\psi t}]\{w_t\} + [N_{\Delta T}][C_{\psi\psi}]\{\psi\} \tag{2.91}$$

where

$$\{N_{\Delta T}\} = \begin{Bmatrix} N_{\Delta Tx} \\ N_{\Delta Ty} \\ N_{\Delta Txy} \end{Bmatrix} \tag{2.92}$$

and

$$[N_{\Delta T}] = \begin{bmatrix} N_{\Delta Tx} & N_{\Delta Txy} \\ N_{\Delta Txy} & N_{\Delta Ty} \end{bmatrix} \tag{2.93}$$

Using Eq.(2.91), and Eqs. (2.65-32 and -33) can be written as

$$\begin{aligned} &\{\delta w_t\}^T \int_A [C_{\psi t}]^T [\theta]^T \{N_{\Delta T}\}dA \\ &= \{\delta w_t\}^T \int_A [C_{\psi t}]^T [N_{\Delta T}][C_{\psi t}]dA\{w_t\} \\ &+ \{\delta w_t\}^T \int_A [C_{\psi t}]^T [N_{\Delta T}][C_{\psi\psi}]dA\{\psi\} \end{aligned} \tag{2.94}$$

and

$$\begin{aligned} &\{\delta\psi\}^T \int_A [C_{\psi\psi}]^T [\theta]^T \{N_{\Delta T}\}dA \\ &= \{\delta\psi\}^T \int_A [C_{\psi\psi}]^T [N_{\Delta T}][C_{\psi t}]dA\{w_t\} \\ &+ \{\delta\psi\}^T \int_A [C_{\psi\psi}]^T [N_{\Delta T}][C_{\psi\psi}]dA\{\psi\} \end{aligned} \tag{2.95}$$

The linear thermal stiffness matrices become

$$[k_t^{N_{\Delta T}}] = \int_A [C_{\psi t}]^T [N_{\Delta T}][C_{\psi t}]dA \tag{2.96}$$

$$[k_{t\psi}^{N_{\Delta T}}] = \int_A [C_{\psi t}]^T [N_{\Delta T}][C_{\psi\psi}]dA \tag{2.97}$$

$$[k_{\psi t}^{N_{\Delta T}}] = \int_A [C_{\psi\psi}]^T [N_{\Delta T}][C_{\psi t}]dA \tag{2.98}$$

$$[k_{\psi}^{N_{\Delta T}}] = \int_A [C_{\psi\psi}]^T [N_{\Delta T}][C_{\psi\psi}]dA \tag{2.99}$$

Expanding the first-order non-linear stiffness matrices one can notice that

$$[\theta]^T [A][C_m]\{w_m\} = [\theta]^T \{N_m\} = [N_m]\{G\} = [N_m][C_{\psi t}]\{w_t\} + [N_m][C_{\psi\psi}]\{\psi\} \tag{2.100}$$

$$[\theta]^T [B][C_t]\{\psi\} = [\theta]^T \{N_t\} = [N_t]\{G\} = [N_t][C_{\psi t}]\{w_t\} + [N_t][C_{\psi\psi}]\{\psi\} \tag{2.101}$$

$$[\theta]^T [A]\{C_R\}[H_w]\{w_t\} = [\theta]^T \{N_{C_R}^t\} = [N_{C_R}^t]\{G\} = [N_{C_R}^t][C_{\psi t}]\{w_t\} + [N_{C_R}^t][C_{\psi\psi}]\{\psi\} \tag{2.102}$$

$$[\theta]^T [A]\{C_R\}[H_{w\psi}]\{\psi\} = [\theta]^T \{N_{C_R}^{\psi}\} = [N_{C_R}^{\psi}]\{G\} = [N_{C_R}^{\psi}][C_{\psi t}]\{w_t\} + [N_{C_R}^{\psi}][C_{\psi\psi}]\{\psi\} \tag{2.103}$$

where

$$\{N_m\} = \begin{Bmatrix} N_{mx} \\ N_{my} \\ N_{mxy} \end{Bmatrix}, \quad \{N_t\} = \begin{Bmatrix} N_{tx} \\ N_{ty} \\ N_{txy} \end{Bmatrix}, \quad \{N_{C_R}^t\} = \begin{Bmatrix} N_{C_Rx}^t \\ N_{C_Ry}^t \\ N_{C_Rxy}^t \end{Bmatrix}, \quad \{N_{C_R}^{\psi}\} = \begin{Bmatrix} N_{C_Rx}^{\psi} \\ N_{C_Ry}^{\psi} \\ N_{C_Rxy}^{\psi} \end{Bmatrix} \tag{2.104}$$

and

$$[N_m] = \begin{bmatrix} N_{mx} & N_{mxy} \\ N_{mxy} & N_{my} \end{bmatrix}, \qquad [N_t] = \begin{bmatrix} N_{tx} & N_{txy} \\ N_{txy} & N_{ty} \end{bmatrix},$$

$$[N_{C_R}^t] = \begin{bmatrix} N_{C_Rx}^t & N_{C_Rxy}^t \\ N_{C_Rxy}^t & N_{C_Ry}^t \end{bmatrix}, \qquad [N_{C_R}^{\psi}] = \begin{bmatrix} N_{C_Rx}^{\psi} & N_{C_Rxy}^{\psi} \\ N_{C_Rxy}^{\psi} & N_{C_Ry}^{\psi} \end{bmatrix} \tag{2.105}$$

Wood and Schoefler[93] developed an elegant manner to cast the quadratic terms in such a way, that the quadratic stiffness matrices remain symmetrical. This concept applied to the present formulation is presented as follows.

Using Eq.(2.100) to expand Eq.(2.65-6 and -11) one obtains

$$\begin{aligned}
&\{\delta w_t\}^T \int_A [C_{\psi t}]^T [\theta]^T [A][C_m] dA \{w_m\} \\
&\quad = \frac{1}{2}\{\delta w_t\}^T \int_A [C_{\psi t}]^T [\theta]^T [A][C_m] dA \{w_m\} \\
&\quad + \frac{1}{2}\{\delta w_t\}^T \int_A [C_{\psi t}]^T [N_m][C_{\psi t}] dA \{w_t\} \\
&\quad + \frac{1}{2}\{\delta w_t\}^T \int_A [C_{\psi t}]^T [N_m][C_{\psi\psi}] dA \{\psi\}
\end{aligned} \tag{2.106}$$

and

$$\begin{aligned}
&\{\delta\psi\}^T \int_A [C_{\psi\psi}]^T [\theta]^T [A][C_m] dA \{w_m\} \\
&\quad = \frac{1}{2}\{\delta\psi\}^T \int_A [C_{\psi\psi}]^T [\theta]^T [A][C_m] dA \{w_m\} \\
&\quad + \frac{1}{2}\{\delta\psi\}^T \int_A [C_{\psi\psi}]^T [N_m][C_{\psi t}] dA \{w_t\} \\
&\quad + \frac{1}{2}\{\delta\psi\}^T \int_A [C_{\psi\psi}]^T [N_m][C_{\psi\psi}] dA \{\psi\}
\end{aligned} \tag{2.107}$$

Using Eq.(2.101) to expand Eq.(2.65-27 and -28) one obtains

$$\begin{aligned}
&\{\delta w_t\}^T \int_A [C_{\psi t}]^T [\theta]^T [B][C_t] dA \{\psi\} \\
&\quad = \frac{1}{2}\{\delta w_t\}^T \int_A [C_{\psi t}]^T [\theta]^T [B][C_t] dA \{\psi\} \\
&\quad + \frac{1}{2}\{\delta w_t\}^T \int_A [C_{\psi t}]^T [N_t][C_{\psi t}] dA \{w_t\} \\
&\quad + \frac{1}{2}\{\delta w_t\}^T \int_A [C_{\psi t}]^T [N_t][C_{\psi\psi}] dA \{\psi\}
\end{aligned} \tag{2.108}$$

and

$$\begin{aligned}
&\{\delta\psi\}^T \int_A [C_{\psi\psi}]^T [\theta]^T [B][C_t] dA \{\psi\} \\
&\quad = \frac{1}{2}\{\delta\psi\}^T \int_A [C_{\psi\psi}]^T [\theta]^T [B][C_t] dA \{\psi\} \\
&\quad + \frac{1}{2}\{\delta\psi\}^T \int_A [C_{\psi\psi}]^T [N_t][C_{\psi t}] dA \{w_t\} \\
&\quad + \frac{1}{2}\{\delta\psi\}^T \int_A [C_{\psi\psi}]^T [N_t][C_{\psi\psi}] dA \{\psi\}
\end{aligned} \tag{2.109}$$

Using Eq.(2.102) to expand Eq.(2.65-9 and -14) one obtains

$$\begin{aligned}
&\{\delta w_t\}^T \int_A [C_{\psi t}]^T [\theta]^T [A][C_R][H_w] dA \{w_t\} \\
&\quad = \frac{1}{2}\{\delta w_t\}^T \int_A [C_{\psi t}]^T [\theta]^T [A][C_R][H_w] dA \{w_t\} \\
&\quad + \frac{1}{2}\{\delta w_t\}^T \int_A [C_{\psi t}]^T [N'_{C_R}][C_{\psi t}] dA \{w_t\} \\
&\quad + \frac{1}{2}\{\delta w_t\}^T \int_A [C_{\psi t}]^T [N'_{C_R}][C_{\psi\psi}] dA \{\psi\}
\end{aligned} \tag{2.110}$$

and

$$\begin{aligned}
&\{\delta\psi\}^T \int_A [C_{\psi\psi}]^T [\theta]^T [A][C_R][H_w] dA \{w_t\} \\
&\quad = \frac{1}{2}\{\delta\psi\}^T \int_A [C_{\psi\psi}]^T [\theta]^T [A][C_R][H_w] dA \{w_t\} \\
&\quad + \frac{1}{2}\{\delta\psi\}^T \int_A [C_{\psi\psi}]^T [N'_{C_R}][C_{\psi t}] dA \{w_t\} \\
&\quad + \frac{1}{2}\{\delta\psi\}^T \int_A [C_{\psi\psi}]^T [N'_{C_R}][C_{\psi\psi}] dA \{\psi\}
\end{aligned} \tag{2.111}$$

Using Eq.(2.103) to expand Eq.(2.65-10 and -15) one obtains

$$\begin{aligned}
&\{\delta w_t\}^T \int_A [C_{\psi t}]^T [\theta]^T [A][C_R][H_{w\psi}]dA\{\psi\} \\
&\quad = \frac{1}{2}\{\delta w_t\}^T \int_A [C_{\psi t}]^T [\theta]^T [A][C_R][H_{w\psi}]dA\{\psi\} \\
&\quad + \frac{1}{2}\{\delta w_t\}^T \int_A [C_{\psi t}]^T [N^{\psi}_{C_R}][C_{\psi t}]dA\{w_t\} \\
&\quad + \frac{1}{2}\{\delta w_t\}^T \int_A [C_{\psi t}]^T [N^{\psi}_{C_R}][C_{\psi\psi}]dA\{\psi\}
\end{aligned} \tag{2.112}$$

and

$$\begin{aligned}
&\{\delta\psi\}^T \int_A [C_{\psi\psi}]^T [\theta]^T [A][C_R][H_{w\psi}]dA\{\psi\} \\
&\quad = \frac{1}{2}\{\delta\psi\}^T \int_A [C_{\psi\psi}]^T [\theta]^T [A][C_R][H_{w\psi}]dA\{\psi\} \\
&\quad + \frac{1}{2}\{\delta\psi\}^T \int_A [C_{\psi\psi}]^T [N^{\psi}_{C_R}][C_{\psi t}]dA\{w_t\} \\
&\quad + \frac{1}{2}\{\delta\psi\}^T \int_A [C_{\psi\psi}]^T [N^{\psi}_{C_R}][C_{\psi\psi}]dA\{\psi\}
\end{aligned} \tag{2.113}$$

Now, the first-order non-linear stiffness matrices corresponding to $[\theta]$ can be written as

$$[n1_{t\psi}] = \int_A [C_{\psi t}]^T [\theta]^T [B][C_t]dA \tag{2.114}$$

$$[n1_{\psi t}] = \int_A [C_t]^T [B][\theta][C_{\psi t}]dA \tag{2.115}$$

$$[n1_{tm}] = \int_A [C_{\psi t}]^T [\theta]^T [A][C_m]dA \tag{2.116}$$

$$[n1_{mt}] = \int_A [C_m]^T [A][\theta][C_{\psi t}]dA \tag{2.117}$$

$$[n1_{\psi}] = \int_A [C_t]^T [B][\theta][C_{\psi\psi}]dA \tag{2.118}$$

$$[n1_{\psi}]^T = \int_A [C_{\psi w}]^T [\theta]^T [B][C_t]\,dA \tag{2.119}$$

$$[n1_{\psi m}] = \int_A [C_{\psi w}]^T [\theta]^T [A][C_m]\,dA \tag{2.120}$$

$$[n1_{m\psi}] = \int_A [C_m]^T [A][\theta][C_{\psi w}]\,dA \tag{2.121}$$

The first-order non-linear stiffness matrices corresponding to $[N_t]$ are

$$[n1_t^{N_t}] = \int_A [C_{\psi t}]^T [N_t][C_{\psi t}]\,dA \tag{2.122}$$

$$[n1_{t\psi}^{N_t}] = \int_A [C_{\psi t}]^T [N_t][C_{\psi w}]\,dA \tag{2.123}$$

$$[n1_{\psi t}^{N_t}] = \int_A [C_{\psi w}]^T [N_t][C_{\psi t}]\,dA \tag{2.124}$$

$$[n1_{\psi}^{N_t}] = \int_A [C_{\psi w}]^T [N_t][C_{\psi w}]\,dA \tag{2.125}$$

The first-order non-linear stiffness matrices corresponding to $[N_m]$ are

$$[n1_t^{N_m}] = \int_A [C_{\psi t}]^T [N_m][C_{\psi t}]\,dA \tag{2.126}$$

$$[n1_{t\psi}^{N_m}] = \int_A [C_{\psi t}]^T [N_m][C_{\psi w}]\,dA \tag{2.127}$$

$$[n1_{\psi t}^{N_m}] = \int_A [C_{\psi w}]^T [N_m][C_{\psi t}]\,dA \tag{2.128}$$

$$[n1_{\psi}^{N_m}] = \int_A [C_{\psi w}]^T [N_m][C_{\psi w}]\,dA \tag{2.129}$$

The first-order non-linear stiffness matrices due to shallow shell geometry and corresponding to $[\theta]$ are

$$[n1_t^R]^T = \int_A [C_{\psi t}]^T [\theta]^T [A][C_R][H_w]\,dA \tag{2.130}$$

$$[n1_t^R] = \int_A [H_w]^T \{C_R\}^T [A][\theta][C_{\psi t}]dA \tag{2.131}$$

$$[n1_{t\psi}^R] = \int_A [C_{\psi t}]^T [\theta]^T [A]\{C_R\}[H_{w\psi}]dA \tag{2.132}$$

$$[n1_{t\psi}^{RT}] = \int_A [H_w]^T \{C_R\}^T [A][\theta][C_{\psi\psi}]dA \tag{2.133}$$

$$[n1_{\psi t}^R] = \int_A [C_{\psi\psi}]^T [\theta]^T [A]\{C_R\}[H_w]dA \tag{2.134}$$

$$[n1_{\psi t}^{RT}] = \int_A [H_{w\psi}]^T \{C_R\}^T [A][\theta][C_{\psi t}]dA \tag{2.135}$$

$$[n1_{\psi}^R]^T = \int_A [C_{\psi\psi}]^T [\theta]^T [A]\{C_R\}[H_{w\psi}]dA \tag{2.136}$$

$$[n1_{\psi}^R] = \int_A [H_{w\psi}]^T \{C_R\}^T [A][\theta][C_{\psi\psi}]dA \tag{2.137}$$

The first-order non-linear stiffness matrices due to the shallow shell geometry and expressed in terms of $[N_{C_R}]$ are

$$[n1_t^{N'_{C_R}}] = \int_A [C_{\psi t}]^T [N'_{C_R}][C_{\psi t}]dA \tag{2.138}$$

$$[n1_{t\psi}^{N'_{C_R}}] = \int_A [C_{\psi t}]^T [N'_{C_R}][C_{\psi\psi}]dA \tag{2.139}$$

$$[n1_{\psi t}^{N'_{C_R}}] = \int_A [C_{\psi\psi}]^T [N'_{C_R}][C_{\psi t}]dA \tag{2.140}$$

$$[n1_{\psi}^{N'_{C_R}}] = \int_A [C_{\psi\psi}]^T [N'_{C_R}][C_{\psi\psi}]dA \tag{2.141}$$

$$\left[n1_t^{N^{\psi}_{C_R}}\right] = \int_A [C_{\psi t}]^T [N^{\psi}_{C_R}][C_{\psi t}]dA \tag{2.142}$$

$$\left[n1_{t\psi}^{N^{\psi}_{C_R}}\right] = \int_A [C_{\psi t}]^T [N^{\psi}_{C_R}][C_{\psi\psi}]dA \tag{2.143}$$

$$\left[n1_{\psi t}^{N_{C_R}^{\psi}}\right] = \int_A [C_{\psi\psi}]^T [N_{C_R}^{\psi}][C_{\psi t}]dA \tag{2.144}$$

$$\left[n1_{\psi}^{N_{C_R}^{\psi}}\right] = \int_A [C_{\psi\psi}]^T [N_{C_R}^{\psi}][C_{\psi\psi}]dA \tag{2.145}$$

The second-order non-linear stiffness matrices are

$$[n2_t] = \frac{3}{2}\int_A [C_{\psi t}]^T [\theta]^T [A][\theta][C_{\psi t}]dA \tag{2.146}$$

$$[n2_{\psi t}] = \frac{3}{2}\int_A [C_{\psi\psi}]^T [\theta]^T [A][\theta][C_{\psi t}]dA \tag{2.147}$$

$$[n2_{t\psi}] = \frac{3}{2}\int_A [C_{\psi t}]^T [\theta]^T [A][\theta][C_{\psi\psi}]dA \tag{2.148}$$

$$[n2_{\psi}] = \frac{3}{2}\int_A [C_{\psi\psi}]^T [\theta]^T [A][\theta][C_{\psi\psi}]dA \tag{2.149}$$

The load vectors are

$$\{p_m^{N_{\Delta T}}\} = \int_A [C_m]^T \{N_{\Delta T}\}dA \tag{2.150}$$

$$\{p_t^{RN_{\Delta T}}\} = \int_A [H_w]^T \{C_R\}^T \{N_{\Delta T}\}dA \tag{2.151}$$

$$\{p_{\psi}^{RN_{\Delta T}}\} = \int_A [H_{w\psi}]^T \{C_R\}^T \{N_{\Delta T}\}dA \tag{2.152}$$

$$\{p_{\psi}^{M_{\Delta T}}\} = \int_A [C_t]^T \{M_{\Delta T}\}dA \tag{2.153}$$

Expanding the work done by external forces in Eq. (2.55) one obtains

$$\delta W_{ext} = \int_A [-\rho h\{\delta w\}^T \{\ddot{w}\} \tag{2.154-1}$$

$$-\rho h\{\delta u\}^T \{\ddot{u}\} \tag{2.154-2}$$

$$-\rho h\{\delta v\}^T \{\ddot{v}\} \tag{2.154-3}$$

$$+\{\delta w\}^T\{F_d\}\Big]dA \tag{2.154-4}$$

where $\{F_d\}$ is a surface traction due to random pressure fluctuation.

Further expansion of Eq. (2.154-1 to -3) leads to

$$\begin{aligned}
&\int_A\Big[-\rho h\{\delta w\}^T\{\ddot{w}\}-\rho h\{\delta u\}^T\{\ddot{u}\}-\rho h\{\delta v\}^T\{\ddot{v}\}\Big]dA=\\
&=-\int_A\rho h\Big[\big(\{\delta w_t\}^T\lfloor H_w\rfloor^T+\{\delta\psi\}^T\lfloor H_{w\psi}\rfloor^T\big)\big(\lfloor H_w\rfloor\{\ddot{w}_t\}+\lfloor H_{w\psi}\rfloor\{\ddot{\psi}\}\big)\\
&\quad+\{\delta w_m\}^T\lfloor H_u\rfloor^T\lfloor H_u\rfloor\{\ddot{w}_m\}+\{\delta w_m\}^T\lfloor H_v\rfloor^T\lfloor H_v\rfloor\{\ddot{w}_m\}\Big]dA\\
&=-\{\delta w_t\}^T\int_A\rho h\lfloor H_w\rfloor^T\lfloor H_w\rfloor\{\ddot{w}_t\}dA-\{\delta w_t\}^T\int_A\rho h\lfloor H_w\rfloor^T\lfloor H_{w\psi}\rfloor\{\ddot{\psi}\}dA\\
&\quad-\{\delta\psi\}^T\int_A\rho h\lfloor H_{w\psi}\rfloor^T\lfloor H_w\rfloor\{\ddot{w}_t\}dA-\{\delta\psi\}^T\int_A\rho h\lfloor H_{w\psi}\rfloor^T\lfloor H_{w\psi}\rfloor\{\ddot{\psi}\}dA\\
&\quad-\{\delta w_m\}^T\int_A\rho h\lfloor H_u\rfloor^T\lfloor H_u\rfloor\{\ddot{w}_m\}dA-\{\delta w_m\}^T\int_A\rho h\lfloor H_v\rfloor^T\lfloor H_v\rfloor\{\ddot{w}_m\}dA
\end{aligned} \tag{2.155}$$

Further expansion of Eq. (2.154-4) leads to

$$\begin{aligned}
\int_A\{\delta w\}^T\{F_d\}dA&=\int_A\big(\{\delta w_t\}^T\lfloor H_w\rfloor^T+\{\delta\psi\}^T\lfloor H_{w\psi}\rfloor^T\big)\{F_d\}dA\\
&=\{\delta w_t\}^T\int_A\lfloor H_w\rfloor^T\{F_d\}dA\\
&\quad+\{\delta\psi\}^T\int_A\lfloor H_{w\psi}\rfloor^T\{F_d\}dA
\end{aligned} \tag{2.156}$$

From Eq. (2.155) mass matrices can be written as

$$[m_t]=\int_A\rho h\lfloor H_w\rfloor^T\lfloor H_w\rfloor dA \tag{2.157}$$

$$[m_{t\psi}]=\int_A\rho h\lfloor H_w\rfloor^T\lfloor H_{w\psi}\rfloor dA \tag{2.158}$$

$$[m_{\psi t}]=\int_A\rho h\lfloor H_{w\psi}\rfloor^T\lfloor H_w\rfloor dA \tag{2.159}$$

$$[m_\psi]=\int_A\rho h\lfloor H_{w\psi}\rfloor^T\lfloor H_{w\psi}\rfloor dA \tag{2.160}$$

$$[m_m^u]=\int_V\rho h\lfloor H_u\rfloor^T\lfloor H_u\rfloor dA \tag{2.161}$$

$$\left[m_m^v\right] = \int_A \rho h \left[H_v\right]^T \left[H_v\right] dA \tag{2.162}$$

and the external loading vectors from Eq. (2.156) are

$$\{p_t\} = \int_A \left[H_w\right]^T \{F_d\} dA \tag{2.163}$$

$$\{p_\psi\} = \int_A \left[H_{w\psi}\right]^T \{F_d\} dA \tag{2.164}$$

The equation of motion for the shallow shell element with von Karman large deflection, shear deformation theory, and a thermal loads is

$$\begin{bmatrix} [m_t] & [m_{t\psi}] & 0 \\ [m_{\psi t}] & [m_\psi] & 0 \\ 0 & 0 & \left([m_m^u]+[m_m^v]\right) \end{bmatrix} \begin{Bmatrix} \ddot{w}_t \\ \ddot{\psi} \\ \ddot{w}_m \end{Bmatrix} \tag{2.165-1}$$

$$+ \left(\begin{bmatrix} 0 & 0 & 0 \\ 0 & [k_\psi] & [k_{\psi m}] \\ 0 & [k_{m\psi}] & [k_m] \end{bmatrix} \right. \tag{2.165-2}$$

$$+ \begin{bmatrix} [k_t^s] & [k_{t\psi}^s] & 0 \\ [k_{\psi t}^s] & [k_\psi^s] & 0 \\ 0 & 0 & 0 \end{bmatrix} \tag{2.165-3}$$

$$- \begin{bmatrix} 0 & 0 & [k_{tm}^{sR}] \\ 0 & 0 & [k_{\psi m}^{sR}] \\ [k_{mt}^{sR}] & [k_{m\psi}^{sR}] & -[k_m^{sR}] \end{bmatrix} \tag{2.165-4}$$

$$+ \begin{bmatrix} [k_t^R] & \left([k_{t\psi}^{RA}]+[k_{t\psi}^{RB}]\right) & [k_{tm}^R] \\ \left([k_{\psi t}^{RA}]+[k_{\psi t}^{RB}]\right) & \left([k_\psi^{RA}]+[k_\psi^{RB}]+[k_\psi^{RB}]^T\right) & [k_{\psi m}^R] \\ [k_{mt}^R] & [k_{m\psi}^R] & 0 \end{bmatrix} \tag{2.165-5}$$

$$- \begin{bmatrix} [k_t^{N_{\Delta T}}] & [k_{t\psi}^{N_{\Delta T}}] & 0 \\ [k_{\psi t}^{N_{\Delta T}}] & [k_\psi^{N_{\Delta T}}] & 0 \\ 0 & 0 & 0 \end{bmatrix} \tag{2.165-6}$$

$$+\frac{1}{2}\begin{bmatrix} 0 & [n1_{t\psi}] & [n1_{tm}] \\ [n1_{\psi t}] & ([n1_{\psi}]+[n1_{\psi}]^T) & [n1_{\psi m}] \\ [n1_{mt}] & [n1_{m\psi}] & 0 \end{bmatrix} \tag{2.165-7}$$

$$+\frac{1}{2}\begin{bmatrix} [n1_t^{N_t}] & [n1_{t\psi}^{N_t}] & 0 \\ [n1_{\psi t}^{N_t}] & [n1_{\psi}^{N_t}] & 0 \\ 0 & 0 & 0 \end{bmatrix} \tag{2.165-8}$$

$$+\frac{1}{2}\begin{bmatrix} [n1_t^{N_m}] & [n1_{t\psi}^{N_m}] & 0 \\ [n1_{\psi t}^{N_m}] & [n1_{\psi}^{N_m}] & 0 \\ 0 & 0 & 0 \end{bmatrix} \tag{2.165-9}$$

$$+\frac{1}{2}\begin{bmatrix} ([n1_t^R]+[n1_t^{RT}]) & ([n1_{t\psi}^R]+[n1_{t\psi}^{RT}]) & 0 \\ ([n1_{\psi t}^R]+[n1_{\psi t}^{RT}]) & ([n1_{\psi}^R]+[n1_{\psi}^{RT}]) & 0 \\ 0 & 0 & 0 \end{bmatrix} \tag{2.165-10}$$

$$+\frac{1}{2}\begin{bmatrix} \left([n1_t^{N'_{CR}}]+[n1_t^{N''_{CR}}]\right) & \left([n1_{t\psi}^{N'_{CR}}]+[n1_{t\psi}^{N''_{CR}}]\right) & 0 \\ \left([n1_{\psi t}^{N'_{CR}}]+[n1_{\psi t}^{N''_{CR}}]\right) & \left([n1_{\psi}^{N'_{CR}}]+[n1_{\psi}^{N''_{CR}}]\right) & 0 \\ 0 & 0 & 0 \end{bmatrix} \tag{2.165-11}$$

$$+\frac{1}{3}\left(\begin{bmatrix} [n2_t] & [n2_{t\psi}] & 0 \\ [n2_{\psi t}] & [n2_{\psi}] & 0 \\ 0 & 0 & 0 \end{bmatrix}\begin{Bmatrix} w_t \\ \psi \\ w_m \end{Bmatrix}\right) \tag{2.165-12}$$

$$=\begin{Bmatrix} \{p_t\} \\ \{p_{\psi}\} \\ 0 \end{Bmatrix}+\begin{Bmatrix} 0 \\ 0 \\ \{p_m^{N_{\Delta T}}\} \end{Bmatrix}+\begin{Bmatrix} 0 \\ \{p_{\psi}^{M_{\Delta T}}\} \\ 0 \end{Bmatrix}+\begin{Bmatrix} \{p_t^{RN_{\Delta T}}\} \\ \{p_{\psi}^{RN_{\Delta T}}\} \\ 0 \end{Bmatrix} \tag{2.165-13}$$

Denote for notation compactness $\{W_b\}=\begin{Bmatrix} W_t \\ \Psi_x \\ \Psi_y \end{Bmatrix}$. Now, assembling all the elements, and taking into the account the kinematic boundary conditions, the system equations of motion in structural node DOF can be expressed as

$$\begin{bmatrix}[M_b] & 0\\ 0 & [M_m]\end{bmatrix}\begin{Bmatrix}\ddot{W}_b\\ \ddot{W}_m\end{Bmatrix}$$
$$+\left(\begin{bmatrix}[K_b] & [K_{bm}]\\ [K_{mb}] & [K_m]\end{bmatrix}+\begin{bmatrix}[K_b^s] & 0\\ 0 & 0\end{bmatrix}+\begin{bmatrix}0 & [K_{bm}^{sR}]\\ [K_{mb}^{sR}] & [K_m^{sR}]\end{bmatrix}+\begin{bmatrix}[K_b^R] & [K_{bm}^R]\\ [K_{mb}^R] & 0\end{bmatrix}-\begin{bmatrix}[K_b^{N_{\Delta T}}] & 0\\ 0 & 0\end{bmatrix}\right.$$
$$+\begin{bmatrix}[K1_b] & [K1_{bm}]\\ [K1_{mb}] & 0\end{bmatrix}+\begin{bmatrix}[K1_b^{N_t}] & 0\\ 0 & 0\end{bmatrix}+\begin{bmatrix}[K1_b^{N_m}] & 0\\ 0 & 0\end{bmatrix}+\begin{bmatrix}[K1_b^R] & 0\\ 0 & 0\end{bmatrix}+\begin{bmatrix}[K1_b^{N_{CR}}] & 0\\ 0 & 0\end{bmatrix} \quad (2.166)$$
$$\left.+\begin{bmatrix}[K2_b] & 0\\ 0 & 0\end{bmatrix}\right)\begin{Bmatrix}W_b\\ W_m\end{Bmatrix}=\begin{Bmatrix}P_b(t)\\ 0\end{Bmatrix}+\begin{Bmatrix}P_b^{\Delta T}\\ P_m^{\Delta T}\end{Bmatrix}$$

where the top row of Eq. (2.166) represents inertia term, second row - linear stiffness, third row – first order nonlinear stiffness, forth row – second order nonlinear stiffness matrices, and right hand side of the equation includes random pressure fluctuation in time and quasi-steady thermal load.

2.6 Free Vibration

Simplifying the equation of motion Eq.(2.166) to the case of free (unforced) oscillation yields the right hand side equal to zero. Additionally, the assumption of a room temperature environment eliminates thermal stiffness components.

$$\begin{bmatrix}[M_b] & 0\\ 0 & [M_m]\end{bmatrix}\begin{Bmatrix}\ddot{W}_b\\ \ddot{W}_m\end{Bmatrix}$$
$$+\left(\begin{bmatrix}[K_b] & [K_{bm}]\\ [K_{mb}] & [K_m]\end{bmatrix}+\begin{bmatrix}[K_b^s] & 0\\ 0 & 0\end{bmatrix}+\begin{bmatrix}0 & [K_{bm}^{sR}]\\ [K_{mb}^{sR}] & [K_m^{sR}]\end{bmatrix}+\begin{bmatrix}[K_b^R] & [K_{bm}^R]\\ [K_{mb}^R] & 0\end{bmatrix}\right.$$
$$+\begin{bmatrix}[K1_b] & [K1_{bm}]\\ [K1_{mb}] & 0\end{bmatrix}+\begin{bmatrix}[K1_b^{N_t}] & 0\\ 0 & 0\end{bmatrix}+\begin{bmatrix}[K1_b^{N_m}] & 0\\ 0 & 0\end{bmatrix}+\begin{bmatrix}[K1_b^R] & 0\\ 0 & 0\end{bmatrix}+\begin{bmatrix}[K1_b^{N_{CR}}] & 0\\ 0 & 0\end{bmatrix} \quad (2.167)$$
$$\left.+\begin{bmatrix}[K2_b] & 0\\ 0 & 0\end{bmatrix}\right)\begin{Bmatrix}W_b\\ W_m\end{Bmatrix}=\begin{Bmatrix}0\\ 0\end{Bmatrix}$$

The free vibration model is developed to be used further in this work for the purpose of validation of the nonlinear stiffness terms.

3. Fatigue Life Formulation

3.1 Fatigue Phenomenon

Experience has shown that a structure can be damaged not only by passing a certain levels of static stresses applied momentarily but also through multi-cycle loading at a considerably lower stress levels. This phenomenon is called fatigue. The most common design tools for the fatigue life prediction are the S-N curves relating the failure stress levels to the number of load cycles. The S-N curves are obtained experimentally as a result of multi-specimen tests. Since there are many geometrical configurations of structures and many loading conditions, it is impossible to obtain reliable data for each arbitrary design. Also the most common practice when conducting fatigue tests is the use of periodic (often harmonic) excitation with constant amplitude and zero-mean value which does not reflect real load characteristics.

3.2 Time Domain vs. Frequency Domain Approach

As mentioned in Chapter 1, the fatigue life estimation can be attempted departing from either the time history or the frequency domain of the curved panel response. In the time domain, a stochastic process can be described by statistical characteristics. Basic parameters defined in the time domain are

Mean Value

$$m = \frac{1}{T}\int_0^T X(t)dt \tag{3.1}$$

Variance

$$\sigma^2 = \frac{1}{T}\int_0^T [X(t) - m]^2 dt \tag{3.2}$$

Standard Deviation

$$\sigma = +\sqrt{\sigma^2} \tag{3.3}$$

Skewness

$$skew = E\left[\left(\frac{X(t)-m}{\sigma}\right)^3\right] \tag{3.4}$$

and Kurtosis

$$kur = E\left[\left(\frac{X(t)-m}{\sigma}\right)^4\right]-3 \tag{3.5}$$

The mean value is the average of all values, the variance and the standard deviation are measures of the departure from the mean value. The skewness measures the departure from the symmetrical distribution. Skewness equal to zero indicates the symmetrical distribution with respect to the mean value. Negative skewness refers to the tail of the distribution shifted to the right of the mean value, and positive skewness refers to the tail being shifted to the left (Figure 3.1).

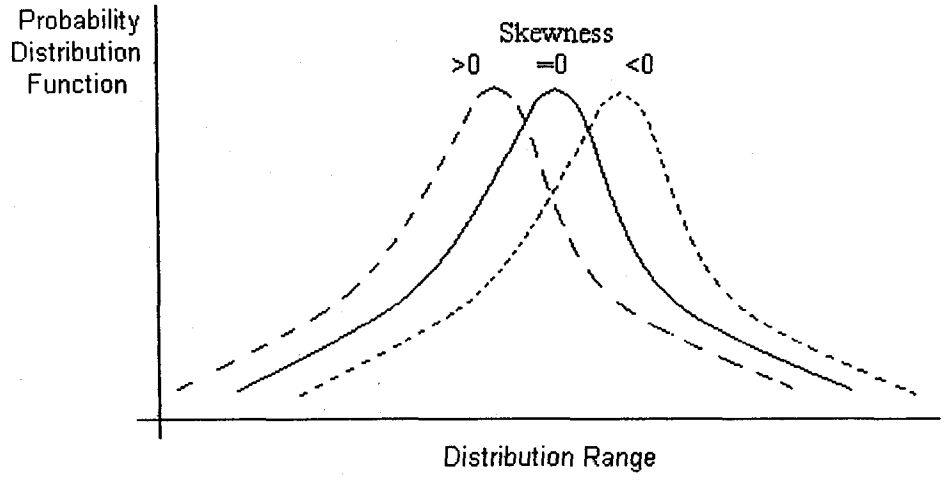

Figure 3.1 Skewness

The kurtosis is the measure indicating the departure from the normal distribution. Zero value represents a perfectly Gaussian distribution. A negative value of kurtosis is obtained when the peak is lower than for the normal distribution and the positive value when the peak is higher (Figure 3.2).

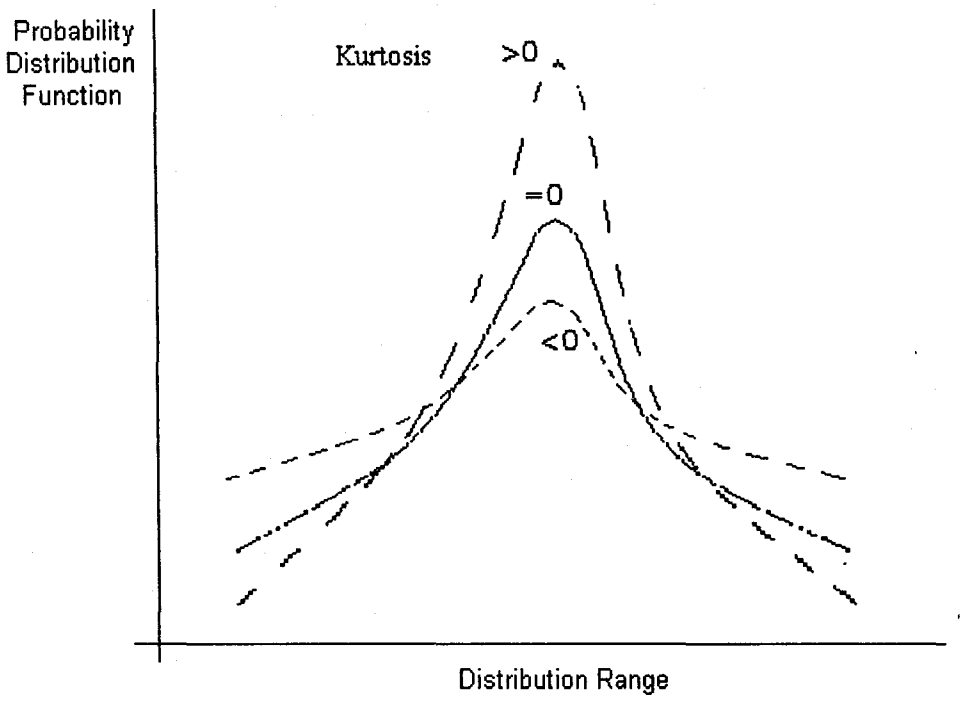

Figure 3.2 Kurtosis

Other statistical values can be defined in a descriptive way. The up-crossing spectrum or up-crossing intensity $\mu(u)$ is equal to the average number of up-crossings per unit time, of a level u by $x(t)$ as a function of u. It is seen in Figure 3.3 that this value can differ significantly for the narrowband and broadband signals. The mean frequency, f_0, is the average number of rainflow cycles (see Chapter 1) per unit time. The irregularity factor, α, is the measure of how dense the local extremes are relative to the mean frequency f_0. For a narrowband signal there is only one local maximum between

up-crossing of the mean level. This situation refers to the irregularity factor α being equal to 1 (Figure 3.3a). On the other hand when the signal is broadband (Figure 3.3b) irregularity factor α goes to zero. It is worth noticing here that the damage accumulation process in most of the theories depends only upon the values and number of the local extremes. The sequence of appearance is not considered. Experimental studies have shown that this is not always the case i.e. for an aluminum riveted airframe.[76] However reliable data relating the sequence of the occurrences to the damage accumulation is not available, and this work is dealing with composite structures. Therefore, the assumption that the applied loading sequence is not of importance is adopted in this work.

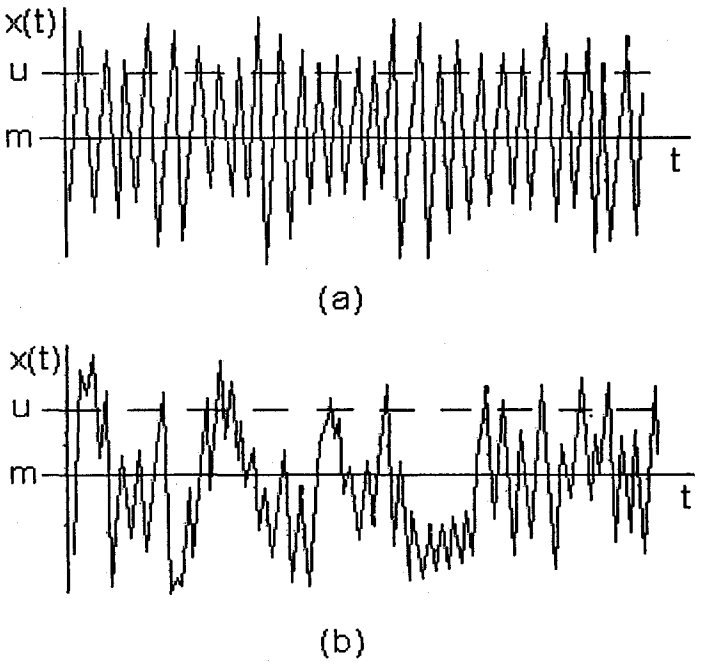

Figure 3.3 Up-Crossing and Its Irregularity for (a) Narrowband and (b) Broadband Signals

The description of a stochastic process in the frequency domain is usually based on its power spectrum.[94] The spectral (Fourier) analysis of a stochastic processes

considers a process as a mixture of periodic components (e.g. sine or cosine waves) with different frequencies and, among others, it enables one to obtain a conception of intensity with which particular frequencies are contained in the investigated stochastic process. Defining the correlation function as

$$R(\tau) = E[X(t)X(t+\tau)] \tag{3.6}$$

The power spectral density function of a weakly stationary stochastic process is a real and non-negative function defined as

$$S(\omega) = \frac{1}{2\pi}\int_{-\infty}^{\infty} e^{-j\omega\tau} R(\tau) d\tau \tag{3.7}$$

Since $R(\tau)$ is an even function of τ, it can be written as

$$S(\omega) = \frac{1}{\pi}\int_{0}^{\infty} R(\tau)\cos(\omega\tau) d\tau \tag{3.8}$$

The reverse relations stand

$$R(\tau) = \int_{-\infty}^{\infty} e^{-j\omega\tau} S(\omega) d\omega \tag{3.9}$$

and

$$R(\tau) = 2\int_{0}^{\infty} S(\omega)\cos(\omega\tau) d\omega \tag{3.10}$$

The spectral analysis of a structural response is a very robust tool, however its application is limited to Gaussian or performing some initial transformations slightly non-Gausian processes. This is not the case for random large amplitude vibrations of shallow shells exposed to elevated thermal environments. Therefore only the time domain approach is used in this work.

3.3 Peak Counting

3.3.1 Rainflow Counting Method

The procedure to calculate strains and stresses using the FE method will be presented as a part of the solution procedure in Chapter 4. Once the maximum stress (for isotropic materials) or strain (for composites) time history is obtained, one can attempt to estimate the fatigue life. The first step of this procedure involves peak counting. As introduced briefly in Section 1.5.3 the Rainflow Counting Method was developed in 1968 by Matsushi and Endo[80] as a complicated recursive algorithm. Since then, the concept was redeveloped in simplified local formulations by Rychlik,[80] and Bishop and Sherratt.[95] This work utilizes Rychlik's formulation.

In fatigue applications it is generally agreed that the shape of the load connecting two intermediate local extremes is of no importance, and only the values of local minima and maxima of the load sequence influence the lifetime. Consequently, the load process can be characterized by its sequence of local extremes, also called turning points (TP). In Figure 3.4 maxima are marked with M_i and minima are marked with m_i.

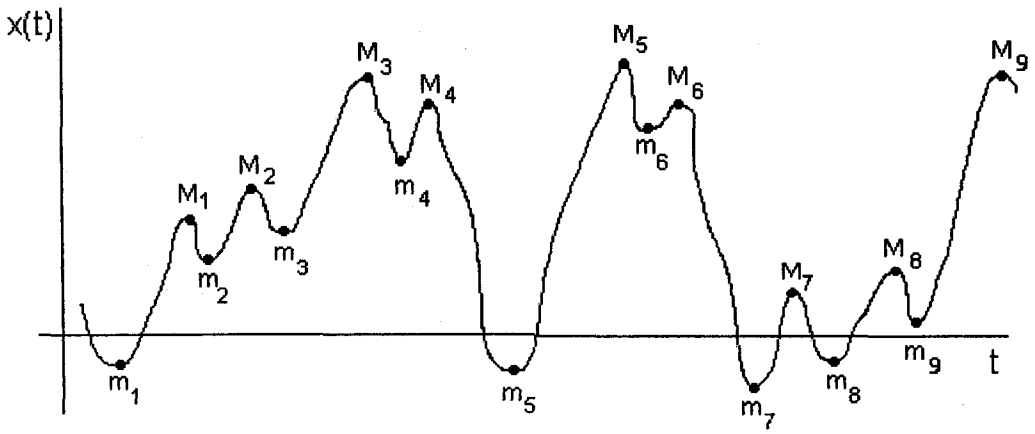

Figure 3.4 Load Curve with TP Marked

The RFC method is designed to catch both slow and rapid variations of the load by forming cycles by pairing high maxima with low minima even if they are separated by intermediate extremes. Each local maximum is used as the maximum of a hysteresis loop with an amplitude that is computed by the rainflow algorithm. What the algorithm does is to count hysteresis cycles for the stress or strain response in the time vs. stress or strain plane, as shown in Figure 3.5. There are two (standing and hanging) rainflow hysteresis cycles shown in Figure 3.5. How to determine a single rainflow cycle is shown in detail in Figure 3.6. The formal definition of RFC reads as follows:

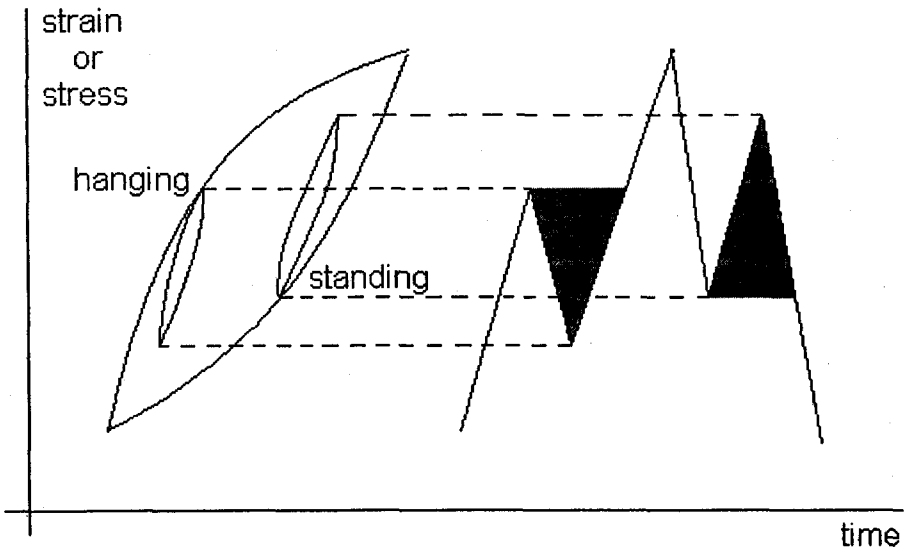

Figure 3.5 Hysteresis Loop in the Stress-Strain

Let $X(t)$, $0 \le t \le T$, be a function with finitely many local maxima of height M_k occurring at times t_k. For the k^{th} maximum at time t_k define the following right and left minima

$$m_k^- = \inf\{x(t): t_k^- < t < t_k\}$$
$$m_k^+ = \inf\{x(t): t_k < t < t_k^+\} \qquad (3.11)$$

where

$$t_k^- = \begin{cases} \sup\{t \in [0, t_k) : X(t) > X(t_k)\}, if\ X(t) > X(t_k)\ for\ some\ t \in [0, t_k) \\ 0, otherwise \end{cases}$$

$$t_k^+ = \begin{cases} \sup\{t \in (t_k, T] : X(t) > X(t_k)\}, if\ X(t) > X(t_k)\ for\ some\ t \in (t_k, T] \\ T, otherwise \end{cases} \quad (3.12)$$

Then the k^{th} RFC is defined as (m_k^{RFC}, M_k), where

$$m_k^{RFC} = \begin{cases} \max(m_k^-, m_k^+), if\ t_k^+ < T \\ m_k^-, if\ t_k^+ = T \end{cases} \quad (3.13)$$

This strict mathematical definition can be re-paraphrased and explained graphically (Figure 3.6) as follows:

From each local maximum, M_k, one shall try to reach above the same level, in the backward (left) or forward (right) directions, with as small a downward excursion as possible. The minima, m_k^- and m_k^+ on each side are defined. That minimum which represents the smallest deviation from the maximum M_k is defined as the corresponding rainflow minimum m_k^{RFC}.

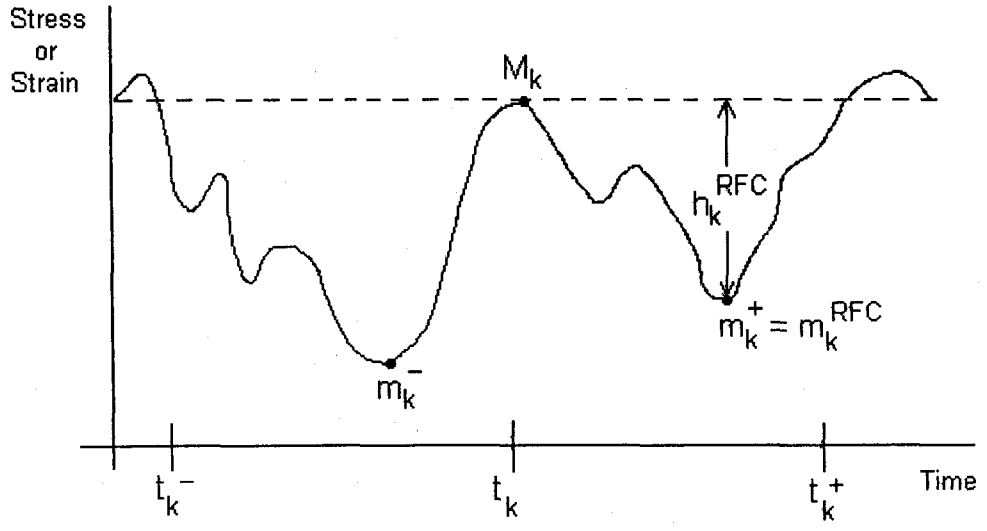

Figure 3.6 Definition of RFC Cycle

Consider t_k being the time of the k^{th} local maximum with the corresponding rainflow amplitude of the attached hysteresis loop being

$$S_k^{RFC} = \frac{\left(M_k - m_k^{RFC}\right)}{2} = \frac{h_k^{RFC}}{2} \tag{3.14}$$

For complicated loads (i.e. chaotic motion), where there are infinitely many local extremes in a final interval, the rainflow is redefined as follows. Rainflow minimum $m^{RFC}(t)$ for all time points t of a load $x(t)$ is defined in such a way that the rainflow amplitude $x(t) - m^{RFC}(t)$ is zero if the point $x(t)$ is not a strict local maximum of the load. It is also possible to divide the set of rainflow cycles into two groups, depending on whether the rainflow minimum occurs before or after the maximum. The two different kinds of cycles occur on an up-going or down-going hysteresis arm, and are called "hanging" or "standing" RFC (Figure 3.5), respectively. The "standing" cycles are defined as $\left(m_k^{RFC}, M_k\right)$, when the minimum occurs before maximum, and the hanging cycles are defined as $\left(M_k, m_k^{RFC}\right)$, when the minimum occurs after the maximum. The RFC counting can be interpreted as a pair of a minimum m_k^{RFC} and the maximum M_k, where the amplitude is the most important characteristic for fatigue evaluation. In fatigue estimates, a cycle is often represented as a range-mean pair. The range is defined as

$$range = M_K - m_k^{RFC} \tag{3.15}$$

and the mean cycle as

$$mean = \frac{\left(M_k + m_k^{RFC}\right)}{2} \tag{3.16}$$

Values defined in Eqs. (3.14-16) are presented in Figure 3.7.

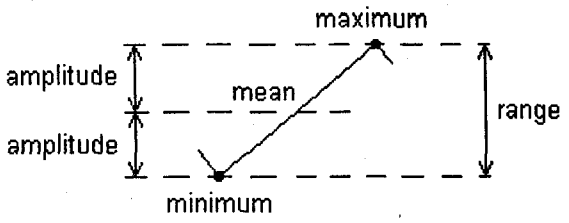

Figure 3.7 Definition of Amplitude, Range and Mean

Let $\{X(t): t \geq 0\}$ be a stochastic process in continuous time with discrete states from the set $I = \{0,1,2,...\}$ (the states are denoted by non-negative integers, for simplicity). The stochastic process $\{X(t): t \geq 0\}$ is called the Markov process if

$$P(X(\tau) = j \mid X(t) = i, X(t_n) = i_n, ..., X(t_1) = i_1) = P(X(\tau) = j \mid X(t) = i) \qquad (3.17)$$

for arbitrary $0 \leq t_1 < t_2 < ... < t_n < t \leq \tau$ and $i_1, ..., i_n, i, j \in I$ (the so-called Markov property). The probabilities of the Eq. (3.17) are called transition probabilities. If these probabilities do not depend on particular values of t and τ but only on their difference, then such a Markov process is called homogenous and the transition probabilities are denoted by

$$p_{ij}(\tau - t) = P(X(\tau) = j \mid X(t) = i) \qquad (3.18)$$

Markov chains are an analogy of Markov processes in discrete time. An arbitrary load sequence of TP will be called a Markov Chain of TP if it forms a Markov chain, i.e., if the distribution of a local extremum depends only on the value of the previous extremum. The elements in the histogram matrix of min-to-max cycles and max-to-min cycles are equal to the observed number of transitions from a minimum to a maximum (or vice versa) of specified height. Therefore, the probabilistic structure of the Markov chain of

TP is fully defined by the expected histogram matrix of min-to-max and max-to-min cycles, referred to as Markov Matrices. The rainflow matrix F^{RFC} is illustrated in Figure 3.8.

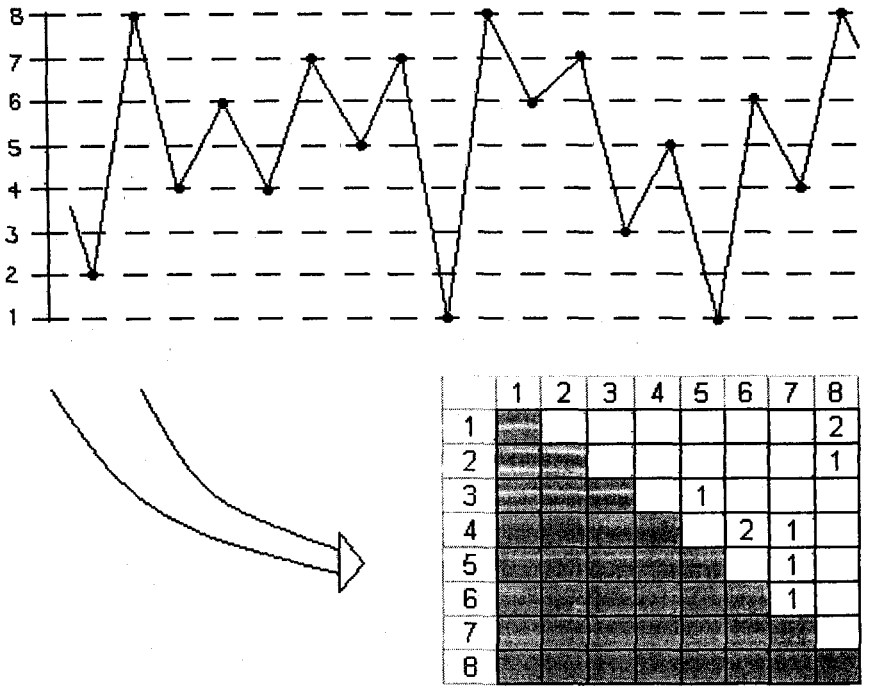

Figure 3.8 Rainflow Matrix

3.3.2 Peak Through Valley Counting

In order to demonstrate the difference between RFC and other simpler methods, the Peak Through Valley Counting (PTVC) method is introduced. The PTVC definition reads: Let $X(t)$, $0 \le t \le T$, be a function with finitely many load maximum of height M_k occurring at times t_k. Then the k^{th} max-min cycle is defined as (M_k, m_{k+1}) and is the minimum succeeding M_k. By inversion min-max cycle can be defined. The min-max matrix F and max-min matrix $\hat{F}$ are illustrated in Figure 3.9.

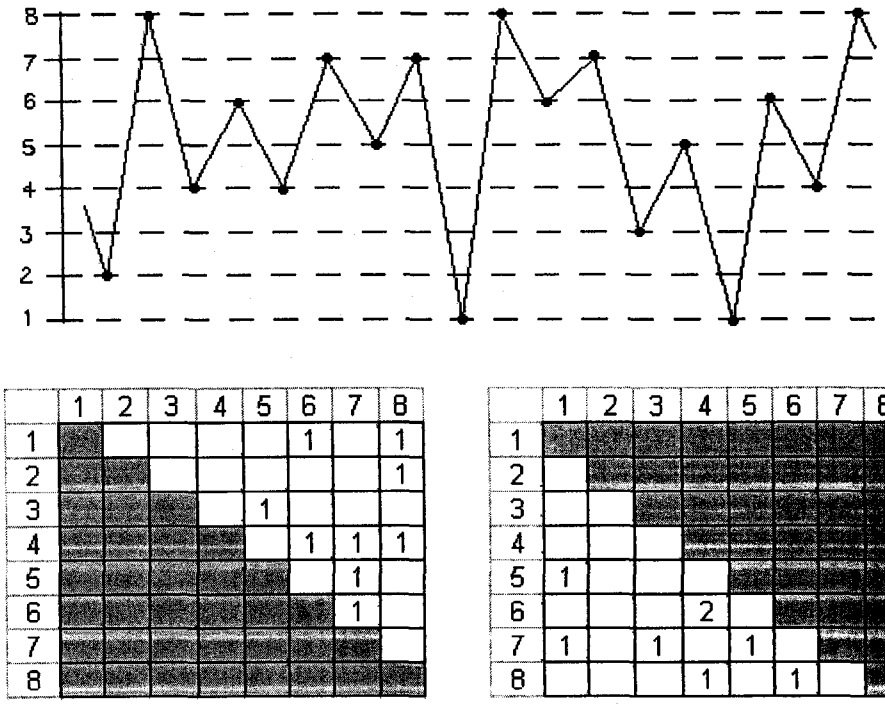

Figure 3.9 Min-max and Max-min Matrices

The observed cycles can be presented as a cloud of points in the min-max plane (Figure 4.5.)

3.4 Damage Accumulation

The concept of Stress-Life Diagrams (S-N Curves) was established by Wöhler in the middle of the 19th century. The diagrams present stress (S) versus number of cycles (N) needed to cause the failure. For the composite materials where significantly different stresses occur in the matrix and the reinforcement, the concept is modified and stress is replaced by strain. Analytically, a typical S-N curve (where S can be either stress or strain) is represented as

$$N(S)=\begin{cases} K S_k^{-\beta} & S_k > S_\infty \\ \infty & S_k \le S_\infty \end{cases} \tag{3.19}$$

where K and β are material properties and in fact they are approximated by E[K] and E[β], respectively, and S_∞ is the fatigue limit. Below the value of S_∞ no damage will be encountered regardless the number of applied cycles. For random oscillations it is apparent that the structure will be exposed to various amplitudes of vibration, each of them occurring with different frequency. Therefore the RFC method and S-N curve must be combined by means of some damage accumulation theory. Fatigue damage theories were investigated[83] for step fatigue tests, with the conclusion that Palmgren-Miner theory[84,85] was as accurate as the more complex theories. Consequently, Palmgren-Miner theory could be recognized as suitable for application to the acoustic fatigue problem.

For each strain amplitude, the contribution to the total damage is calculated. If the strain amplitude S_k requires $N(S_k)$ cycles for the damage to occur, the contribution to the total damage due to n_k cycles at this amplitude, where $n_k < N(S_k)$, is equal $n_k/N(S_k)$. Accordingly, the failure occurs when

$$D=\sum_{k=1}\left(\frac{n_K}{N(S_K)}\right) \tag{3.20}$$

reaches unitary value. Combining Equations (3.19) and (3.20) in the time domain, with the assumption that if the k^{th} cycle has an amplitude S_k causing damage equal to $1/N(S_k)$ for random ergodic stationary processes, the total expected value of damage experienced by the structure up to time t is

$$E[D(t)]=E\left[\sum_{t<t_k}\frac{1}{N(S_k)}\right]=E\left[\frac{1}{K}\sum_{t<t_K}S_k^{\beta}\right]=E\left[\frac{D_\beta(t)}{K}\right] \tag{3.21}$$

where K and β are experimentally determined constants characterizing S-N curve for a particular material. Assuming that $E[K] \cong K$ Eq. (3.20) simplifies to

$$E[D(t)] \cong \frac{1}{K} E[D_\beta(t)] \tag{3.22}$$

and the fatigue life is equal

$$T_f = \frac{1}{E[D(t)]} \tag{3.23}$$

and it corresponds to the total damage value of Eq. (3.20) being equal 1.

4. Solution Procedure

In this section the steps and considerations regarding the solution procedure are addressed. First, the solution of the linear vibration problem is dealt with. The mode shapes obtained at this step allow for the expansion theorem to be used and the modal transformation procedure is detailed. Two types of convergence are investigated. Firstly, for the linear vibration problem, the convergence of the natural frequencies upon discrestization is sought. Secondly, the number of modes remaining in the approximation for the nonlinear vibration problem are considered so the modal convergence is reached.

As a part of the preliminary fundamental studies, the free undamped vibration problem is studied. In the section related to this problem, an iterative procedure for setting the initial conditions for the periodic response is presented.

Subsequently, the loadings of the panel are discussed. The thermal effects on the panel response are followed by acoustic pressure fluctuation behavior. Two types of random pressure fluctuations are used – a simulated truncated white noise, and data produced by an in-flight microphone recording.

Finally, the post-processing of the displacement solution and the fatigue life estimation are brought into consideration. These include strain and stress estimation using the concept of reduced integration,[100,101] determination of the transient and the steady-state response and use of statistical tools for fatigue prediction.

4.1 Linear Vibration Problem

In order to attempt modal transformation of the equation of motion in the structural DOF, Eq. (2.167), the linear eigenproblem is solved first to obtain eigenvectors

needed for the modal reduction. In order to formulate linear vibration problem, nonlinear stiffness matrices [K1] and [K2] are neglected and Eq. (2.167) becomes

$$\left(-\omega_r^2[M]+[K_L]\right)\{\phi\}^{(r)}=0 \tag{4.1}$$

where $\{\phi\}^{(r)}$ is the r^{th} eigenvector, ω_r is the corresponding natural frequency, and

$$[M]=\begin{bmatrix}[M_b] & 0\\ 0 & [M_m]\end{bmatrix} \tag{4.2}$$

with

$$[M_b]=\begin{bmatrix}[M_t] & [M_{t\psi}]\\ [M_{\psi t}] & [M_\psi]\end{bmatrix} \tag{4.2a}$$

Similarly

$$[K_L]=\begin{bmatrix}[K_{Lb}] & [K_{Lbm}]\\ [K_{Lmb}] & [K_{Lm}]\end{bmatrix}=[K\ ]+[K^s]+[K^{sR}]+[K^R] \tag{4.3}$$

with

$$[K_{Lb}]=\begin{bmatrix}[K_t] & [K_{t\psi}]\\ [K_{\psi t}] & [K_\psi]\end{bmatrix} \tag{4.3a}$$

$$[K_{Lbm}]=\begin{bmatrix}0\\ [K_{\psi m}]\end{bmatrix}=[K_{Lmb}]^T \tag{4.3b}$$

The eigenvectors $\{\phi\}^{(r)}$ consist of bending and inplane modes

$$\{\phi\}^{(r)}=\begin{Bmatrix}\phi_b\\ \phi_m\end{Bmatrix}^{(r)} \tag{4.4}$$

with

$$\{\phi_b\}^{(r)}=\begin{Bmatrix}\phi_t\\ \phi_\psi\end{Bmatrix}^{(r)} \tag{4.4a}$$

4.2 Transformation of the Equation of Motion into Modal Coordinates

4.2.1 General Case

Expressing the panel response as

$$\{W\}=\begin{Bmatrix}W_b\\W_m\end{Bmatrix}=\sum_{r=1}^{n}q_r(t)\begin{Bmatrix}\phi_b\\\phi_m\end{Bmatrix}^{(r)}=[\phi]\{q\} \tag{4.5}$$

the diagonal modal mass and linear stiffness matrices are

$$[\overline{M}]=[\phi]^T[M][\phi] \tag{4.6}$$

$$[\overline{K_L}]=[\phi]^T[K_L][\phi] \tag{4.7}$$

Denoting quadratic terms of Eq. (2.167) as

$$[K1]=[K1^{\theta}]+[K1^{N_r}]+[K1^{N_m}]+[K1^{R}]+[K1^{C_R}] \tag{4.8}$$

and cubic term of Eq. (2.167) as

$$[K2]=\begin{bmatrix}[K2_b] & 0\\ 0 & 0\end{bmatrix} \tag{4.9}$$

the nonlinear stiffness matrices [K1] and [K2] can be expressed as the sum of products of modal coordinates and nonlinear modal stiffness matrices as[17,18]

$$[\overline{K_q}]=[\phi]^T\sum_{r=1}^{n}q_r(t)[K1(\phi)]^{(r)}[\phi] \tag{4.10}$$

and

$$[\overline{K_{qq}}]=[\phi]^T\sum_{r=1}^{n}\sum_{s=1}^{n}q_r(t)q_s(t)[K2(\phi)]^{(rs)}[\phi] \tag{4.11}$$

where the super indexes of those nonlinear stiffness matrices denote that they are assembled from the corresponding element nonlinear stiffness matrices, see Eq. (2.165). Those element nonlinear stiffness matrices are evaluated with the corresponding element components $\{w\}^{(r)}$ obtained from the known system mode $\{\phi\}^{(r)}$.

The modal load vector consisting of the quasi-steady thermal load and the random pressure fluctuation takes the form

$$\{\overline{P}\} = [\phi]^T (\{P_{\Delta T}\} + \{P(t)\}) \tag{4.12}$$

Introducing a structural modal damping, the system of coupled equations of motion expressed in the truncated modal degrees of freedom can be written as

$$[\overline{M}]\{\ddot{q}\} + 2\zeta_r \omega_r \overline{M}_r [I]\{\dot{q}\} + ([\overline{K_L}] + [\overline{K_q}] + [\overline{K_{qq}}])\{q\} = \{\overline{P}\} \tag{4.13}$$

where $[\overline{M}] = \overline{M}_r [I]$, and $\overline{M}_r$ is a scalar and $[I]$ is the unit diagonal matrix.

4.2.2 Case with Inplane Inertia Neglected

Since no prior work has been found on large amplitude random response of shallow shells to combined acoustic and thermal loads, the validation of the present formulation will be conducted by parts in Chapter 5. In order to verify the nonlinear stiffness matrices a comparison with analytical free vibration results will be performed.[10] For free undamped vibration of a shallow shell, modal Equation (4.13) reduces to

$$[\overline{M}]\{\ddot{q}\} + ([\overline{K_L}] + [\overline{K_q}] + [\overline{K_{qq}}])\{q\} = \{0\} \tag{4.14}$$

and its solution retains the form of Equation (4.5). However, due to mathematical difficulties, classical methods neglect inplane inertia in the equations of motion. Therefore, for the sake of comparison, the FE modal formulation neglecting inertia of inplane motion

$$[M_m]\{\ddot{W}_m\} \cong \{0\} \tag{4.15}$$

was developed.[96] To preserve generality of this formulation, arbitrary force $\{P\} = \{P(t) + \{P_{\Delta t}\}\} = \lfloor \{P_b\}\{P_m\} \rfloor^T$ is kept in the derivation. Solving the second of the Eq. (2.166) with the assumption of Eq. (4.15) yields

$$\{W_m\} = \left([K_m] + [K_m^{sR}]\right)^{-1}\left(\{P_m\} - [K_{mb}] + [K_{mb}^{R}] + \{K_{mb}^{sR}] + [K1_{mb}]\right)\{W_b\} \quad (4.16)$$

while the first of the Eq. (2.166) reads

$$\begin{aligned}
&[M_b]\{\ddot{W}_b\} + \\
&\left([K_b] + [K_b^s] + [K_b^R] - [K_b^{N_{\Delta T}}] + [K1_b] + [K1^{N_b}]\right. \\
&\left. + [K1_b^{N_m}] + [K1_b^R] + [K1_b^{N_R}] + [K2_b]\right)\{W_b\} \\
&+ \left([K_{bm}] + [K_{bm}^R] + [K_{bm}^{sR}] + [K1_{bm}]\right)\{W_m\} = \{P_b\}
\end{aligned} \quad (4.17)$$

Substituting Eq. (4.16) into Eq. (4.17) yields

$$\begin{aligned}
&[M_b]\{\ddot{W}_b\} \\
&+ [\ [K_b] + [K_b^s] + [K_b^R] - [K_b^{N_{\Delta T}}] + [K1_b] + [K1^{N_b}] \\
&+ [K1_b^{N_m}] + [K1_b^R] + [K1_b^{N_R}] + [K2_b] \\
&- \underline{\left([K_{bm}] + [K_{bm}^R] + [K_{bm}^{sR}] + [K1_{bm}]\right)} \\
&\quad \underline{\left([K_m] + [K_m^{sR}]\right)^{-1}\left([K_{mb}] + [K_{mb}^R] + [K_{mb}^{sR}] + [K1_{mb}]\right)]\{W_b\}} \\
&+ \left([K_{bm}] + [K_{bm}^R] + [K_{bm}^{sR}] + [K1_{bm}]\right)\left([K_m] + [K_m^{sR}]\right)^{-1}\{P_m\} = \{P_b\}
\end{aligned} \quad (4.18)$$

and it represents the equation of motion expressed in terms of bending displacement $\left(\{W_b\} = \left\lfloor \{W_t\}^T, \{\psi_x\}^T, \{\psi_y\}^T \right\rfloor\right)$ only. Expanding the underlined portion of Eq. (4.18), 16 new terms are generated. Nine of them are linear:

$$-[K_{bm}]\left([K_m] + [K_m^{sR}]\right)^{-1}[K_{mb}] \quad (4.18a)$$

$$-[K_{bm}]\left([K_m] + [K_m^{sR}]\right)^{-1}[K_{mb}^R] \quad (4.18b)$$

$$-[K_{bm}]\left([K_m] + [K_m^{sR}]\right)^{-1}[K_{mb}^{sR}] \quad (4.18c)$$

$$-[K_{bm}^R]\left([K_m] + [K_m^{sR}]\right)^{-1}[K_{mb}] \quad (4.18d)$$

$$-[K_{bm}^R]\left([K_m] + [K_m^{sR}]\right)^{-1}[K_{mb}^R] \quad (4.18e)$$

$$-[K_{bm}^R]\left([K_m] + [K_m^{sR}]\right)^{-1}[K_{mb}^{sR}] \quad (4.18f)$$

$$-\left[K_{bm}^{sR}\right]\left(\left[K_m\right]+\left[K_m^{sR}\right]\right)^{-1}\left[K_{mb}\right] \tag{4.18g}$$

$$-\left[K_{bm}^{sR}\right]\left(\left[K_m\right]+\left[K_m^{sR}\right]\right)^{-1}\left[K_{mb}^{R}\right] \tag{4.18h}$$

$$-\left[K_{bm}^{sR}\right]\left(\left[K_m\right]+\left[K_m^{sR}\right]\right)^{-1}\left[K_{mb}^{sR}\right] \tag{4.18j}$$

six – first order nonlinear

$$-\left[K_{bm}\right]\left(\left[K_m\right]+\left[K_m^{sR}\right]\right)^{-1}\left[K1_{mb}\right] \tag{4.18k}$$

$$-\left[K_{bm}^{R}\right]\left(\left[K_m\right]+\left[K_m^{sR}\right]\right)^{-1}\left[K1_{mb}\right] \tag{4.18m}$$

$$-\left[K_{bm}^{sR}\right]\left(\left[K_m\right]+\left[K_m^{sR}\right]\right)^{-1}\left[K1_{mb}\right] \tag{4.18n}$$

$$-\left[K1_{bm}\right]\left(\left[K_m\right]+\left[K_m^{sR}\right]\right)^{-1}\left[K_{mb}\right] \tag{4.18p}$$

$$-\left[K1_{bm}\right]\left(\left[K_m\right]+\left[K_m^{sR}\right]\right)^{-1}\left[K_{mb}^{R}\right] \tag{4.18q}$$

$$-\left[K1_{bm}\right]\left(\left[K_m\right]+\left[K_m^{sR}\right]\right)^{-1}\left[K_{mb}^{sR}\right] \tag{4.18r}$$

and one - second order nonlinear

$$-\left[K1_{bm}\right]\left(\left[K_m\right]+\left[K_m^{sR}\right]\right)^{-1}\left[K1_{mb}\right] \tag{4.18s}$$

Moreover, it is noticed that the term $\left[K1_b^{N_m}\right]$ depends on the inplane displacement $\{W_m\}$, therefore it will also be affected by the assumption of neglecting the inplane inertia. Recalling the membrane displacement vector of Eq. (4.16)

$$\begin{aligned}\{W_m\} &= \left(\left[K_m\right]+\left[K_m^{sR}\right]\right)^{-1}\left(\{P_m\}-\left[K_{mb}\right]+\left[K_{mb}^{R}\right]+\left[K_{mb}^{sR}\right]+\left[K1_{mb}\right]\right)\{W_b\} \\ &= \left(\left[K_m\right]+\left[K_m^{sR}\right]\right)^{-1}\left(\{P_m\}-\sum_{r=1}^{n} q_r(t)\left[K_{mb}\right]\{\phi_b\}^{(r)}-\sum_{r=1}^{n} q_r(t)\left[K_{mb}^{R}\right]\{\phi_b\}^{(r)}\right. \\ &\qquad \left.-\sum_{r=1}^{n} q_r(t)\left[K_{mb}^{sR}\right]\{\phi_b\}^{(r)}-\sum_{r=1}^{n}\sum_{s=1}^{n} q_r(t)q_s(t)\left[K1_{mb}\right]^{(r)}\{\phi_b\}^{(s)}\right)\end{aligned} \tag{4.19}$$

Therefore, the membrane vector of Eq. (4.19) can be expressed in a form of

$$\{W_m\}=\{W_m^*\}-\left(\sum_{r=1}^{n}q_r(t)\{W_m\}^{(r)}+\sum_{r=1}^{n}q_r(t)\{W_m^R\}^{(r)}+\sum_{r=1}^{n}q_r(t)\{W_m^{sR}\}^{(r)}+\sum_{r=1}^{n}\sum_{s=1}^{n}q_r(t)q_s(t)\{W_m\}^{(rs)}\right) \tag{4.20}$$

where $\{W_m\}^{(r)}=([K_m]+[K_m^{sR}])^{-1}[K_{mb}]\{\phi_b\}^{(r)}$, $\{W_m^R\}^{(r)}=([K_m]+[K_m^{sR}])^{-1}[K_{mb}^R]\{\phi_b\}^{(r)}$, $\{W_m^{sR}\}^{(r)}=([K_m]+[K_m^{sR}])^{-1}[K_{mb}^{sR}]\{\phi_b\}^{(r)}$, $\{W_m\}^{(rs)}=([K_m]+[K_m^{sR}])^{-1}[K1_{mb}]^{(r)}\{\phi_b\}^{(s)}$, and $\{W_m^*\}=([K_m]+[K_m^{sR}])^{-1}\{P_m\}$.

and the new $[K1_b^{N_m}]$ matrix is built as the following summation:

$$[K1_b^{N_m}]=[K_b^{*N_m}]-\sum_{r=1}^{n}q_r(t)[K1^{N_m}]^{(r)}-\sum_{r=1}^{n}q_r(t)[K1^{N_mR}]^{(r)}-\sum_{r=1}^{n}q_r(t)[K1^{N_msR}]^{(r)}-\sum_{r=1}^{n}\sum_{s=1}^{n}q_r(t)q_s(t)[K2^{N_m}]^{(rs)} \tag{4.21}$$

In particular, it is observed that this operation will yield a second order nonlinear term, $[K2_b^{N_m}]$, and the final equation reads (assuming that inplane force $\{P_m\}$is associated only with thermal load, superscript (*) is replaced with ΔT):

$$\begin{aligned}
&[M_b]\{\ddot{W}_b\}\\
&+[[K_b]+[K_b^s]+[K_b^R]-[K_b^{\Delta T}]+[K_b^{\Delta T N_m}]-[K_{bm}]([K_m]+[K_m^{sR}])^{-1}[K_{mb}]\\
&-[K_{bm}]([K_m]+[K_m^{sR}])^{-1}[K_{mb}^R]-[K_{bm}]([K_m]+[K_m^{sR}])^{-1}[K_{mb}^{sR}]\\
&-[K_{bm}^R]([K_m]+[K_m^{sR}])^{-1}[K_{mb}]-[K_{bm}^R]([K_m]+[K_m^{sR}])^{-1}[K_{mb}^R]\\
&-[K_{bm}^R]([K_m]+[K_m^{sR}])^{-1}[K_{mb}^{sR}]-[K_{bm}^{sR}]([K_m]+[K_m^{sR}])^{-1}[K_{mb}]\\
&-[K_{bm}^{sR}]([K_m]+[K_m^{sR}])^{-1}[K_{mb}^R]-[K_{bm}^{sR}]([K_m]+[K_m^{sR}])^{-1}[K_{mb}^{sR}]\\
&+[K1_b]+[K1_b^{N_b}]-[K1_b^{N_m}]-[K1_b^{N_mR}]-[K1_b^{N_msR}]+[K1_b^R]+[K1_b^{N_R}]\\
&-[K_{bm}]([K_m]+[K_m^{sR}])^{-1}[K1_{mb}]-[K_{bm}^R]([K_m]+[K_m^{sR}])^{-1}[K1_{mb}]\\
&-[K_{bm}^{sR}]([K_m]+[K_m^{sR}])^{-1}[K1_{mb}]-[K1_{bm}]([K_m]+[K_m^{sR}])^{-1}[K_{mb}]\\
&-[K1_{bm}]([K_m]+[K_m^{sR}])^{-1}[K_{mb}^R]-[K1_{bm}]([K_m]+[K_m^{sR}])^{-1}[K_{mb}^{sR}]\\
&+[K2_b]-[K1_{bm}]([K_m]+[K_m^{sR}])^{-1}[K1_{mb}]-[K2^{N_m}]\{W_b\}=\{P_b\}
\end{aligned} \tag{4.22}$$

Experience has shown that all (linear, first and second order nonlinear) modal equation coefficients are affected by neglecting the inplane inertia. However the differences for linear, and first order nonlinear terms are minor -- usually not greater than 1%.[96] Based on numerous study cases, substantial differences always occur for the second order nonlinear terms, which become[96]

$$[K2_b]-[K1_{bm}]([K_m]+[K_m^{sR}])^{-1}[K1_{mb}]-[K2^{N_m}] \tag{4.22a}$$

The ambiguity mentioned above will be discussed and illustrated with examples in Chapter 5.

The equation of motion, Eq. (4.22) is written in terms of the bending displacement. The response of a panel becomes

$$\{W_b\}=\sum_{r=1}^{n} q_r(t)\{\phi_b\}^{(r)}=[\phi_b]\{q\} \tag{4.23}$$

where $\{\phi_b\}^{(r)}$ are eigenvectors obtained as a solution of the eigenproblem expressed in the bending degrees of freedom only

$$\left(-\omega_r^2[M_b]+[K_{Lb}]\right)\{\phi_b\}^{(r)}=0 \tag{4.24}$$

and the modal equation becomes

$$[\overline{M_b}]\{\ddot{W}_b\}+([\overline{K}_{Lb}]+[\overline{K}_{qb}]+[\overline{K}_{qqb}])\{W_b\}=\{\overline{P}\} \tag{4.25}$$

The modal transformation and the solution procedure follow exactly for the one where the inplane inertia is not neglected, with

$$[\overline{M_b}]=[\phi_b]^T[M_b][\phi_b] \tag{4.25a}$$

$$[\overline{K_b}]=[\phi_b]^T[K_{Lb}][\phi_b] \tag{4.25b}$$

$$[\overline{K}_{qb}]=\sum_{r=1}^{n} q_r(t)[K1_b(\phi)]^{(r)} \tag{4.25c}$$

$$\left[\overline{K}_{qqb}\right] = \sum_{r=1}^{n}\sum_{s=1}^{n} q_r(t) q_s(t) [K2_b(\phi)]^{(rs)} \tag{4.25d}$$

where $[K_{Lb}]$ is established in lines 2 to 6, $[\overline{K}_{qb}]$ is established in lines 7 to 10, and $[\overline{K}_{qqb}]$ is established in line 11 of Eq. (4.22), respectively.

4.3 The Advantages of the Modal Approach

The main advantage of using the modal approach is computational savings. The number of equations remaining in the solution is usually two or three orders lower comparing to structural DOF approach. For most of the cases, the number of modes needed to obtain modal convergence is less than ten. Moreover – nonlinear stiffness matrices do not need to be reassembled at each integration time step, since they are constant. Also, the time step when performing numerical integration can be larger.

4.4 Convergence Considerations

Two types of solution convergence must be addressed. Firstly, while attempting the solution of the linear vibration problem, convergence to the natural frequency must be reached. To investigate this type of convergence the finite model descretization is refined and the change in the fundamental frequency is calculated. In this work it is assumed that the modal convergence is reached when the refinement of the discretization resulting from doubling the number of nodes on both panel edges causes a fundamental frequency change of less than 2%. It is also worth noting that since the forcing function is assumed uniform over the surface of the panel, symmetry can be exploited and the response of a rectangular panel can be calculated based on the modeling a quarter of the panel.

Next, when performing modal transformation, the question of how many modes need to be retained in the analysis arises. In order to resolve this issue, modal convergence is sought. The nonlinear response of the panel is the linear combination of certain modes and each of them has a certain contribution to the total response. In this work it is assumed that modes which contribute to the total response W_{max}/h by less than 1% and contribute to RMS (W_{max}/h) by less then 2% can be neglected. Since the mode contribution in the total response varies with the forcing function (random vibration), and/or initial conditions enforced (free vibration), the estimation of the modal convergence should be performed over the entire range of the panel response under investigation. Generally a larger number of modes is needed for larger values of W_{max}/h or RMS (W_{max}/h). Crude prediction with respect to the mode contribution can be made based on the analytical solution which states that the contribution of a certain mode is inversely proportional to the third power of the natural frequency associated with the mode.

Both types of convergence criteria are a compromise between the accuracy and the computational cost and can be adjusted by the user according to the objectives and computational capabilities.

4.5 Free Undamped Vibration Problem – Iterative Procedure to Determine Initial Conditions For Periodic Response

It is known that the curved panels under moderately large deflection vibrations may exhibit primarily softening characteristics, and as the deflection increases further – hardening characteristics (Figures 5.1 to 5.3).[10] To investigate these phenomena – before

attempting the solution of the randomly excited and damped vibration problem – fundamental studies of a free undamped system were conducted.

The multimode approach requires the initial conditions to be set in such a manner that the system response is periodic. In this section the derivation of an iterative procedure setting the initial conditions is presented.[96] It is assumed that the initial guess of the shallow shell multimode response (the maximum deflection along with the corresponding frequency) is known. These initial trial values can be obtained from the single mode solution, perturbation methods or other methods.

The modal approach to a free undamped vibration problem, where the solution is sought in the form of Equation (4.5) or (4.23) where n is number of modes considered in the solution, results in the general system of Duffing type modal equations in reduced DOF, recall Equation (4.14)

$$[\overline{M}]\{\ddot{q}\}+([\overline{K}_L]+[\overline{K}_q]+[\overline{K}_{qq}])\{q\}=0$$

where $[\overline{M}]$ and $[\overline{K}_L]$ matrices are diagonal matrices (n x n), and $[\overline{K}_q]$ and $[\overline{K}_{qq}]$ are fully populated (n x n x n) and (n x n x n x n), respectively. Mass normalization yields

$$\{\ddot{q}\}+([\overline{K}_L]+[\overline{K}_q]+[\overline{K}_{qq}])\{q\}=0 \tag{4.26}$$

where each of the matrices $[\overline{K}_L]$, $[\overline{K}_q]$, and $[\overline{K}_{qq}]$ is premultiplied by the inverse of the modal mass matrix $[\overline{M}]^{-1}$ (the same notation is kept for convenience). Denoting

$$\begin{aligned}\{\dot{q}\}&=\{p\}\\ \{\dot{p}\}&=-([\overline{K}_L]+[\overline{K}_q]+[\overline{K}_{qq}])\{q\}\end{aligned} \tag{4.27}$$

the second order system of n Equations (4.26) is transformed into $2n$ equations of the first order in the state-space form of

$$\begin{Bmatrix} \dot{p} \\ \dot{q} \end{Bmatrix} = \begin{bmatrix} [I] & [0] \\ [0] & -\left([\overline{K}_L]+[\overline{K}_q]+[\overline{K}_{qq}]\right) \end{bmatrix} \begin{Bmatrix} p \\ q \end{Bmatrix} \tag{4.28}$$

Denoting $\{X\} = \begin{Bmatrix} q \\ \dot{q} \end{Bmatrix}$, we have to solve the following differential equation

$$\{\dot{X}\} = F(\{X\}) \tag{4.29}$$

with a judicious specification of initial conditions $\{X(0)\}$ that lead to periodic solutions.

The initial conditions are

$$\{X(0)\} = \begin{Bmatrix} q_1(0) \\ \vdots \\ q_n(0) \\ \dot{q}_1(0) \\ \vdots \\ \dot{q}_n(0) \end{Bmatrix} = \begin{Bmatrix} q_{01} \\ \vdots \\ q_{0n} \\ \dot{q}_{01} \\ \vdots \\ \dot{q}_{0n} \end{Bmatrix} = \begin{Bmatrix} \eta_1 \\ \vdots \\ \eta_n \\ \eta_{n+1} \\ \vdots \\ \eta_{2n} \end{Bmatrix} = \{\eta\} \tag{4.30}$$

For the periodic solution with period T it follows that

$$\{X(t+T)\} = \begin{Bmatrix} q_1(t+T) \\ \vdots \\ q_n(t+T) \\ \dot{q}_1(t+T) \\ \vdots \\ \dot{q}_n(t+T) \end{Bmatrix} = \begin{Bmatrix} q_1(t) \\ \vdots \\ q_n(t) \\ \dot{q}_1(t) \\ \vdots \\ \dot{q}_n(t) \end{Bmatrix} = \{X(t)\} \tag{4.31}$$

or setting $t = 0$

$$\{X(T)\} = \{X(0)\} \tag{4.32}$$

Recalling Equation (4.5) for t = 0 results in

$$\{W(0)\} = \sum_{r=1}^{n} q_{0r} \{\phi\}^{(r)} \tag{4.33}$$

Denote by T the period of the nonlinear system corresponding to the initial condition $\{\eta\}$ prescribed by Equation (4.30). It is assumed that

$$\begin{cases} T = T_0 + \Delta T \\ \{\eta\} = \{\eta_0\} + \{\Delta\eta\} \end{cases} \tag{4.34}$$

where T_0 and $\{\eta_0\}$ are initial approximations, and ΔT and $\{\Delta\eta\}$ are corrections that need to be computed. Initial conditions for the multimode approach are assumed to be

$$\{\eta_0\} = \begin{Bmatrix} q_{01} \\ 0 \\ \vdots \\ 0 \end{Bmatrix} \tag{4.35}$$

where

$$q_{01} = q_1(0) \tag{4.36}$$

is a given value. Now, using Equations (4.30), (4.32) and (4.34) one can write

$$\{X(T,\eta)\} = \{X(T_0 + \Delta T, \eta_0 + \Delta\eta)\} = \{X(0, \eta_0 + \Delta\eta)\} = \{\eta_0 + \Delta\eta\} \tag{4.37}$$

Employing a Taylor series in the neighborhood of (T_0, η_0) and neglecting the non-linear terms of the expansion yields

$$\{\eta_0\} + \{\Delta\eta\} \cong \{X(T_0,\eta_0)\} + \left.\frac{\partial\{X\}}{\partial t}\right|_{(T_0,\eta_0)} \Delta T + \left.\frac{\partial\{X\}}{\partial\{\eta\}}\right|_{(T_0,\eta_0)} \{\Delta\eta\} \tag{4.38}$$

Equation (4.38) can be rearranged into the form

$$\left(\left.\frac{\partial\{X\}}{\partial\{\eta\}}\right|_{(T_0,\eta_0)} - [I] \right) \{\Delta\eta\} + \left.\frac{\partial\{X\}}{\partial t}\right|_{(T_0,\eta_0)} \Delta T = \{\eta_0\} - \{X(T_0,\eta_0)\} \tag{4.39}$$

One needs to know $\{X(T_0,\eta_0)\}$, $\left.\frac{\partial\{X\}}{\partial t}\right|_{(T_0,\eta_0)}$ and $\left.\frac{\partial\{X\}}{\partial\{\eta\}}\right|_{(T_0,\eta_0)}$ in order to solve Equation (4.39). The vector $\{X(T_0,\eta_0)\}$ can be found by solving the system of Duffing equations using an initial guess (for the first iteration) or using the previous solution (for the

subsequent iterations) of the initial conditions. In order to estimate $\left.\frac{\partial\{X\}}{\partial t}\right|_{(T_0,\eta_0)}$ one can use Equations (4.29) and (4.30), noting that

$$\left.\frac{\partial\{X\}}{\partial t}\right|_{(T_0,\eta_0)} = F(\{X(T_0,\eta_0)\}) = F(\{X(0,\eta_0)\}) = F(\{\eta_0\}) \tag{4.40}$$

The Jakobian $\left.\frac{\partial\{X\}}{\partial\{\eta\}}\right|_{(T_0,\eta_0)}$ can be evaluated using the forward scheme

$$\left.\frac{\partial\{X\}}{\partial\{\eta\}}\right|_{(T_0,\eta_0)} = \left[\frac{\partial X_i}{\partial \eta_j}\right] \cong \frac{X_i(T_0,\{\eta_0\}+\varepsilon\{e\}_j)-X_i(T_0,\{\eta_0\})}{\varepsilon} \tag{4.41}$$

where ε is a small parameter, $\{e\}_j$ is the unit j^{th} vector and $i,j=1,2,...2n$. Denoting $[\Phi]=\frac{\partial\{X\}}{\partial\{\eta\}}$ Eq. (4.39) can be rewritten in the form

$$([\Phi]-[I])\{\Delta\eta\}+\Delta T\{F(\eta_0)\}=\{\eta_0\}-\{X(T_0,\eta_0)\} \tag{4.42}$$

Eq. (4.42) represents a system of *2n* equations. Since the amplitude of the first mode is prescribed arbitrary by Eq. (4.36) and is to remain constant during the iteration process, the number of unknowns is equal to the number of equations available. Replacing $\Delta\eta_{01}$ by ΔT, the 2n unknowns can be expressed as a vector

$$\begin{Bmatrix} \Delta T \\ \Delta\eta_{02} \\ \vdots \\ \Delta\eta_{02n} \end{Bmatrix}_{2nx1} = \begin{Bmatrix} \Delta T \\ \Delta\eta \end{Bmatrix}_{2nx1} \tag{4.43}$$

It follows that the system to be solved is

$$[\tilde{\Phi}]\begin{Bmatrix} \Delta T \\ \Delta\eta \end{Bmatrix} = \{\eta_0\}-\{X(T_0,\eta_0)\} \tag{4.44}$$

where

$$[\tilde{\Phi}]=\begin{bmatrix} \frac{\partial X_1}{\partial t} & \frac{\partial X_1}{\partial \eta_2} & \cdots & \frac{\partial X_1}{\partial \eta_{2n}} \\ \frac{\partial X_2}{\partial t} & \frac{\partial X_2}{\partial \eta_2} & \cdots & \frac{\partial X_2}{\partial \eta_{2n}} \\ \vdots & \vdots & \ddots & \vdots \\ \frac{\partial X_{2n}}{\partial t} & \frac{\partial X_{2n}}{\partial \eta_2} & \cdots & \frac{\partial X_{2n}}{\partial \eta_{2n}} \end{bmatrix} = \begin{bmatrix} F(\eta_{01}) & \frac{\partial X_1}{\partial \eta_2} & \cdots & \frac{\partial X_1}{\partial \eta_{2n}} \\ F(\eta_{02}) & \frac{\partial X_2}{\partial \eta_2} & \cdots & \frac{\partial X_2}{\partial \eta_{2n}} \\ \vdots & \vdots & \ddots & \vdots \\ F(\eta_{02n}) & \frac{\partial X_{2n}}{\partial \eta_2} & \cdots & \frac{\partial X_{2n}}{\partial \eta_{2n}} \end{bmatrix} \tag{4.45}$$

Finally,

$$\begin{Bmatrix} \Delta T \\ \Delta \eta \end{Bmatrix} = [\tilde{\Phi}]^{-1}(\{\eta_0\}-\{X(T_0,\eta_0)\}) \tag{4.46}$$

The process of determining the initial conditions for periodic motion is iterative. The updated period and the updated initial deflections become the initial conditions for the subsequent iteration. One needs specify a satisfactory rate of convergence where the iterative process is assumed to result in the desired accuracy. The choice of parameter ε has an affect on the accuracy of the results. In general, more iterations are needed when: the material is anisotropic, when the boundary conditions become more complicated, when the panel curvature increases, and/or when more modes are taken into account.

In order to investigate the stability of the scheme one needs to look at the eigenvalues of the Jakobian matrix.

The numerical scheme consists of the following steps:

- Prescribe initial displacement on the first mode
- Solve Eq. (4.40) using a 4th order Runge Kutta numerical integration scheme (RK4)
- Determine the Jakobian matrix, Eq. (4.41), using the Runge-Kutta 4th order integration scheme

- Construct the $[\tilde{\Phi}]$ matrix prescribed by Equation (4.45)
- Solve the algebraic Eq. (4.46) for $\begin{Bmatrix} \Delta T \\ \Delta \eta \end{Bmatrix}$
- Check the convergence, perform another iteration if convergence has not been satisfied.

The algorithm can be modified in order to obtain better accuracy while determining the Jacobian matrix, Eq. (4.41). The improvement of the accuracy by employing the centered scheme

$$\left.\frac{\partial\{X\}}{\partial\{\eta\}}\right|_{(T_0,\eta_0)} = \left[\frac{\partial X_i}{\partial \eta_j}\right] \cong \frac{X_i(T_0,\{\eta_0\}-\varepsilon\{e\}_j)-2X_i(T_0,\{\eta_0\})+X_i(T_0,\{\eta_0\}+\varepsilon\{e\}_j)}{2\varepsilon} \quad (4.47)$$

results in an increase of the computational cost of the iteration process.

4.6 Thermal Effects

In general, the change in the temperature from ambient or reference conditions will generate finite thermal deflection of the curved panel, which becomes the equilibrium position for the panel oscillation under acoustic pressure. Panel deflection depends upon both the average temperature increase and the temperature gradient across the thickness. For the special case of a flat isotropic or orthotropic panel with a uniform temperature distribution and inplane boundary conditions, the thermal buckling problem needs to be addressed. For a flat symmetrical structure, an initial uniform temperature increase will not generate any transverse displacement, although for immovable inplane boundary conditions the compression load will be increasing. At some point, known as the buckling temperature T_{cr}, the panel will encounter loss of stability resulting in the transverse deflection. Since the structure is flat and symmetrical one of two possible

equilibrium conditions will be reached. Figure 4.1 shows the buckling of a flat isotropic/orthotropic plate along with finite thermal deflection for the general case of a curved and/or antisymmetrically laminated panel. For an arbitrary curved panel or for the flat panel with non-symmetrical lamination, a finite thermal deflection is unique (does not exhibit two equilibrium positions).

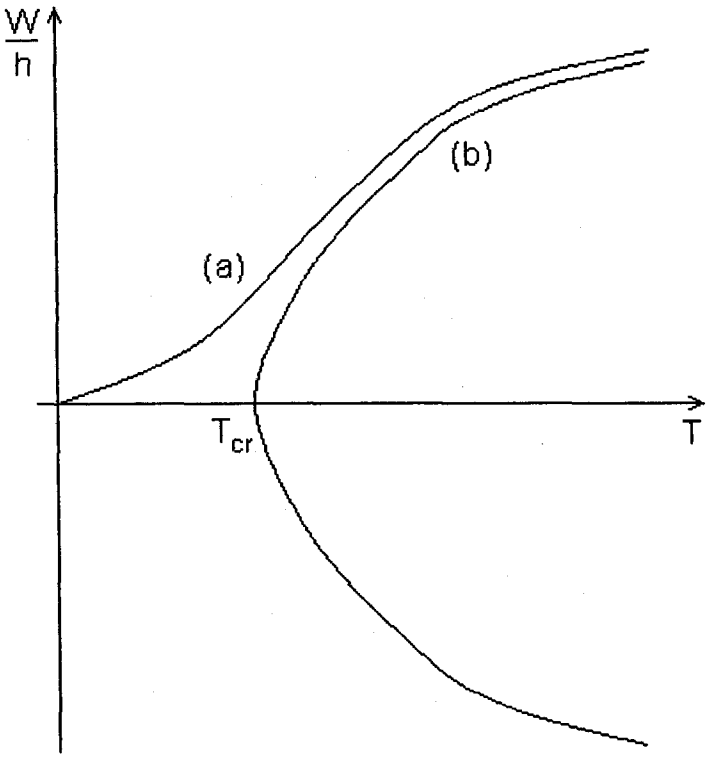

Figure 4.1 (a) Thermal Finite Deflection, and (b) Thermal Buckling

Solving the buckling problem for the flat isotropic or symmetrically laminated panel is beyond the scope of this work. For the detailed solutions the reader is referred to Chen and Mei[97] and Shi et al.[98,99] However, such a case will be used for validation of the thermal part of the formulation.

4.7 Random Pressure Fluctuation

4.7.1 White Random Pressure Simulation

In this work it is assumed that the pressure $p(t)$ varies randomly with time and is spatially distributed uniformly over the panel surface. The white noise is defined as stationary random sequence with the autocovariance in a form[94]

$$R(t)=\begin{cases}\sigma^2 & for\ t=0\\ 0 & for\ t\ an\ integer,\ t\neq 0\end{cases} \tag{4.48}$$

The white noise truncated at the cut-off frequency f_c, often referred as "pink noise" is defined as

$$G(f)=\begin{cases}G_0 & for\ 0\le f\le f_c\\ 0 & for\ f<0\ and\ f>f_c\end{cases} \tag{4.49}$$

The expression for G_0 can be written as[32]

$$G_0 = p_0^2\, 10^{\frac{SPL}{10}} \tag{4.50}$$

where p_0 is the reference pressure, $p_0 = 2.90075\cdot 10^{-9}\ psi\ (20\mu Pa)$, and SPL is the Sound Pressure Level expressed in decibels, *dB*. Integrating the "pink noise" over the bandwidth (equal to the value of the cut-off frequency) the Overall Sound Pressure Level (*OASPL*) can be found

$$\int_0^{f_c} p_0^2\, 10^{\frac{SPL}{10}}\, df = p_0^2\, 10^{\frac{SPL}{10}}\cdot f_c = p_0^2\, 10^{\frac{OASPL}{10}} \tag{4.51}$$

It follows that

$$OASPL = SPL + 10\log(f_c) \tag{4.52}$$

The length of the simulated process cannot be selected arbitrarily and needs to be related to the fundamental frequency of the structure. It has been shown in previous studies[32,35] that for a stationary response, reasonable statistical properties are obtained from a time history that contains more then 100 natural periods of the structure

$$N \cdot t > 100 \cdot \frac{1}{f_1} \tag{4.53}$$

where N is the number of simulated points, t is the time step, and f_1 is the fundamental frequency. The condition of Equation (4.53) is strictly fulfilled for all the curved panels studied in this work, and slightly relaxed for a flat panel, which has substantially lower fundamental frequency compared to curved panels. It is a common routine to employ Fast Fourier Transformation (*FFT*) while computing the Power Spectrum Density (*PSD*) of the signal. For that reason it is customary to select a value of N that can be represented by a power of two ($N = 2^n$).

The Matlab® code used to generate the white random pressure samples is shown in Appendix A.

4.7.2 Non-White Random Pressure Data (In-Flight Data)

The random pressure fluctuation with non-white characteristics have been obtained from in-flight recorded data provided by the Structural Dynamic Branch, Air Force Research Laboratory at Wright-Patterson Air Force Base. The microphone data were captured on a B-1B strategic bomber during take-off using full afterburner power. The recording consists of three parts captured at the three successive stages of take-off: (i) takeoff roll, (ii) rotation into flight, and (iii) initial flight when retracting the gear. One recording of approximately 14.8 seconds and sampling interval of 0.15294×10^{-3}

sec. (96756 measurement points) was used in this work. Figure 4.2 presents basic characteristics of the recorded data, including the time history, probability density function (PDF), and power spectral density (PSD) of the non-white pressure fluctuation, and its comparison with the simulated truncated white noise. It is seen that the PSD characteristics are non-flat and exhibit an incremental trend for the frequency range from 0 to about 180 Hz. For higher frequencies, the power density decreases. The highest rates of change correspond to the frequency interval below 400 Hz. There are also two pronounced spikes clearly noticeable on the PSD plots. One corresponds to a frequency of 180 Hz, the other occurs at 360 Hz.

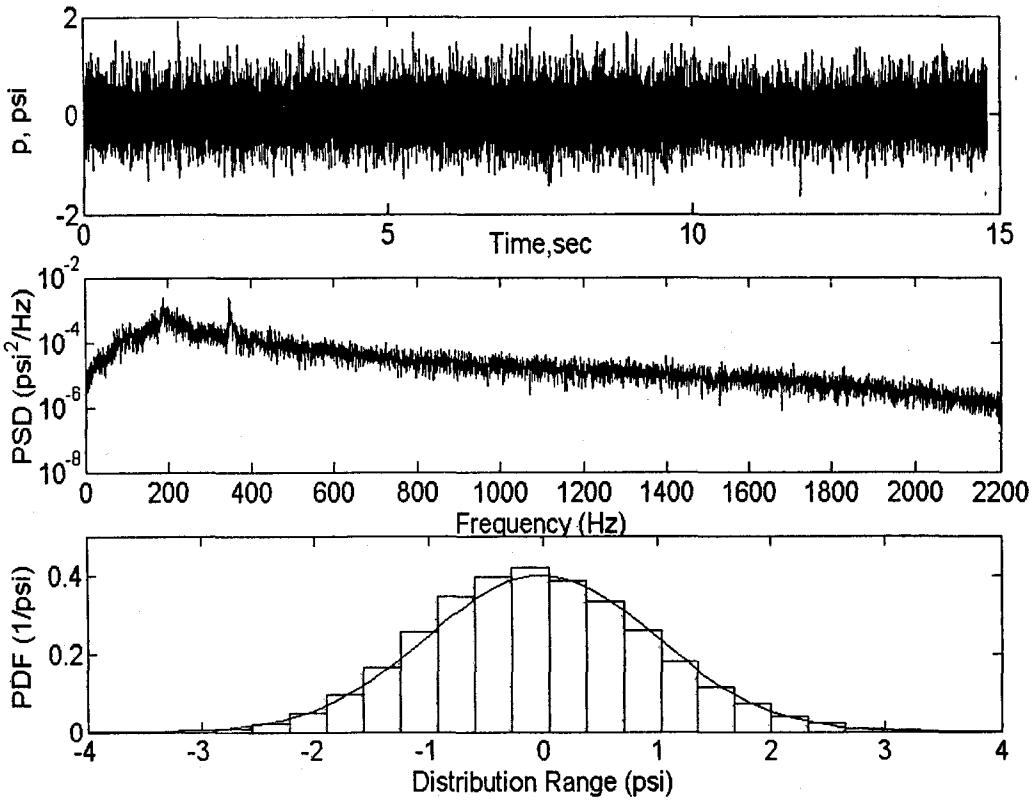

Figure 4.2a Time History, Probability Density Function (PDF), and Power Spectral Density (PSD) of Non-White Pressure Fluctuation (in-flight recorded data)

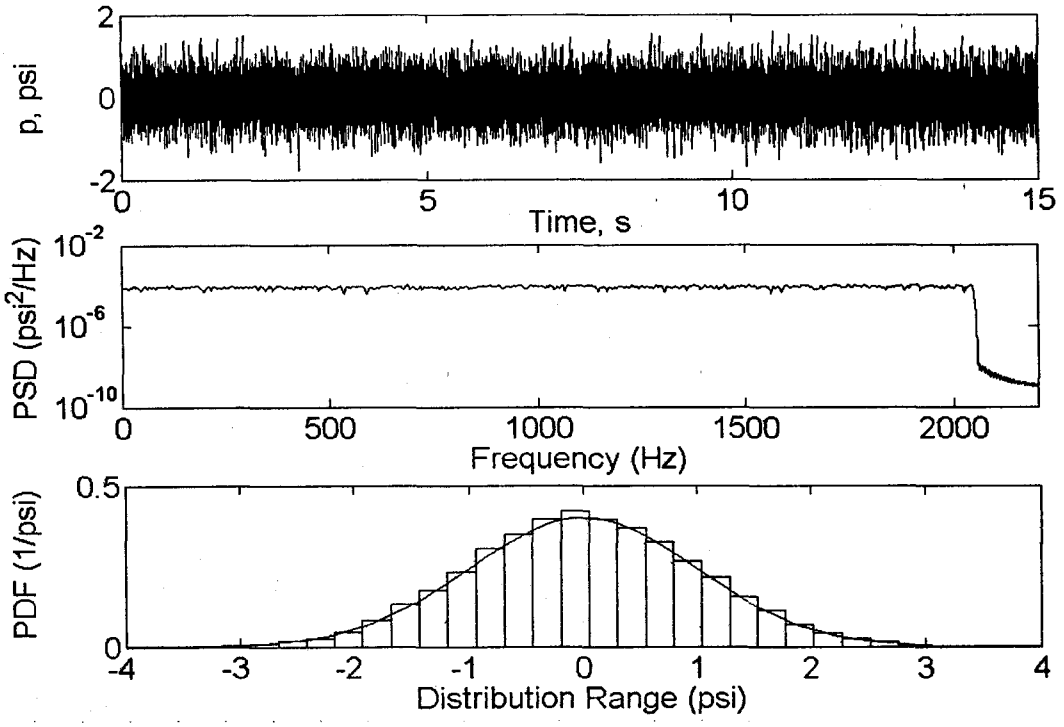

Figure 4.2b Time History, PDF and PSD of Simulated Truncated White Noise

No details regarding the microphone placement, its sensitivity, bandwidth, nor other apparatus parameters, were available. Also no data on measurement environmental conditions, i.e. temperature or humidity were available to the author. The statistics of recorded signal were calculated, and are presented in Table 3.1.

Table 3.1 Statistics of Microphone Recorded Random Pressure Fluctuation (measurement in units of psi)

RMS	0.365755
Mean	-0.017597
Variance	0.365331
Skewness	0.197474
Kurtosis	0.162631

4.7.3 Equivalent White Sound Pressure Level Simulation

In order to make comparisons of the panel response results for in-flight recorded data and for a comparable simulated white noise, the overall sound pressure level was chosen to be the same. In fact this means that the amount of energy carried by both power spectra are equal, however the frequency distribution of this energy is different. The overall sound pressure level for the B-1B recorded data was found to be 163.014 dB.

An important issue when simulating truncated white noise is the choice of cut-off frequency f_c. As mentioned before, when applying FFT it is customary to make the count equal to some power of 2. At the same time, the cut-off frequency must be high enough to excite a certain number of the desired lowest modes. With respect to this requirement, the Nyquist criterion applies.[35,36] It states that the excitation frequency should be at least double of the natural frequency to be excited. Since some preliminary studies indicated that a 6-mode solution represents a reasonable compromise between the accuracy and the computational effort, and for all shallow shells under investigation, the natural frequency

of the 6th mode did not exceed 1024 Hz, the cut-off frequency was set to 2048 Hz. Applying Eq. (4.52), the SPL of truncated white noise was found to be 129.901 dB.

4.8 Monte Carlo Simulation

Monte Carlo methods enable the simulation of any process influenced by random factors. However it needs to be recognized that for many mathematical problems involving no chance, one can artificially devise a probabilistic model for solving these problems. For these reasons the Monte Carlo method can be considered a universal method for solving a variety of complex mathematical problems.

Two distinctive features of the Monte Carlo method can be summarized as follows: One advantageous feature of the method is its simple structure for the computation algorithm. As a rule, a program is written to carry out one random trial. This trial is repeated N times, each trial being independent of the other trials, and then the results of all trials are averaged. Therefore, the Monte Carlo method is sometimes called the method of statistical trials. A second feature of the method is that the error of calculations is proportional to

$$error = \sqrt{\frac{D}{N}} \tag{4.54}$$

where D is some constant, and N is number of trials. Hence, it is clear that to decrease the error by one order of magnitude, it is necessary to increase number of trials by two orders of magnitude. Therefore the major drawback of this approach is the computational cost.

For the random vibration problem the approach essentially consists of generating a large number of sample excitations (code listed in Appendix A with different values of

seeds - variable *ISEED*), calculating the corresponding response samples (by the FE modal approach), and processing the desired response characteristics (Section 3.2). Based on previous experience,[35,36] but also keeping in mind that the scope of this work is to establish a methodology rather than obtain great accuracy for the particular study cases the number of samples adopted in this work is 7. Before calculating the desired characteristics it is important to recognize that they should be based on the "developed" part of response. However, before the response is fully developed, a shallow shell panel that is initially at rest undergoes induced transient oscillations. Therefore to ensure that accurate response statistics are obtained, the transient part of a response needs to be removed. In this work each random pressure sample is generated for 2.0 sec, than the response is calculated for 1.2 sec only, and the first 0.2 sec is removed (in Chapter 5 time intervals from 0 to 1.0 sec are plotted to demonstrate the presence of an initial transient response phase.)

4.9 Time Step Considerations

Runge-Kutta 4th order integration scheme is employed to solve the system of nonlinear differential equations of motion. The scheme is explicit, so the step by step approximation of q_{k+1} (corresponding to time t_{k+1}) is obtained from q_k (corresponding to t_k) in such a way that the power series expansion of the approximation coincides with the actual Taylor series development of $q(t_k + h)$ up to terms of 4th order. Therefore

$$q_{k+1} = q_k + \frac{1}{6} h(b_1 + 2b_2 + 2b_3 + b_4) \tag{4.55}$$

with

$$
\begin{aligned}
k_1 &= f(t_k, q_k) \\
k_2 &= f\left(t_k + \frac{1}{2}h, q_k + \frac{1}{2}hb_1\right) \\
k_3 &= f\left(t_k + \frac{1}{2}h, q_k + \frac{1}{2}hb_2\right) \\
k_3 &= f(t_k + h, q_k + hb_3)
\end{aligned}
\tag{4.56}
$$

where $h = t_{k+1} - t_k$. The scheme is conditionally stable. The necessary condition to be fulfilled is a Nyquist criterion introduced with regard to the cut-off frequency selection in Section 4.7.3. A satisfactory criterion was obtained in such a way that time step prescribed initially based on Nyquist rule was halved until two consecutive solutions resulted in the same response.

4.10 Post-Processing of the Displacement Solution – Strain and Stress Calculation

Fatigue life models are usually based on strain (composites), or stress (isotropic materials) time histories. In this section the finite element displacement solutions are post-processed in order to obtain these values.

After the modal displacement $\{q\}$ for a given combination of acoustic load and elevated temperature is determined, $\{W_b\}$, $\{\psi\}$ and $\{W_m\}$ can be evaluated with Eq. (4.5) for the general case or with Eq. (4.23) and Eq. (4.16) for the special case described in section 4.2.2. The element inplane strain $\{\varepsilon^0\}$, curvature $\{\kappa\}$ and shear strain $\{\gamma\}$ can be calculated using Eqs. (2.28), (2.29), and (2.30), respectively.

In the displacement based FE model, the assumed displacement functions act as constraints on the system, therefore resulting in overly stiff behavior. Barlow[100] and Cook et al.[101] addressed this issue and demonstrated that application of a lower-order

quadrature rule improves the accuracy of the strain and stress estimations. This so-called "reduced integration" tends to soften an element, thus countering the overly stiff behavior associated with the displacement method. The softening is a result of vanishing higher order polynomials at integration points (Gaussian quadrature) of a lower-order rule. As a consequence, these terms do not contribute to the element strain energy. Based on this argument, the strains and stresses are computed at *N-1* Gauss points of an element, where *N* is the Gauss quadrature needed in order to obtain an exact integration.

Because this FE formulation is displacement-based, the strains and stresses are not continuous between elements with the C^0-class element model (C^0 has continuous displacement only in contrast to C^1 that has continuous displacement and slope). To improve the accuracy of the strain results the average is taken from different local nodal values that share the same global node number. Then, the transformation into the material principal coordinates is performed for the k^{th} layer of a laminated panel

$$\begin{Bmatrix} \varepsilon_1 \\ \varepsilon_2 \\ \gamma_{12} \end{Bmatrix}_k = [T_\varepsilon(\theta)] \begin{Bmatrix} \varepsilon_x \\ \varepsilon_y \\ \gamma_{xy} \end{Bmatrix}_k \tag{4.55}$$

where the transformation matrix is given by Eq. (2.41). If required (for isotropic materials) stress is obtained by usual constitutive law.

4.11 Fatigue Life Estimation

In this section the description of the numerical procedures implemented in the WAVE Analysis Toolbox[102] and developed in the Matlab® environment are given. The procedures follow closely the formulation presented in Sections 3.3 and 3.4. Source code is presented in Appendix B.

4.11.1 Turning Points

Command *[TP ind]=dat2tp(x,h,wdef)* finds the turning points from data. Input x is a two column data fill with a time-sampled value format, h is a threshold, and *wdef* defines the type of wave. *TP* and *ind* are the outputs and refer to the turning point of the two column vector of a structure similar to x, and the indices of the turning points, respectively. The process of finding *TP* is shown in Figure 4.3, and needs to be performed before attempting the Rainflow Counting analysis.

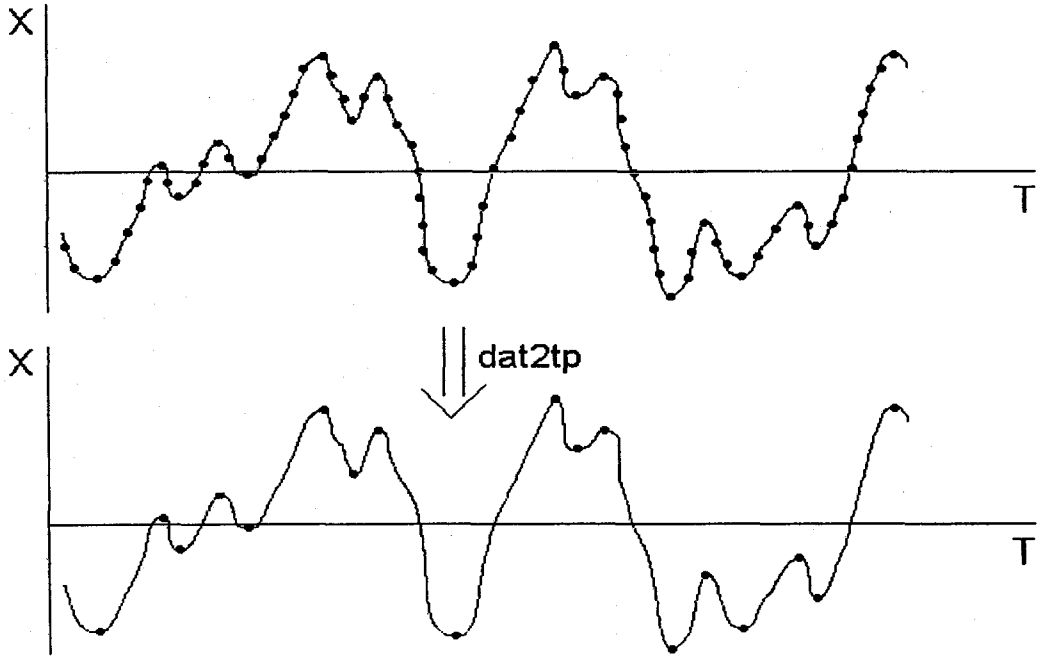

Figure 4.3 Data to Turning Points (TP)

4.11.2 Crossing Rate

Command *lc=tp2lc(TP,def,plotflag,sa)* calculates the number of up-crossing from the turning points *TP*. The additional inputs *def*, *plotflag*, and *sa* define whether to include also minima and maxima, plotting options, and standard variation of the process, respectively. Knowledge of up-crossing rate of certain level of strains permits determination whether the process is narrow- or broad-band, and whether or not it corresponds with Gaussian distribution. A sample of up-crossing rate of strain is shown in Figure 4.4.

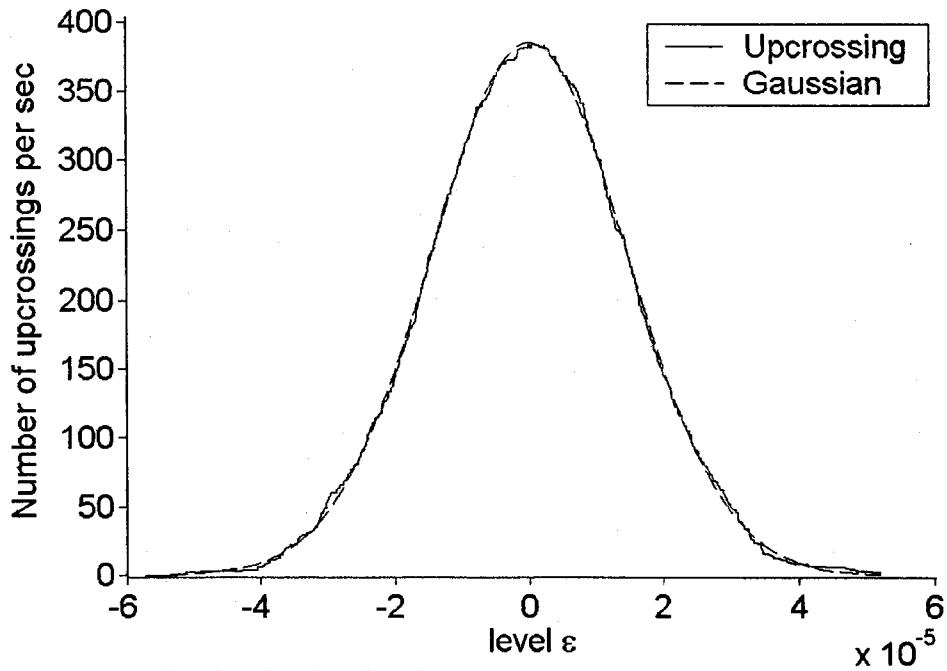

Figure 4.4 Up-crossing Rate

4.11.3 Rainflow Cycles

Command *[rfc,rfc1,res]=tp2rfc(TP,def,rfc0,res0)* finds the rainflow cycles from the sequence of turning points *TP*. Input *def* allows the selection of min-to-max cycles (correct number of up-crossing), max-to-min cycles (correct number of down-crossing), and the Cloormann-Seeger method (correct number of closed hysteresis loops). *rfc0* and *res0* additionally allow for the computation of rainflow cycles without residuals and the residuals themselves – these values are assigned to the outputs *rfc1* and *res1*, respectively. The procedure is the realization of the algorithm outlined in Section 3.3.1. The central idea of RFC is shown in Figure 3.6.

4.11.4 Peak Through Valley Cycles

Command *[mM,Mm]=tp2mm(TP)* finds the min-to-max (*mM*) and max-to-min (*Mm*) cycles from the sequence of turning points *TP*. *mM* and *Mm* are in two column format of time-value. These peaks are calculated only for the comparison to demonstrate the difference between the simplest available method and RFC. The sample comparison is shown in Figure 4.5 and suggests that PTVC will result in more conservative fatigue estimation compared with RFC.

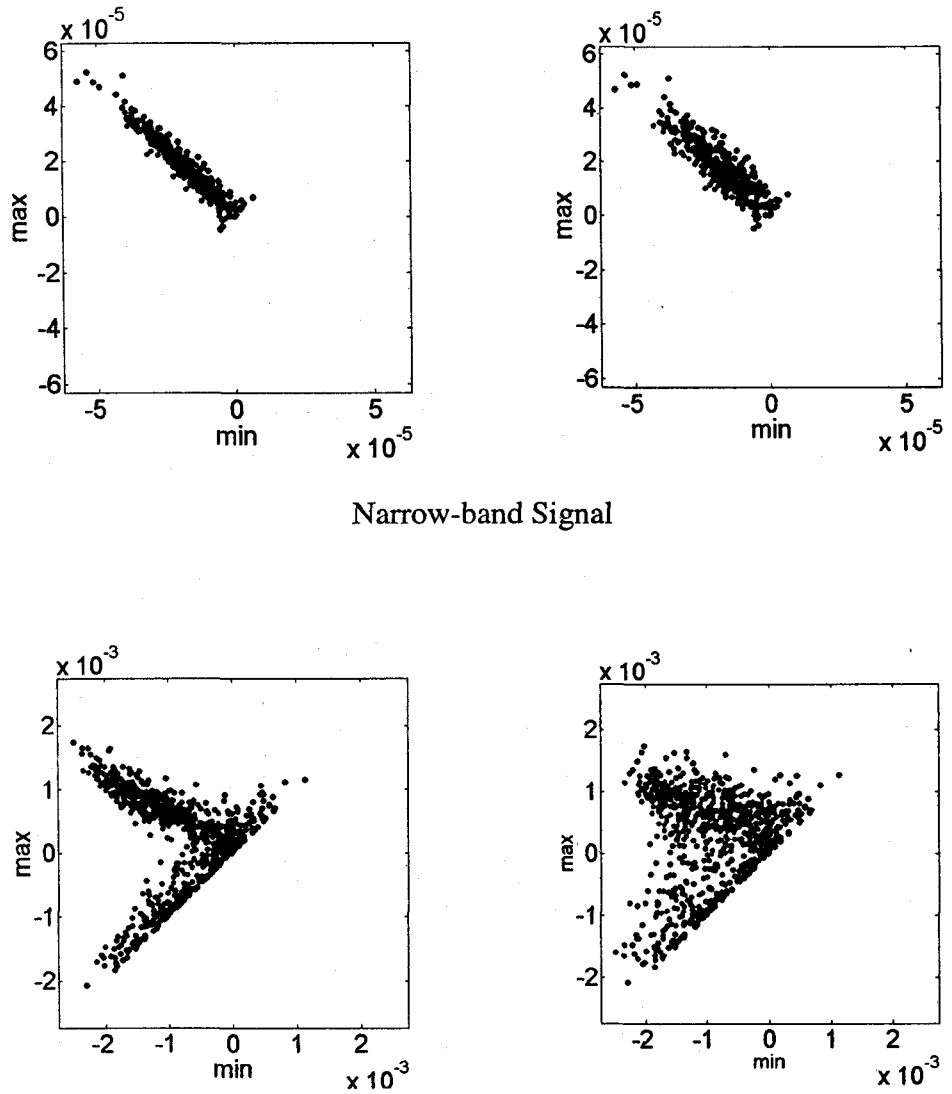

Figure 4.5 Comparison of strain counting by RFC vs. PTVC for Narrow-band and Broad-band Signals

4.11.5 Damage and Operational Life

Command *D=cc2dam(cc,beta,K)* calculates the damage, *D*, of a cycle count according to Palmgren-Miner theory (Equation 1.3). *cc* is a cycle count in two column format of min-max, and *beta* and *K* are material properties (see Equation 1.1). Consequently, the operational life is computed from Equation (1.6).

5. Results and Discussion

5.1 Validation

Since no work has been reported on multimode nonlinear random vibration of shallow shells exposed to combined acoustic and thermal loads, the validation process will be conducted by parts. First, the FE formulation is validated for the case of nonlinear free vibrations against classic solution by Leissa and Kobayashi,[10] which utilizes First Order Shear Deformation Theory. Subsequently, the forced vibration response prediction methodology is validated against known solutions for a flat panel configuration with random pressure excitation input.[103-105] Also, buckling and postbuckling behavior are compared with the analytical solution by Paul[106] to validate thermomechanical portion of the formulation.

5.1.1 Free Vibration Problem – Nonlinear Stiffness Validation

It is known that curved panels exhibit soft-spring behavior at large deflections unlike, hard-spring behavior for flat plates. No work has been reported so far for large amplitude free vibration of shallow shells considering effects of inplane inertia, and characterizing the dynamic behavior with coupled linear bending-inplane modes and multiple-mode solutions. The analytical methods, as described in Section 1.1 have mathematical difficulties in obtaining closed form solutions unless the inplane inertia is neglected in the formulation. Therefore, for the sake of comparison, the validation of the developed free vibration FE formulation is also conducted under the restriction of neglecting the inplane inertia and characterizing the nonlinear vibration behavior with linear bending modes only. The FE formulation without inplane inertia is presented in Section 4.2.2, so that the finite element vibration results could be compared with classical

analytical results. First, the single-mode solutions for isotropic shells supported by shear diaphragms ($v = 0$, $w = 0$, $\psi_y = 0$ at $x = 0$ and $x = a$, and $u = 0$, $w = 0$, $\psi_x = 0$ at $y = 0$ and $y = b$) were compared with results obtained by Kobayashi and Leissa.[10] For all cases studied in this section, symmetrical initial conditions were assumed. Consequently the response consists only of symmetrical modes, allowing one quarter of the shallow shell to be studied for refined discretization. The mesh size used was 14 by 14 or 392 triangular shallow shell elements. For shear diaphragm boundary condition this results in 980 structural node DOF. The dimensions of the shallow shell used for validation are $a = b =$ 3.937 in. (0.10 m), nondimensional radii are defined as $r_x = R_x/a$ and $r_y = R_y/b$, and nondimensional thickness is $H = h/a$. The idea behind retaining only the symmetrical modes in the formulation was for future random vibration studies, where random pressure fluctuations would be assumed to be uniform over the panel surface and only the symmetrical modes are excited. Similarly, the only gradient for the temperature distribution that is allowed in the formulation is the one across the thickness, therefore the thermal environment is not contributing any unsymmetrical deflection components.

Since the cubic nonlinearity is well established and investigated based on flat isotropic or orthotropic composites plate studies, the particular attention is now turned to the quadratic nonlinearity. The quadratic nonlinear term, responsible for introducing the softening characteristics into the dynamic response can originate from two factors. One is geometrical – namely, the curvature of the panel; the second is due to the material stacking sequences, and its existence is noticeable for unsymmetrical lamination of composites.

Figures 5.1 to 5.3 present a comparison between the present formulation and the classical results by Kobayashi and Leissa obtained via PDE/Galerkin method.[10] In both finite element and classical formulations first order shear deformation theory is used, and inplane inertia neglected. Therefore FE modal equation that is being solved is Eq.(4.25) obtained under assumption expressed by Eq.(4.15). Presented results are single mode. The fundamental frequency ratios ω_{NL}/ω_L as a functions of the nondimensional maximum deflection W_{max}/h for various shallow shell geometries (doubly curved, cylindrical, saddle), radii and thicknesses are investigated. It is seen from Figure 5.1 that doubly curved panels ($r_x/r_y>0$) exhibit more softening in comparison with cylindrical panels ($r_x/r_y=0$). Saddle panels ($r_x/r_y<0$) do not exhibit softening characteristics. Good agreement between the present FE and classical results is found.

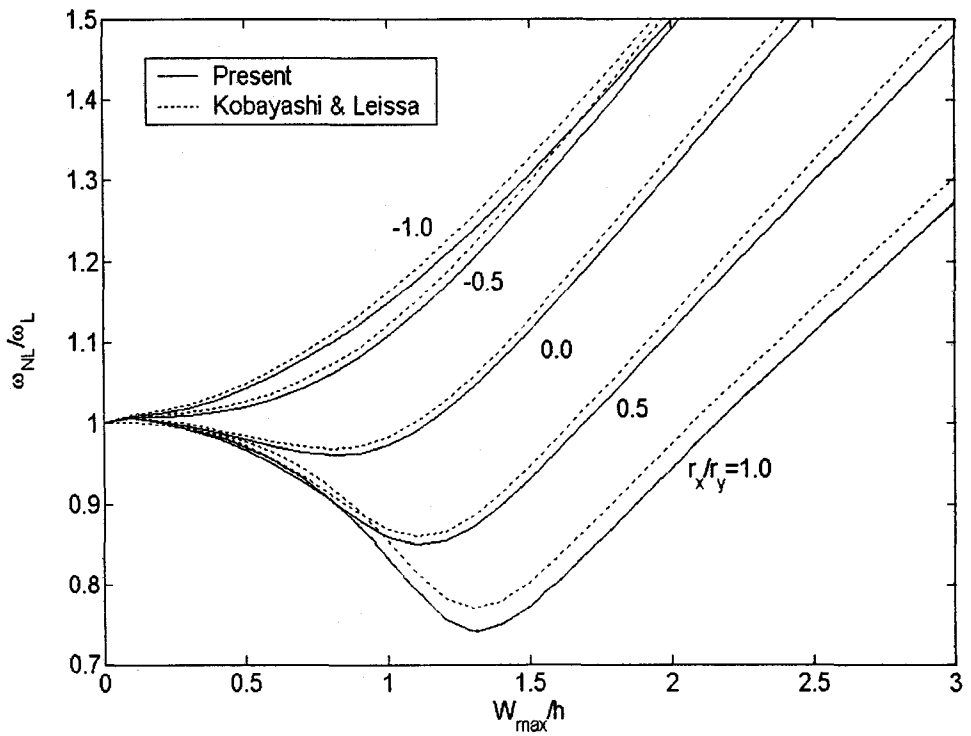

Figure 5.1 Comparison of Analytical and FE Fundamental Frequency Ratio for Various Curvature Ratios $r_x = 10$, $h/a = 0.01$, $b/a = 1$, $\nu = 0.3$

The agreement is also good to excellent for a wide range of radii of curved panels. Based on Figure 5.2 it is seen that even for relatively small ratio of shell curvature to its corresponding panel length $r_x = R_x/a$ and $r_y = R_y/b$ equal to 10, the agreement is quite acceptable.

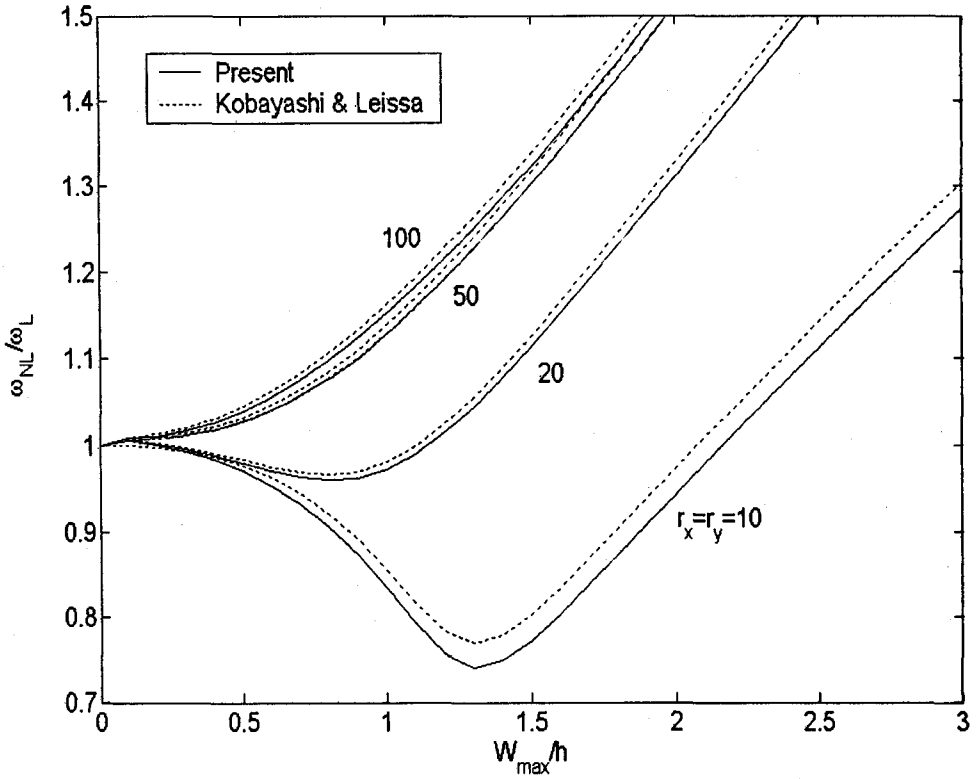

Figure 5.2 Comparison of Analytical and FE Fundamental Frequency Ratio for Various Curvatures h/a = 0.01, b/a = 1, ν = 0.3

First order shear deformation theory, incorporated in the formulation, allows the analysis of panels over relatively wide range of thicknesses. It is seen in Figure 5.3 that the agreement is very good for the range of thicknesses in terms of the edge of the panel

ratio $H=h/a$ up to 0.2. It is also observed that thinner shells will have more pronounced softening characteristics than thicker ones.

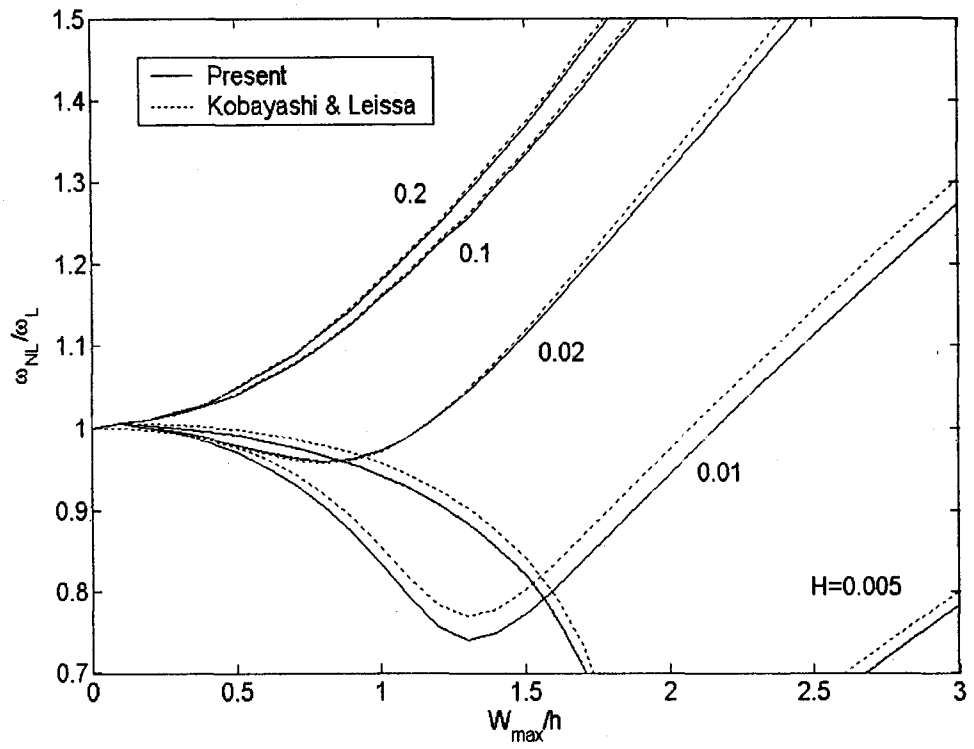

Figure 5.3 Comparison of Analytical and FE Fundamental Frequency Ratio for Various Thickness Ratios, H=h/a, $r_x = r_y = 10$, b/a=1, $\nu = 0.3$

Secondly, for a flat, simply supported $(0/90)_3$ cross-ply plate, the coefficients of the nonlinear terms of the single-mode Duffing equation were compared in Table 5.1 with those obtained by Pillai and Rao.[14]

Table 5.1 Duffing Equation Coefficients for a Flat Simply Supported Cross-ply $(0/90)_3$ Rectangular Plate

$\ddot{q}+\omega^2\left(q+\alpha q^2+\beta q^3\right)=0$	α	β
PDE/Galerkin[14]	0.8896	5.9153
FE (14x14) quarter plate	0.8759	5.8965
Difference, %	-1.54	-0.32

Dimensions: a=20 mm, b=10 mm, h=0.6 mm
Material Properties: E_{11} = 5000 kg/mm^2, E_{22} = 500 kg/mm^2, ν_{12} = 0.25, G_{12} = 250 kg/mm^2

Again, good agreement was found. Therefore both factors -- namely the curvature of the panel (Figures 5.1-3) and the non-symmetrical lamination sequence (Table 5.1) -- contributing to the quadratic term in the Duffing equation were investigated.

In order to predict the random response, some shallow shell configurations to be analyzed under random and/or thermal loads have also been analysed and will be discussed later. Since shear diaphragm supports are very rare in an aerospace design, all the subsequent cases in this work will be dealing with either simply supported (u = 0, w = 0, ψ_y = 0 at x = 0 and x = a) or clamped boundary conditions (v = 0, w = 0, ψ_x = 0 at y = 0 and y = b).

5.1.2 Forced Response Validation

5.1.2.1 Random Response

In order to verify the accuracy of the forced response prediction, random response of an isotropic flat plate was computed and compared with several other results obtained

using the Fokker-Planck-Kolmogorov equation,[103] a finite element with Equivalent Linearization formulation,[104] and another finite element modal approach utilizing BFS elements and Classical Plate Theory.[105] The study was conducted on a simply supported 12 x 15 x 0.040 in. (304.8 x 381.0 x 1.016 mm) aluminium panel. The mesh size used for quarter panel was 10 by 10 or 200 triangular elements. The material properties are E = 10.587 psi (73.0 MPa,) ν = 0.3, and $\rho = 2.588 \times 10^{-4}$ lbf-sec^2/in.^{4} (2763 kg/m^2). The comparison is presented in Table 5.2. Good agreement is found in comparison with the FE/BFS formulation,[105] and satisfactory agreement for the remaining two references. However, one needs to bear in mind that the FPK solution is available for a single mode, and inaccuracy of the EL approach was demonstrated in Figure 1.4.[65]

Table 5.2 Comparison of RMS (W_{max}/h) for a Simply Supported 12x15x0.040 in. Isotropic Aluminum Plate

SPL, dB	FPK[103] 1 mode	FE/EL[104] 4 modes	FE/BFS[105] 4 modes	Present 4 modes
90	0.249	0.238	0.266	0.254
100	0.592	0.533	0.489	0.510
110	1.187	1.031	1.092	1.069
120	2.200	1.905	2.113	2.100

5.1.2.2 Thermal Loads – Buckling Temperature and Postbuckling Behavior

The thermal buckling problem and post-buckling behavior were used to validate the thermal part of the formulation. A comparison with an analytical solution of 25 terms by Paul[106] was performed. A clamped isotropic plate of 10 x 10 x 0.040 in. (254 x 254 x 1.016 mm) was used in the study with material properties of E = 10.587 Msi (73.0 GPa), $\nu = 0.3$ and $\alpha = 12.5 \times 10^{-6}$ 1/°F (27.8×10^{-6} 1/°C). The mesh size used for the quarter panel was 10 by 10 or 200 triangular elements. The nondimentional critical buckling temperature

$$T_{non\,\dim} = 12(1+\nu)\frac{\alpha \Delta T a^2}{\pi^2 h^2} \tag{5.1}$$

and large postbuckling deflections were compared. A critical buckling temperature of T_{cr} = 5.304 was found, which matches exactly with the solution by Paul.[106] Also, excellent agreement of the postbuckling behavior is presented in Figure 5.4.

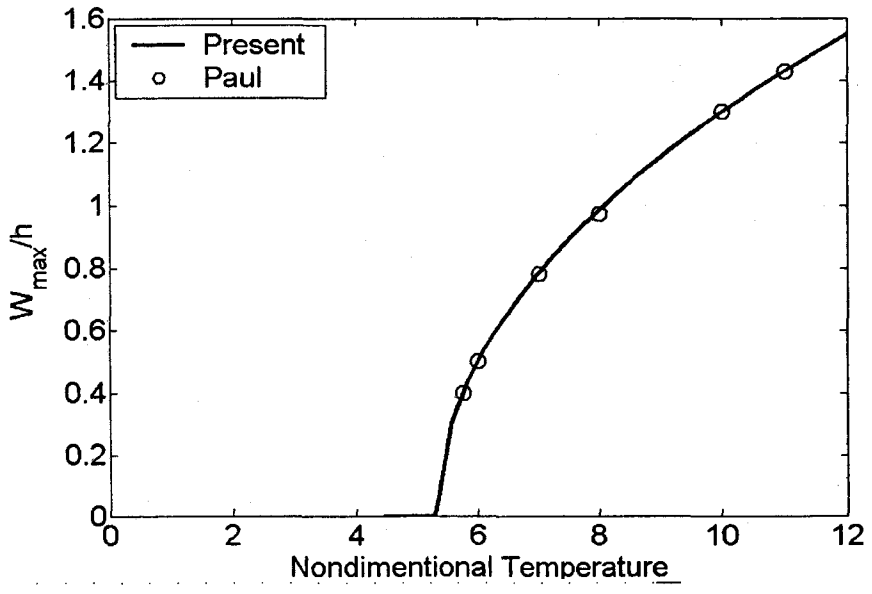

Figure 5.4 Critical Buckling Temperature and Post-buckling Behavior of 10 x 10 x 0.040 in. Clamped Aluminum Plate

5.1.3 Strain and Stress Validation

The accuracy of the stress calculations was verified by comparing values of RMS (σ_{max}) with the results obtained by Dhainaut.[36] The accurate results obtained for stress implies that prior calculated strains are also accurate. Table 5.3 compares values of RMS (σ_{max}) obtained for a 12 x 15 x 0.060 in. (308.4 x 381 x 1.524 mm) simply supported isotropic plate with material properties listed in Section 5.1.2.1, and a mesh size of 10 by 10 or 200 triangular elements for the quarter panel. Both sets of results presented in Table 5.3 were obtained by an FE method with 6 modes retained in the solution; it should be noted that Dhainaut[36] used rectangular C^1-class elements with Classical Plate Theory (Kirchoff Plate Theory), and the present work utilizes triangular C^0-class elements with First Order Shear Deformation Theory. Bearing this in mind, the comparison is considered to be very good.

Table 5.3 Comparison of RMS (σ_{max}) psi for a Simply Supported 12x15x0.060 in. Isotropic Plate at White Noise Excitation with Cut-off Frequency of f_c = 1024 Hz

SPL, dB	FE/BFS[36]	Present
83.75	47.01	46.27
113.84	1209.5	1161.9
119.87	2575.8	2491.9
131.91	5858.5	5781.3

5.2 Results

5.2.1 Free Vibration

For all cases studied in this section, symmetrical conditions were employed. Consequently the response consists only of symmetrical modes, allowing one quarter of the shallow shell to be studied for refined discretization. The mesh size used was 14 by 14 or 392 triangular shallow shell elements, which results in 980 structural node DOF for edges supported by shear diaphragms, and in 978 structural node DOF for simply supported boundary conditions.

First, the square isotropic doubly curved shallow shell used in the FE model validation (Section 5.1.1,) $r_x = r_y = 10$, $b/a = 1$, $H = 0.01$, $\nu = 0.3$, was studied to investigate the effect of inplane inertia (neglected/not-neglected) and the discrepancy between single- and multi-mode solutions. Subsequently, several graphite-epoxy simply supported cylindrical panels were studied to determine the influence of the stacking sequence of the laminations on the response.

5.2.1.1 Inplane Inertia Effect

Analytical methods have expressed the shallow shell response in terms of linear bending modes only by neglecting inplane inertia effects as described earlier. The FE formulations presented here are capable of providing solutions to Eq. (4.14) and to Eq. (4.25). It is found, as presented in Figure 5.5, that the vibrating shallow shell exhibits hard response characteristics when the solution is obtained by utilizing coupled bending-inplane modes with inplane inertia effects, and softening response characteristic when bending modes only are used and inplane effects are neglected. In an attempt to resolve

this ambiguity two steps were undertaken, namely: (1) multimode solutions for both FE modal formulations are computed, and (2) the solution in structural DOF as presented by Eq. (2.166) is calculated. A finite element formulation where inplane inertia was neglected was presented in Section 4.2.2.

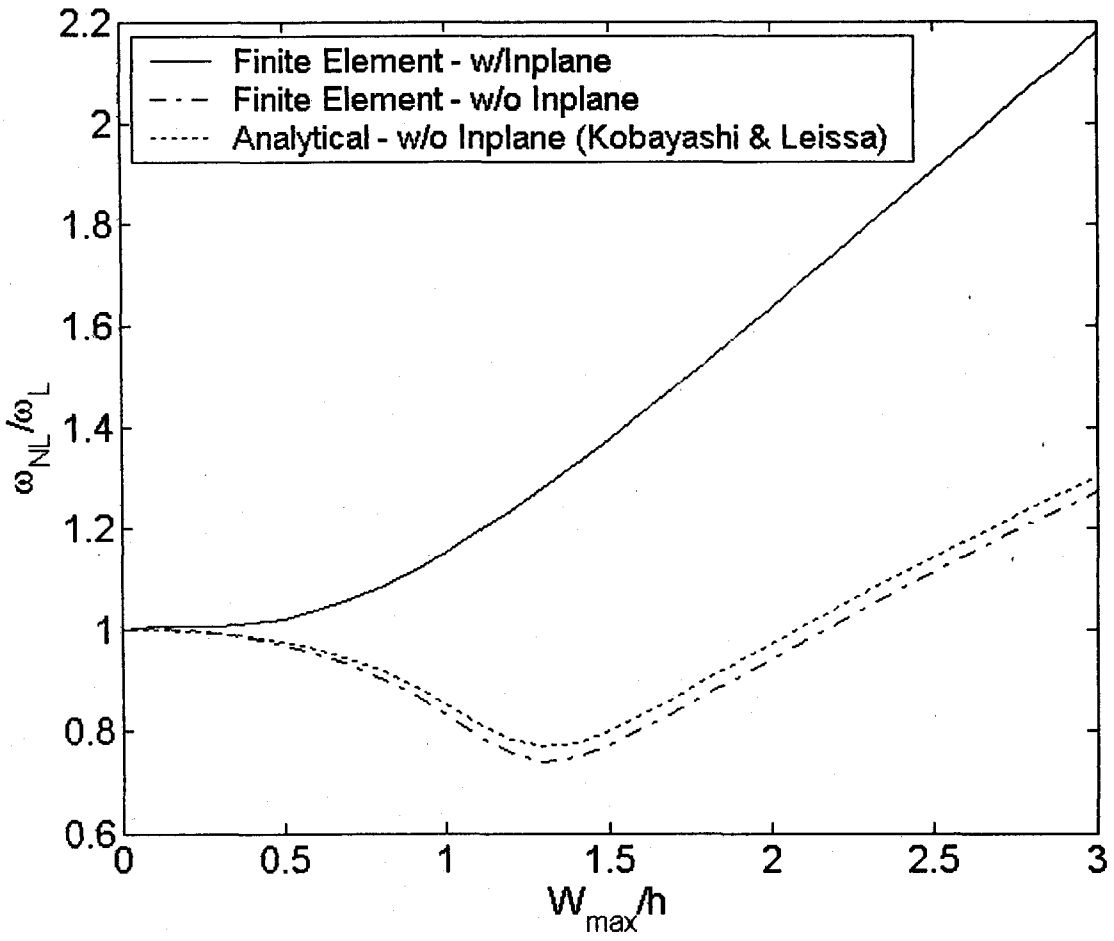

Figure 5.5 Effect of Inplane Inertia on the Square Isotropic Doubly Curved Shell Response, $\nu = 0.3$, $r_x = r_y = 10$, $H = 0.01$

5.2.1.2 Multimode Solution

The two-mode and three-mode solutions were determined and compared with the single-mode solution using both of the FE modal formulations considered. Once the 3-mode solution is available, also a solution in structural DOF (due to computational limitations a quarter section of shallow shell was discretized with 4 by 4, or 32 triangular elements) with initial conditions obtained from the shell deflection of the three-mode solution was determined. The first three natural frequencies are given in Table 5.4.

Table 5.4 Natural Frequencies for Isotropic Square Doubly Curved Shallow Shell Supported by Shear Diaphragms

Mode	(1,1)	(1,3)+(3,1) (1,3)-(3,1)	(3,3)
Frequency, Hz	944.46	2550.6	4427.6
Dimensions:	$a = b = 0.10$ m, $h = 1$ mm, $R_x = R_y = 1.0$ m		

Sample time response, and phase plots for moderately large amplitude vibrations are presented in Figure 5.6 and Figure 5.7, respectively, for the formulation in bending modes only. It is seen in Figure 5.6 that the FE structural DOF solution (obtained with 4x4 mesh discretization) agreed very well with the three-mode modal solution in bending modes only.

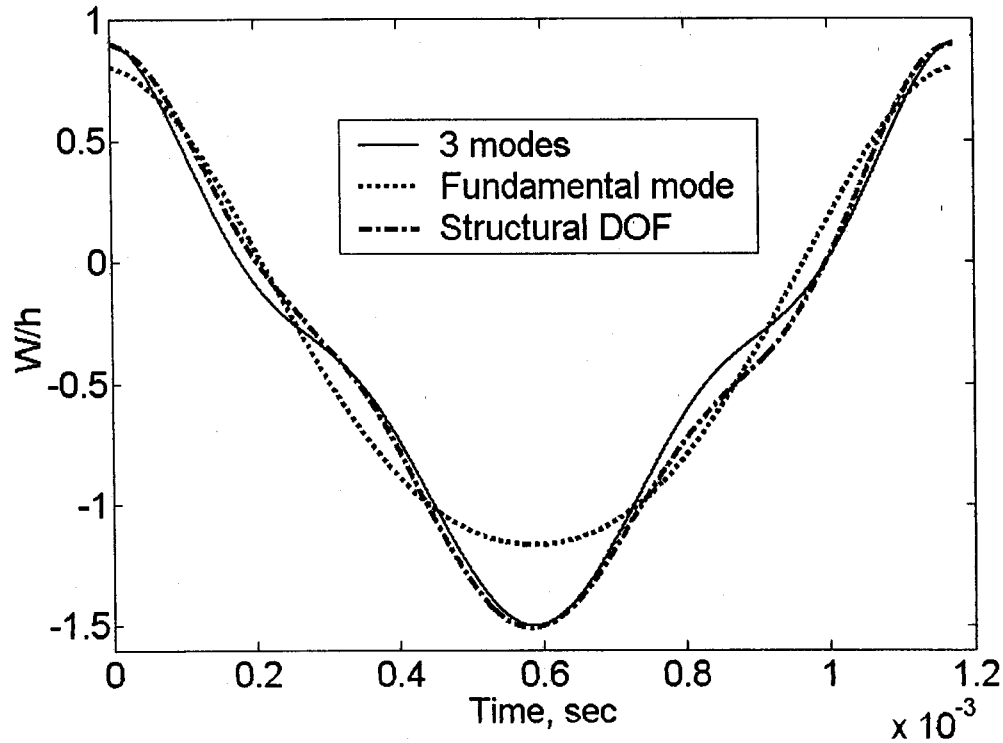

Figure 5.6 Time Response of an Isotropic Doubly Curved Shallow Shell

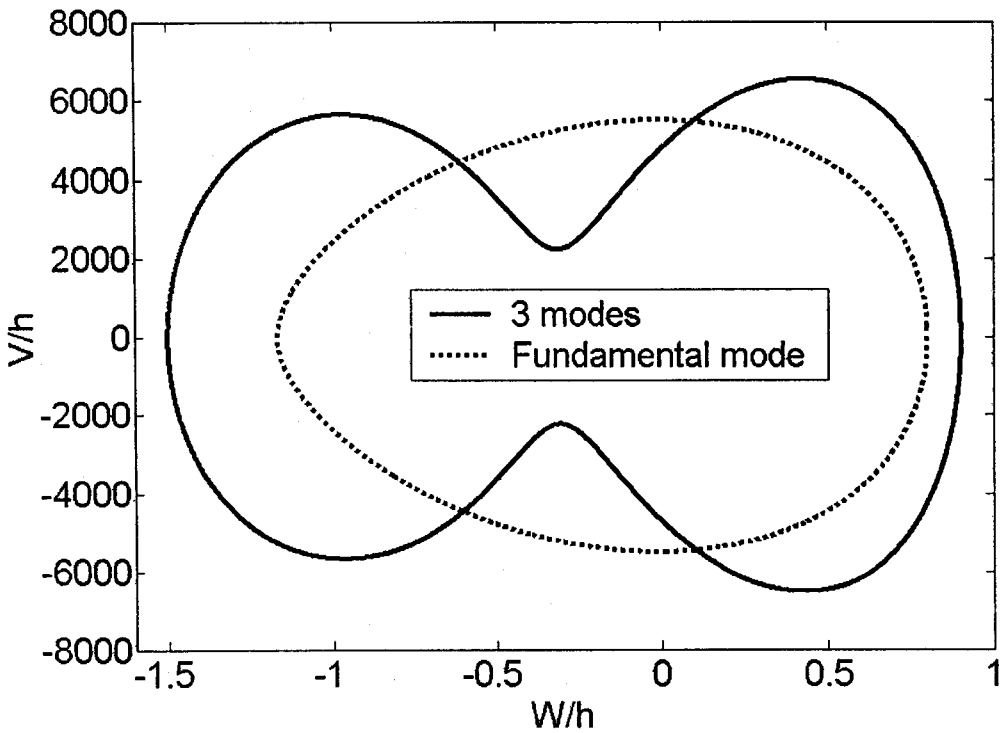

Figure 5.7 Phase Plot for an Isotropic Doubly Curved Shallow Shell

For the same formulation a typical set of the three-mode results consisting of the time response and the phase plots for each mode is presented in Figure 5.8a and 5.8b, respectively.

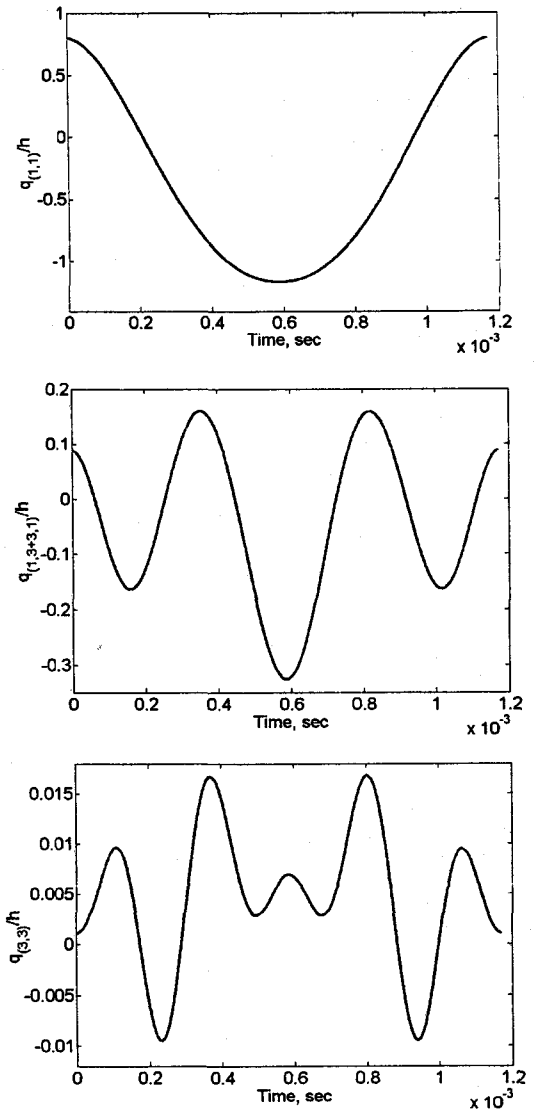

Figure 5.8a 3-mode Solution - Time Response for Modes (1,1), (1,3)+(3,1), and (3,3).

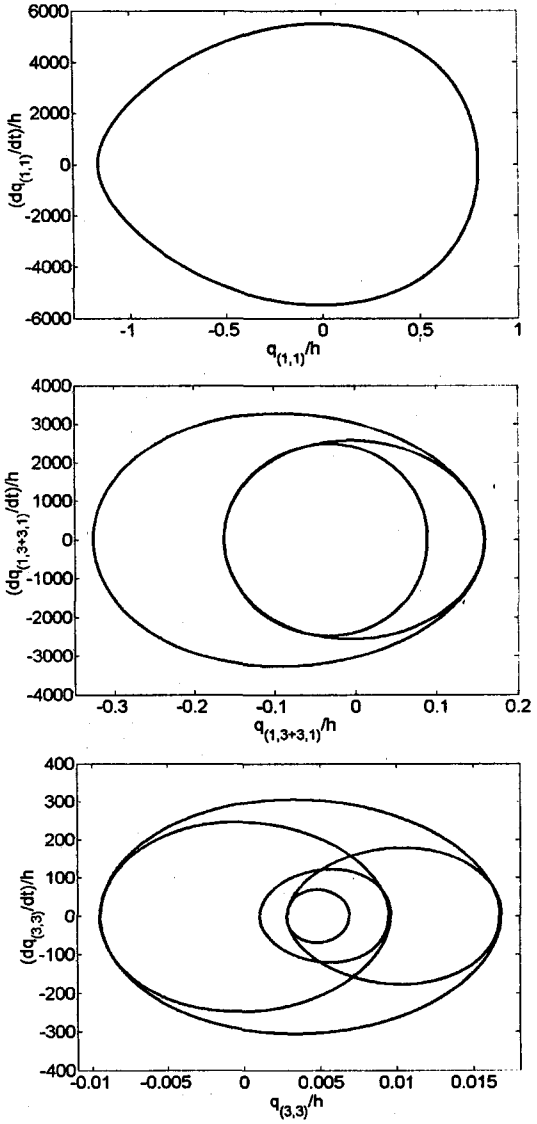

Figure 5.8b 3-mode Solution – Phase Plots for Modes (1,1), (1,3)+(3,1), and (3,3).

It is seen from the aforementioned figures that the multimode solution departs from the single mode solution, especially for the inbound part of the oscillation (negative deflection – shallow shell in compression) and for larger amplitudes. For this reason it was reasonable to show both positive and negative values, namely W_{max}/h and W_{min}/h as a functions of frequency ratio, as presented in Figure 5.9, instead of showing only the positive values, as is traditionally done for isotropic or symmetrically laminated flat plates.

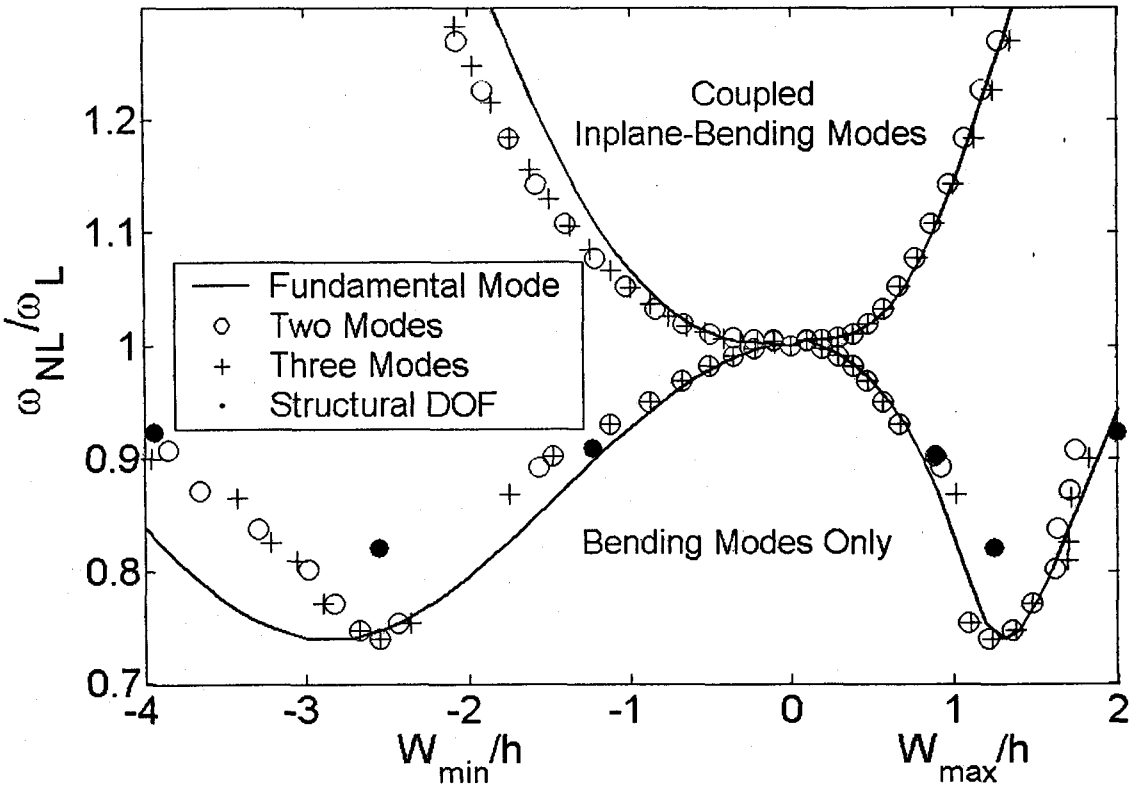

Figure 5.9 Multiple Mode vs. Single Mode Solutions for Isotropic Doubly Curved Shallow Shell

The differences between the fundamental mode solution and the multimode solutions are observed, however the number of modes does not alter the solution characteristics between hardening and softening. On the other hand it is seen that a substantial difference still exists between the two modal FE formulations in expressing the response in terms of coupled bending-inplane modes versus bending modes. Utilizing subscript 1 to refer to mode (1,1), subscript 2 to refer to mode (1,3)+(3,1), and subscript 3 to refer to mode (3,3), the cubic nonlinear terms in each of the three Duffing modal equations are in the form of

$$A_{111}q_1^3 + A_{112}q_1^2q_2 + A_{113}q_1^2q_3 + A_{122}q_1q_2^2 + A_{123}q_1q_2q_3 + A_{133}q_1q_3^2 + A_{222}q_2^3 + A_{223}q_2^2q_3 + A_{233}q_2q_3^2 + A_{333}q_3^3 \tag{5.2}$$

Table 5.5 compares the cubic coefficients of the Duffing equations for two different FE modal formulations, and major differences are revealed. Mode (1,3)-(3,1) is not shown in Figure 5.8, nor Table 5.5 since it does not contribute to W_{max}/h and W_{min}/h. It is also seen in Figure 5.9, that the FE solution in structural DOF compares relatively well with the FE modal solution in bending modes only. The 4x4 mesh coarse discretization gives a slightly overstiff solution obtained in structural DOF compared to FE modal solution in bending modes only. The value of contribution for the r-th mode is defined as

$$Modal\ Participation(\%) = 100\frac{|q_r(t)|}{\sum_{s=1}^{n}|q_s(t)|} \tag{5.3}$$

Table 5.5 Comparison of Coefficients of Cubic Nonlinear Terms of a Duffing-type System Equation of Motion Using the Lowest Three Modes with and without Neglecting Inplane Inertia

Cubic Nonlinear Term Coefficient	Coefficient x 10^9 W/ Inplane Inertia W/o Inplane Inertia		
	1st Eq.	2nd Eq.	3rd Eq.
A_{111}	0.0171 0.0040	-0.0059 0.0065	-0.0104 -0.0022
A_{112}	-0.0089 0.0099	0.1692 0.0448	0.0211 0.0094
A_{113}	-0.0304 -0.0063	0.0408 0.0183	0.2460 0.0374
A_{122}	0.0852 0.0254	0.1221 0.0838	0.0961 0.0372
A_{123}	0.0411 0.0184	0.3727 0.1444	0.0227 0.0235
A_{133}	0.2402 0.0365	0.0220 0.0228	0.0014 -0.0405
A_{222}	0.0205 0.0141	0.2830 0.1097	0.0593 0.0341
A_{223}	0.0938 0.0364	0.3450 0.1982	0.7842 0.2859
A_{233}	0.0111 0.0115	1.5205 0.5542	0.0208 0.0120
A_{333}	0.0005 -0.0132	0.0135 0.0078	1.3554 0.4794

Table 5.6 Modal Participations for Isotropic Doubly Curved Shallow Shell

$\frac{\omega}{\omega_L}$	$\frac{w_{max}}{h}$ $\frac{w_{min}}{h}$	Modal Participation at W_{max}, % Modal Participation at W_{min}, %		
		q_{11}	$q_{13}+q_{31}$	q_{33}
1.0044	0.0988	98.50	1.36	0.13
	-0.1055	98.41	1.47	0.12
0.9982	0.1950	97.03	2.70	0.28
	-0.2232	96.82	2.95	0.23
0.9917	0.2890	95.64	3.93	0.43
	-0.3553	95.15	4.52	0.33
0.9821	0.3813	94.42	4.99	0.59
	-0.5050	93.42	6.18	0.40
0.9695	0.4735	93.55	5.70	0.74
	-0.6768	91.52	8.04	0.45
0.9512	0.5685	93.32	5.79	0.89
	-0.8768	89.42	10.12	0.46
0.9307	0.6749	94.87	4.62	0.87
	-1.1227	86.63	12.85	0.51
0.9029	0.8899	89.90	9.98	0.12
	-1.4858	77.80	21.74	0.46
0.8692	1.0116	84.64	14.44	0.92
	-1.7477	87.06	11.93	1.01
0.7545	1.1022	89.87	8.73	1.40
	-2.3606	97.97	1.33	0.69
0.7396	1.2333	92.01	6.35	1.63
	-2.5480	96.16	3.20	0.65
0.7479	1.3773	95.57	2.99	1.44
	-2.6705	93.05	6.83	0.11
0.7717	1.4751	97.00	2.31	0.70
	-2.8952	91.07	8.29	0.65
0.8160	1.6895	88.54	4.13	7.33
	-3.0547	87.33	10.52	2.15
0.8260	1.6980	89.97	5.07	4.96
	-3.2144	88.71	10.40	0.89
0.8660	1.7116	90.14	6.85	3.02
	-3.4147	88.48	10.45	1.07
0.9010	1.8190	88.66	7.56	3.78
	-3.9575	88.94	10.17	0.89

In particular, the *Modal Participation*, defined in Eq. (5.3), can be calculated at maximum deflection W_{max}, corresponding to time $t = kT$, and at minimum deflection W_{min}, corresponding to time $t = (k+1/2)T$, where T is the period and $k=0,1,2,...$ Sample modal participation values for the case shown in Figure 5.9 are given in Table 5.6, and it is seen that modal participations at W_{max} and W_{min} differ.

A vibrating flat plate always remains in tensile inplane strain. For the shallow shell, the outbound part of oscillation is also associated with positive inplane strain, but for the inbound part of the oscillation the inplane strain becomes negative. For that reason the time when shallow shell remains below the undeflected position is longer than half of the period and the negative deflection has a larger absolute value than the positive deflection.

It is seen that even for the moderately large deflection, on the order of one thickness, the higher mode contributions can reach 20%. It is also observed that the modal participations based on the outbound (maximum) and inbound (minimum) deflections differ. The difference increases as the deflection increases.

5.2.1.3 Lamination Sequence

Responses of cylindrical, rectangular, simply supported composite panels with different lamination stacking, namely anti-symmetrical (0/90), (90/0), (0/90/0/90), (90/0/90/0), symmetrical (0/90/0), and (90/0/90) are investigated. For the (0/90) cylindrical panel, the (0) layer is closer to the center of the cylinder. The composite shallow shell of the same plan - form dimensions and thickness 10 x 15 x 0.050 in. (0.2540 x 0.3556 x 0.00127 m), and curvatures R_x = 100 in. (2.54 m) and Ry = ∞ is

studied. Material properties are E_1 = 26.24 Msi (181.0 GPa), E_2 = 1.49 (10.3), G_{12} = 1.04 (7.17), ν_{12} = 0.28, $\rho = 0.1458 \times 10^{-3}$ lb-sec^2/in.^{4} (1550 kg/m^3).

For anti-symmetrical lamination stacking, additional linear bending-inplane coupling occurs due to the material stiffness [B] not being equal to zero. This additional coupling can influence, depending on stacking sequence, the response characteristics, and either magnify or suppress the softening effect. Although it was found in the previous section that the single mode solution was not of high accuracy, it was also found that additional modes added to the solution refining the results but did not alter softening versus hardening characteristics. Therefore this preliminary study was performed using single mode solution. Since in the previous section it was already concluded that the modal FE formulation in terms of bending modes only produced more accurate results (Figure 5.9), all the composite cases were analyzed according to this formulation.

Table 5.7 presents the first three natural frequencies of the panels where the anti-symmetrical lamination stacking was the strongest. As the sequence of lamination is reversed, the major differences are found with respect to natural frequencies, mode shapes and nonlinear response characteristics. Lamination *(0/90)* results in the fundamental frequency being higher by 16.4% than for lamination *(90/0)*. For the *(0/90)* case, the sequence of mode shapes in increasing natural frequency is (1,1) followed by (3,1) and (1,3) while for the *(90/0)* case the order is (1,1), (1,3) and (3,1). As for nonlinear behavior, lamination sequence *(0/90)* introduces softening characteristics, while lamination *(90/0)* gives purely hardening response.

Table 5.7 Natural Frequencies for Graphite-epoxy Rectangular Cylindrical Simply Supported Panel with Antisymmetrical Lamination Stacking

Lamination	Frequency, Hz		
	Mode (1,1)	Mode (1,3)	Mode (3,1)
(0/90)	381.8	436.8	409.8
(90/0)	327.9	429.1	591.0

More examples are illustrated in Figure 5.10. Generally it is concluded that configurations with lower fundamental frequencies exhibit hardening response characteristics, while these of higher fundamental frequencies exhibit softening response characteristics.

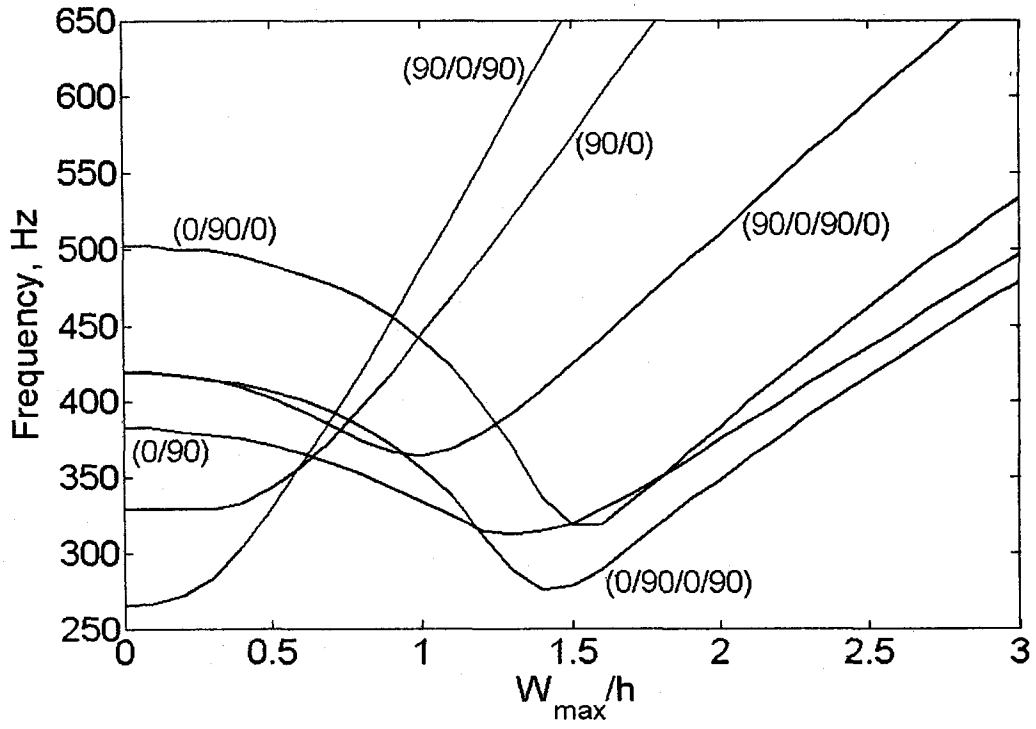

Figure 5.10 Lamination Stacking Influence on the Simply Supported Cylindrical Rectangular Panel Response

5.2.1.4 Summary of Free Vibration Studies

The major difference that was found between two modal FE formulations was one that expresses the solution in terms of coupled bending-inplane modes, and does not neglect inplane inertia, and the other that uses bending modes only and neglects inplane inertia. From the examples studied, it is concluded that the two aforementioned modal FE formulations may give completely different characteristics (hard- or soft-spring), while multiple modes will contribute relatively small adjustments to the nonlinear frequency. Since analytical results are available only under the latter assumptions, FE solution in structural DOF, that holds in account of inplane inertia and includes both – out-of-plane and inplane modes, is used to resolve the ambiguity. Under current assumptions and selected mode sets for each solution the formulation in terms of bending modes only is found to be more accurate. It is apparent that the ratio between bending and inplane displacement in the linear case does not hold constant due to the von Karman type nonlinearity and the ratio changes as the amplitude of vibration increases. Therefore expressing the nonlinear system response in terms of linearly coupled bending-inplane modes, there was a fixed ratio between the bending and inplane parts of the eigenvector and it acts as a constraint on the system, introducing an excessive amount of stiffening. The effect is demonstrated in Table 5.8. Based on the FE in structural DOF, and on the FE modal formulation that allows for inplane versus out-of-plane displacement adjustment, the ratio between maximum inplane ($U_{max}/h = V_{max}/h$) and transverse displacement (W_{max}/h) is calculated. It is seen that the ratio increases significantly as the amplitude of the oscillation increases. Another reason why in this study the formulation in linearly coupled bending-inplane modes did not give the correct shallow shell response

maybe also due to the subset of selected modes that does not incorporate all the dynamics of system being modeled.

Table 5.8 Inplane Versus Out-of-plane Displacement for Various Amplitudes of Doubly Curved Isotropic Shell Supported by Shear Diaphragms

Coupled Linear Bending - Inplane

$U_{max}/ W_{max} = 2.07$ %

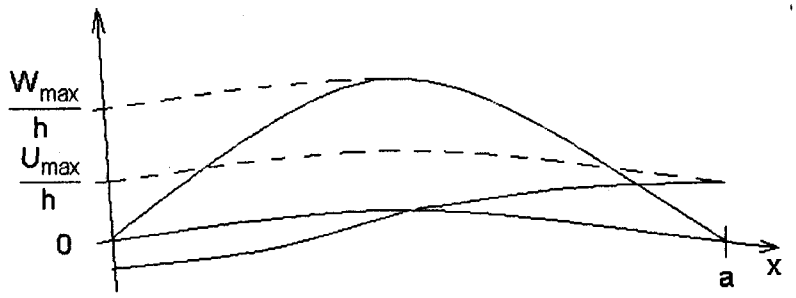

W_{max}/h	U_{max}/h	$\lvert U_{max}/ W_{max} \rvert$ %	Method
0.890	0.022126	2.49	Structural DOF
1.000	0.028897	2.89	Single Mode
1.012	0.027695	2.74	Three Modes
1.248	0.036981	2.96	Structural DOF
1.819	0.060014	3.30	Three Modes
1.989	0.075268	3.78	Structural DOF
3.000	0.135909	4.53	Single Mode
-1.232	0.033634	2.73	Structural DOF
-2.553	0.081945	3.21	Structural DOF

5.2.2 Random Response

5.2.2.1 Simulated Gaussian Bandlimited White Noise Excitation

A 10 x 15 x 0.050 in. (254 x 381 x 1.27 mm) graphite-epoxy shallow cylindrical shell ($R_y=\infty$) was studied. Since the softening effect in shallow shell response (that is within the scope of this work in contrast to the hardening response for flat isotropic or orthotropic plates investigated previously by Mei et al.[35] and Dhainaut[36]) can be induced by both the curvature and the lamination stacking, different radii R_x, and lamination sequences are investigated. Also different support conditions were studied. The material properties for the graphite-epoxy composite are the same as listed in Section 5.2.1.3. Additionally, for the cases involving an elevated thermal environment, the coefficients of thermal expansion are $\alpha_1 = -0.072\text{x}10^{-6}$ 1/°C (-0040x10^{-6} 1/°F) and $\alpha_2 = 30.06\text{x}10^{-6}$ 1/°C (16.70x10^{-6} 1/°F). The modal damping, ς_1, is assumed to be 0.02. The advantage of symmetry of the structure and the applied load is again taken for refined discretization, and one quarter of the shell is modeled with a 10x10 mesh, or 200 triangular elements. This corresponds to 498 structural DOF for simply supported and 442 structural DOF for clamped boundaries. The cut-off frequency, f_c, of the simulated white noise is set to 2048 Hz, which is more than double the natural frequency corresponding to the highest mode retained in the analysis for all cases studied. Modal convergence is studied and presented along with modal participations in Table 5.9. The modal participation value is defined as

$$r^{th} - mode\ participation = \frac{RMS\ (q_r)}{\sum_{s=1}^{n} RMS\ (q_s)} \tag{5.4}$$

It is seen that excellent modal convergence is reached with the use of 6 modes. The difference in RMS (W_{max}/h) obtained with 5 and 6 modes retained in the analysis is only 0.11%. It is interesting to notice that for the 6-mode solution, the participation of the 6^{th} mode is 3.24%. However the response RMS (W_{max}/h) is affected by a fraction of this number (0.11%). To help understand this phenomenon the ratio of modal participation for two modes corresponding to the two lowest natural frequencies is also shown in Table 5.9. The addition of a higher mode does not simply contribute additional value that is always a "net gain," but it also alters the relative contribution of the lower modes. The ratio between modal participation of mode (3,1) versus mode (1,1) is 1.173 for the 2-mode solution and 0.775 for the 6-mode solution.

Table 5.9 Modal Convergence and Modal Participations for (0/90) Simply Supported Cylindrical Shell of R_x = 75 in. at SPL = 137 dB

Number of Modes	RMS (W_{max}/h)	Modal Participation %						Participation (3,1) vs. Participation (1,1)
		(3,1)	(1,1)	(3,3)	(1,3)	(1,5)	(3,5)	
2	1.9268	53.99	46.01					1.173
3	2.0096	38.45	46.72	14.83				0.823
4	2.0712	32.52	40.98	17.41	9.09			0.794
5	2.0782	29.62	37.97	15.40	12.29	4.71		0.780
6	2.0804	28.39	36.63	14.20	10.89	6.63	3.24	0.775

Certainly, a modal convergence study should be performed on an individual basis for each shallow shell configuration and pressure excitation level, but excellent convergence was obtained for the case of very small radius. The highest excitation level investigated is seen to be very representative for all the cases studied. The lowest six mode shapes for a simply supported (0/90) cylindrical panel are presented in Figure 5.11. The

corresponding natural frequencies for different curvature ratios are presented in Table 5.10.

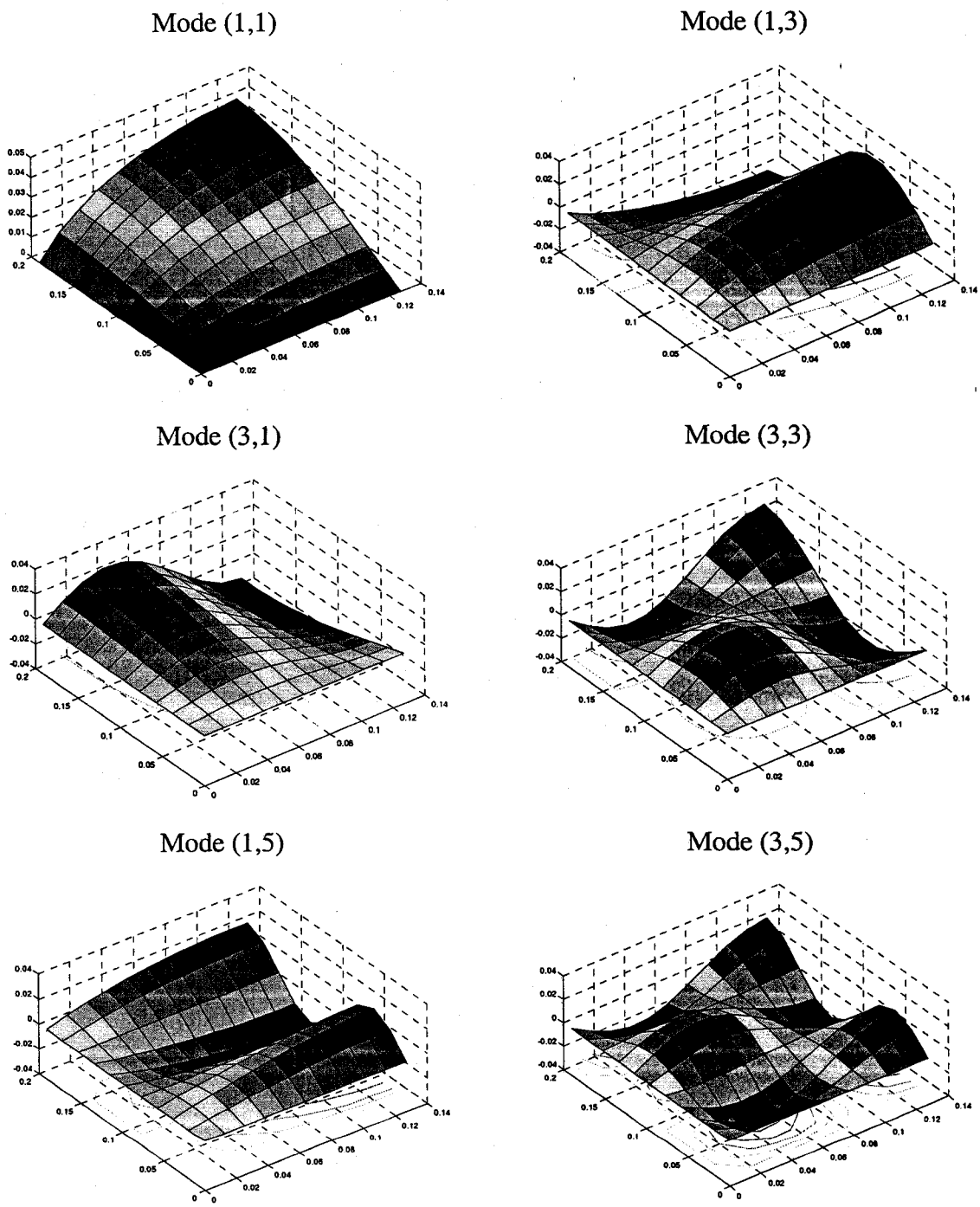

Figure 5.11 Six Lowest Mode Shapes for Simply Supported (0/90) Cylindrical Panel (Quarter of Panel Shown)

Table 5.10 The Lowest Six Modes and Corresponding Natural Frequencies (Hz) of Cylindrical Panel

R_x in.	B.C. & Lamination	(1,1)	(1,3)	(3,1)	(3,3)	(1,5)	(3,5)
∞	SS (0/90)	73.71	219.10	435.05	538.50	546.43	827.50
150	SS (0/90)	240.59	320.51	418.39	530.92	591.35	821.01
75	SS (0/90)	530.36	579.56	418.16	542.29	762.79	848.95
75	SS (90/0)	359.31	495.79	687.29	749.09	779.87	972.31
75	CL (0/90)	462.65	577.24	688.72	773.52	849.03	1015.44

Two groups of modes can be identified for simply supported (0/90) cylindrical panels of different radii are shown. The first group has natural frequencies that vary significantly with increases in curvature, and modes (1,1), (1,3), and (1,5) fall into this category. On the other hand frequencies corresponding to modes (3,1), (3,3), and (3,5) are affected only slightly by the curvature R_x only changes. It is interesting to notice that the first group has only one semi-sine wave along the curved edge, while the second group has 3 semi-sine waves along the curved edge. Comparing cylindrical panels of the same radii and inverted lamination stacking it is observed that lamination (0/90) results in the first six natural frequencies being spaced more closely than for lamination (90/0). For the (0/90) case the fundamental mode has a corresponding frequency of 418.16 Hz, and the sixth natural frequency mode is 848.95 Hz, while for the (90/0) case the frequencies are

359.31 Hz and 972.31 Hz, respectively. Mode switching is also observed. For lamination stacking (0/90) and simply supported boundaries, mode ordering by frequency is (3,1), (1,1), (3,3), (1,3), (1,5), and (3,5), while for all the other cases studied and presented in Table 5.10, the sequence is (1,1), (1,3), (3,1), (3,3), (1,5), and (3,5). It is also seen that clamped boundary conditions result in natural frequencies that are higher than for the simply supported case with the same curvature of the panel. For the simply supported (0/90) cylindrical shell of R_x=75 in. the modal participation values as functions of excitation pressure level are presented in Table 5.11.

Table 5.11 Modal Participation (%) for a (0/90) Simply Supported Panel of R_x = 75 in.

				Mode Shape, Frequency and Participation					
SPL	OASPL	RMS (p)	RMS	(3,1)	(1,1)	(3,3)	(1,3)	(1,5)	(3,5)
dB	dB	psi	(W_{max}/h)	418.16	530.36	542.29	579.56	762.79	848.95
90	123.11	0.0042	0.0044	8.45	53.80	3.01	20.95	10.19	3.61
100	133.11	0.0131	0.0141	8.76	53.52	3.24	20.92	10.14	3.42
110	143.11	0.0415	0.0470	11.63	49.81	6.08	19.94	9.42	3.12
120	153.11	0.1313	0.1847	22.97	35.66	15.73	15.05	7.03	3.57
125	158.11	0.2335	0.3066	26.56	34.62	15.78	12.53	6.71	3.80
128	161.11	0.3299	0.5070	26.94	33.65	15.78	12.91	7.14	3.58
131	164.11	0.4660	0.9285	26.62	36.01	14.90	12.03	6.76	3.68
134	167.11	0.6582	1.4497	27.59	35.14	14.91	11.85	6.70	3.81
137	170.11	0.9297	2.0804	28.39	36.63	14.20	10.89	6.63	3.24

Large variations of modal participation value are observed. For low excitation pressure, mode (1,1) makes a dominant contribution to RMS (W_{max}/h). As the level of random pressure increases from SPL = 90 dB to SPL = 137 dB, the participations of mode (1,1) and mode (1,3) are suppressed from 53.80% to 36.63%, and from 20.95% to 10.89%, respectively. At the same time, participations of mode (3,1) and mode (3,3) increase from 8.45% to 28.39%, and from 3.01% to 14.20%, respectively. Participation of modes (1,5) and (3,5) are affected relatively little.

The RMS of the nondimensionalized maximum deflection at the panel center (W_{max}/h) versus excitation pressure for the (0/90) lamination for two different radii, R_x, are presented and compared with results for the flat panel ($R_x = \infty$) in Figure 5.12.

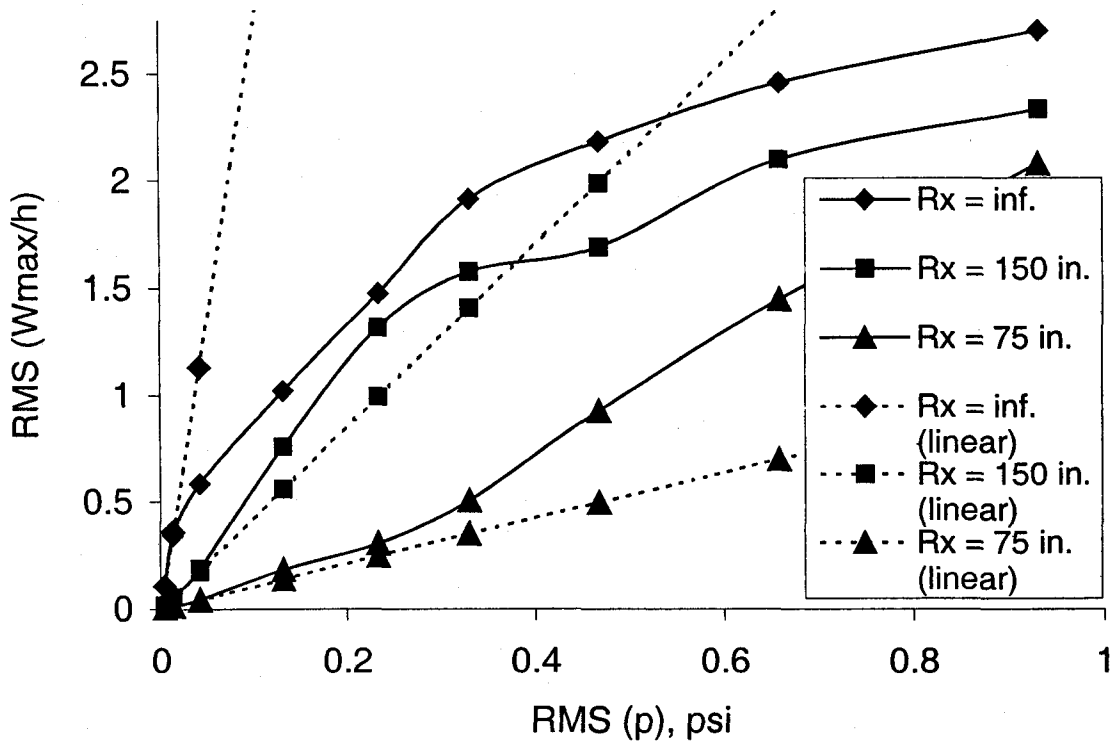

Figure 5.12 Nonlinear and Linear RMS (W_{max}/h) Versus Excitation Pressure for Graphite-epoxy Simply Supported Cylindrical Shallow Shell of Different Curvatures

Figure 5.12 demonstrates clearly that the smaller the radius the softer the shell panel response. It is also observed that for the flat plate, the linear solution will always over-predict the nonlinear response. On the other hand, for the panel with R_x = 75 in., the linear solution will always under-predict the nonlinear response. Table 5.12 presents modal participations for selected radii and excitation pressure levels. It is observed that for a panel with small radius, R_x = 75 in., at moderate and high excitation pressures, the contribution of mode (1,1) can be as low as approximately 1/3 of the total RMS(W_{max}/h). Even for relatively larger radius (R_x = 150 in.) and significantly lower excitation pressure (100 dB) the contribution of mode (1,1) is slightly more than 1/2. This leads to the conclusion that the single mode solution would not yield accurate results. The statistical moments of the response, including mean, variance, skewness and kurtosis, are presented in Table 5.13.

Table 5.12 Modal Participation (%) for (0/90) Simply Supported Cylindrical Shell of Different Radii at 100, 125 and 137 dB

SPL	RMS(p)	Radius	RMS	Modal Participation %					
dB	psi	R_x, in.	(W_{max}/h)	(1,1)	(1,3)	(3,1)	(3,3)	(1,5)	(3,5)
		75	0.0141	53.52	20.92	8.76	3.24	10.14	3.42
100	0.0131	150	0.0560	63.11	16.33	9.77	3.54	5.76	1.50
		inf.	0.3426	81.20	9.12	4.89	3.12	1.20	0.46
		75	0.3066	34.62	12.53	26.56	15.78	6.71	3.80
125	0.2335	150	1.3195	62.69	11.14	13.53	5.50	4.59	2.56
		inf.	1.4764	61.14	11.97	9.54	7.79	6.80	3.06
		75	2.0804	36.63	10.89	28.39	14.20	6.63	3.24
137	0.9297	150	2.3374	60.01	13.20	12.49	6.25	5.53	2.53
		inf.	2.7040	58.29	13.68	8.27	9.05	7.81	2.90

Table 5.13 Statistics of the Panel Center Maximum Deflection for (0/90) Simply Supported Cylindrical Shell of $R_x = 75$ in.

SPL dB	RMS (W_{max}/h)	Mean in./in.	Variance $in.^2/ in.^2$	Skewness $in.^3/in.^3$	Kurtosis $in.^4/in.^4$
90	0.0044	0.0000	0.0046	-0.0053	-0.1008
100	0.0141	0.0002	0.0147	-0.0153	-0.0686
110	0.0470	0.0018	0.0487	0.0427	0.1077
120	0.1847	-0.0091	0.1863	-0.3851	0.4778
125	0.3066	-0.0423	0.2997	-0.5239	0.6633
128	0.5070	-0.1168	0.4722	-0.9016	1.5409
131	0.9285	-0.3837	0.9719	-1.1929	1.6290
134	1.4497	-0.7212	1.3082	-0.7033	0.1989
137	2.0804	-1.1074	1.7336	-0.3908	-0.5124

Negative values of mean and skewness are the result of the softening effect demonstrated later in this section (Figure 5.14a). As expected, the value of the variance becomes larger as the excitation level increases. Small and large amplitude response characteristics are presented in Figures 5.13a and 5.13b, respectively, with deflection time histories, power spectral densities (PSD), and probability density functions (PDF). At the low SPL of 90 dB, the 6 modes can be seen clearly in the PSD plot. At the high SPL of 137 dB, the peak is broadened and shifted to the right, as is typical for nonlinear random response. Both responses reveal non-Gaussian characteristics due to softening-hardening effect.

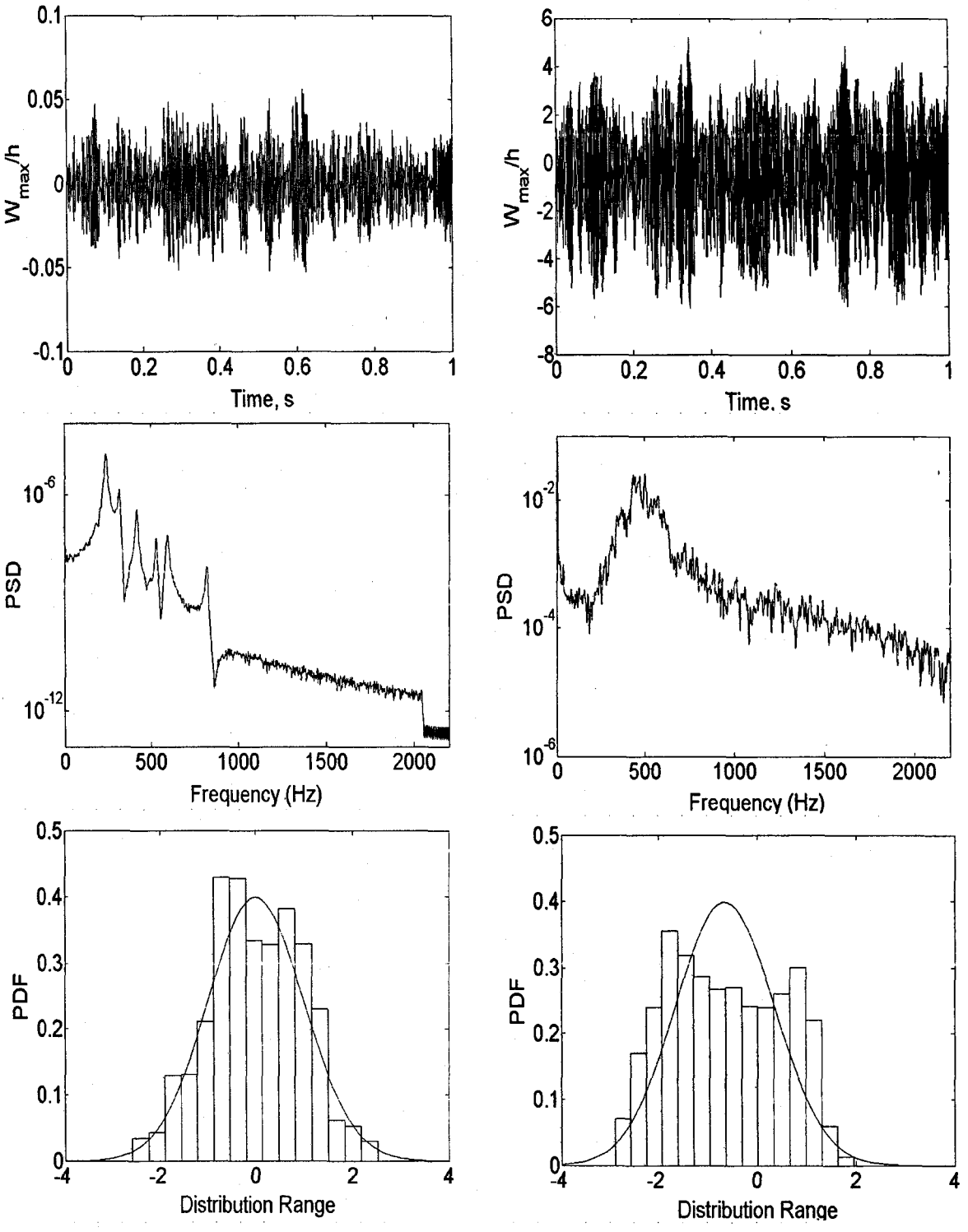

(a) (b)

Figure 5.13 Random Response of (0/90) Graphite-epoxy Simply Supported Cylindrical Panel of R_x=150 in., (a) SPL=90 dB, (b) SPL=137 dB

Comparison of the random nonlinear response with the linear solution for a cylindrical panel of R_x=75 in. and two different lamination stacking sequences of (0/90) and (90/0) is presented in Figures 5.14a and 5.14b, respectively. It is found that lamination sequence (0/90) makes the softening effect very pronounced (Figure 5.14a), while the reverse sequence of lamination (90/0) reduces the amount and range of softening response (Figure 5.14b). Comparing RMS (W_{max}/h) for the abovementioned two lamination stackings, regardless of their relations to the corresponding linear response, it is found that the (0/90) configuration will yield higher RMS (W_{max}/h) compared to (90/0).

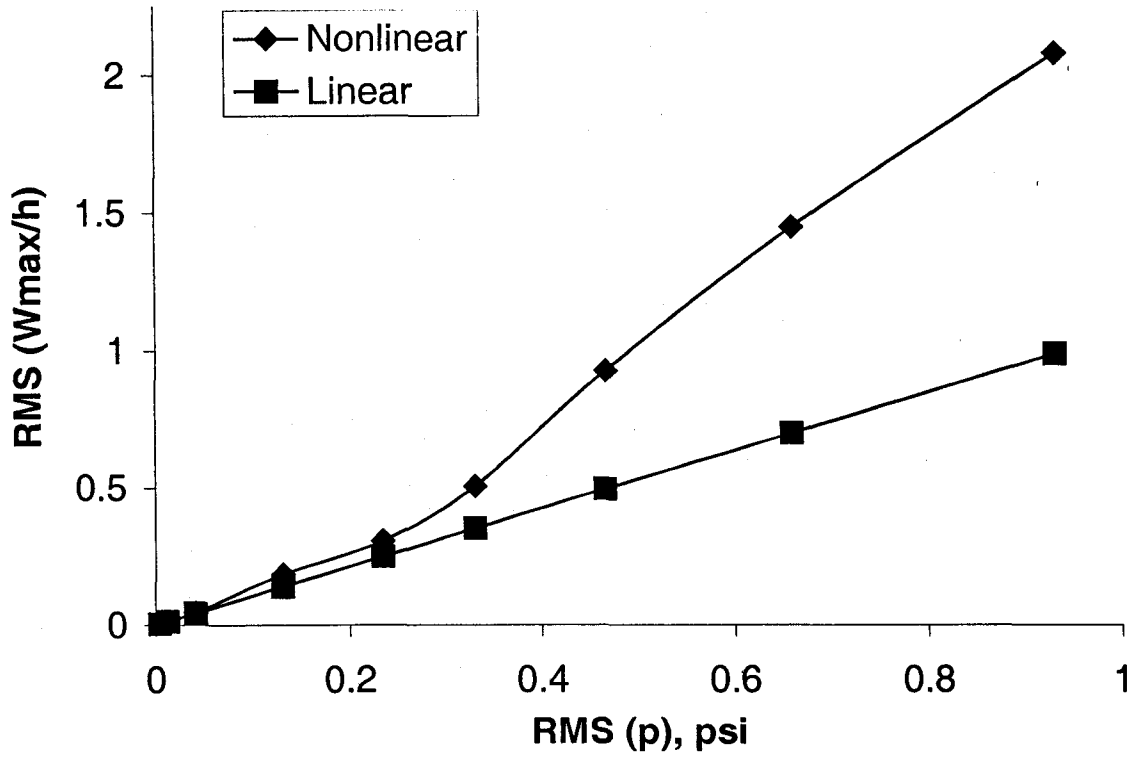

Figure 5.14a Linear and Nonlinear Response of (0/90) Cylindrical Simply Supported Panel of R_x = 75 in.

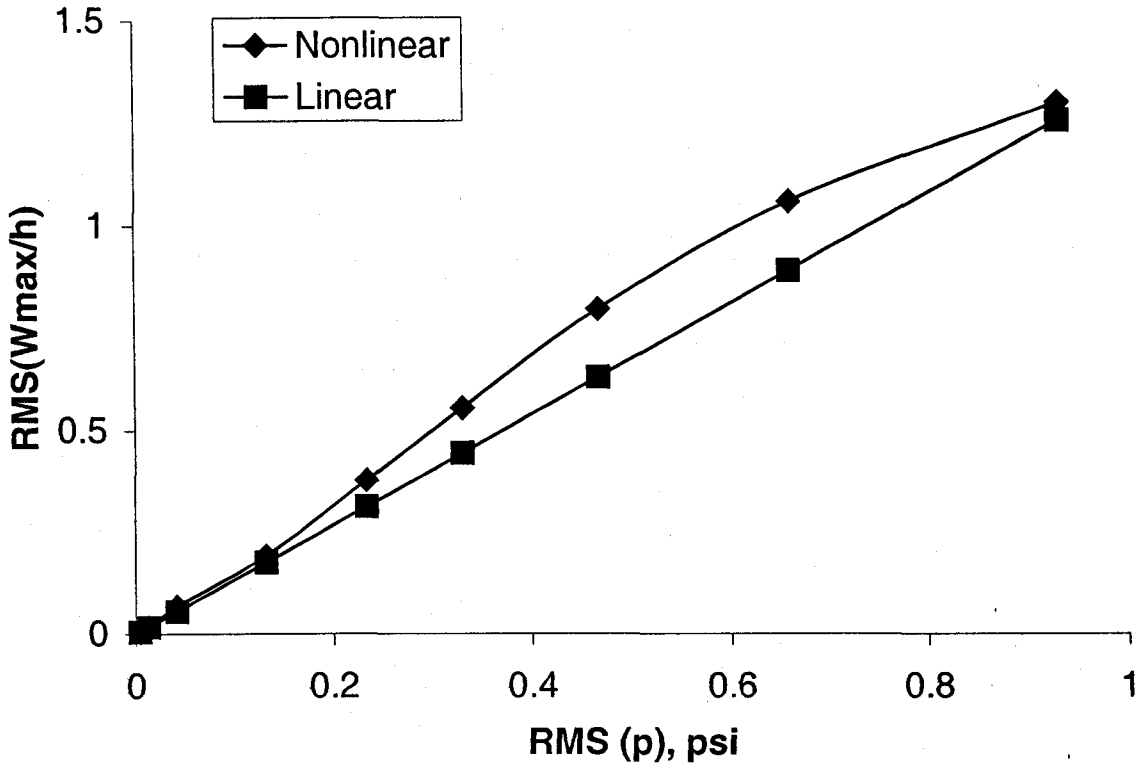

Figure 5.14b Linear and Nonlinear Response of (90/0) Cylindrical Simply Supported Panel of $R_x = 75$ in.

Subsequently, the random response of a fully clamped (0/90) cylindrical shallow shell panel of $R_x = 75$ in. in a uniformly elevated temperature was studied. First, the FE modal approach presented by Shi et al.[98,99] was used and the Newton-Raphson method was employed to solve the static thermal problem. Figure 5.15a and Figure 5.15b are the shape of the thermally deflected panel at $\Delta T = 180$ °F. It is found that mode (1,1) is not dominant for the thermally deflected panel, and therefore the deflection of the center of the panel (W_c/h) does not coincide with the maximum deflection (W_{max}/h). The maximum thermal deflections are located at $x = 5.00$ in., $y_1 = 3.75$ in. and $x = 5.00$ in., $y_2 = 11.25$ in., and not at $x = 5.00$ in. and $y = 7.5$ in. that corresponds to the center of the panel.

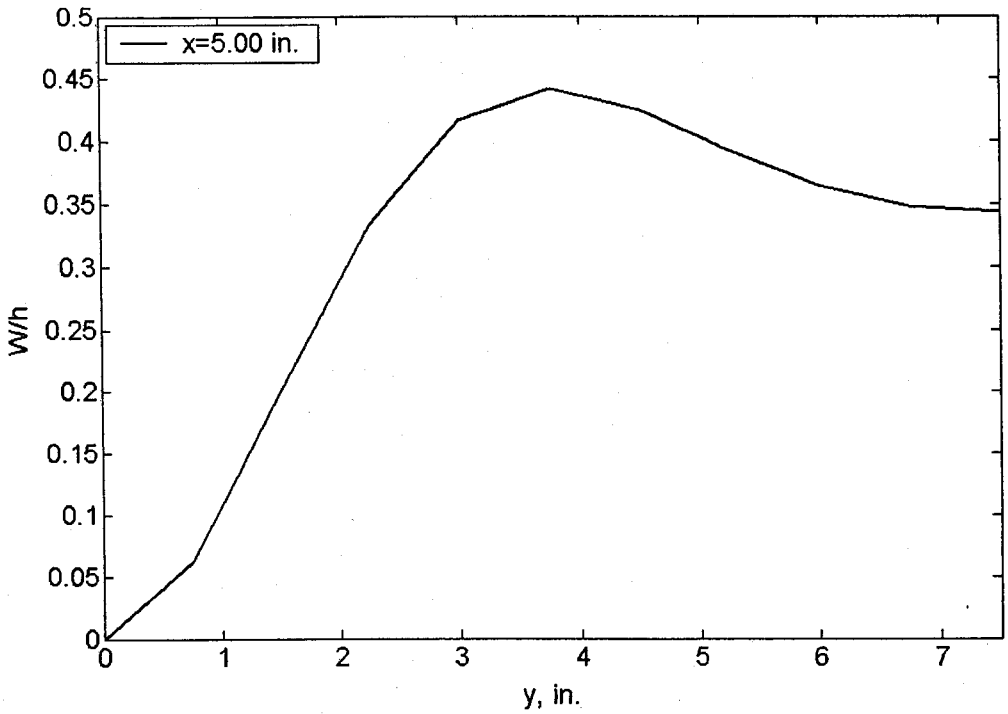

Figure 5.15a Thermal Deflection Along y-axis for x = 5.00 in. at ΔT = 180 °F

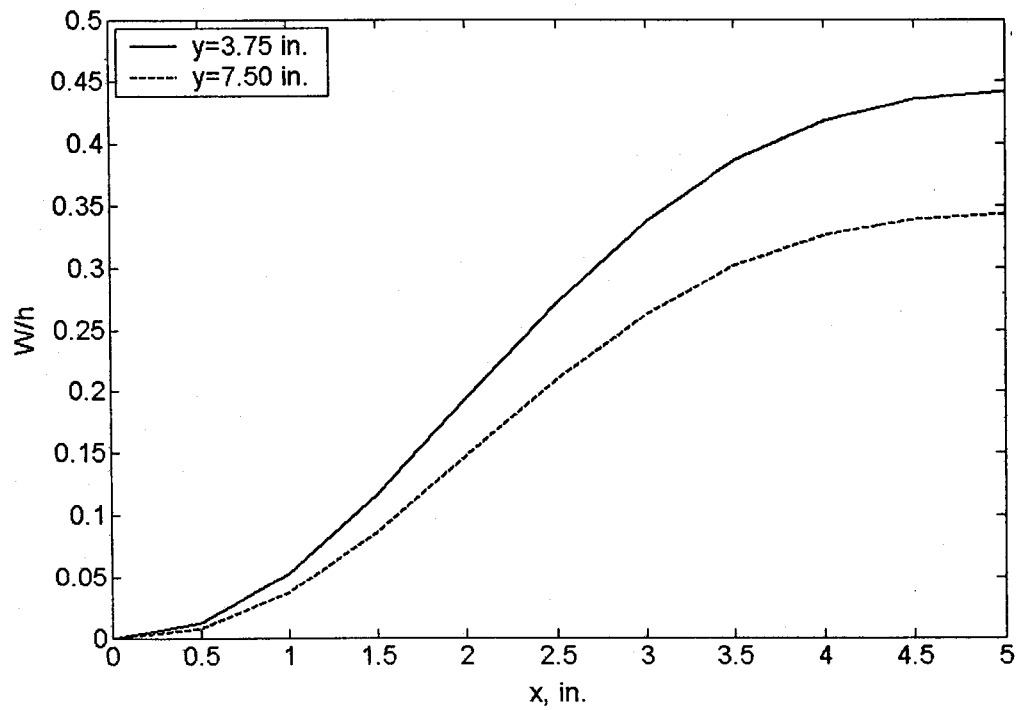

Figure 5.15b Thermal Deflection Along x-axis for y = 3.75 in. and y = 7.50 in. at ΔT = 180 °F

The random response of a uniformly heated shallow shell is presented and compared with the response at room temperature in Figure 5.16. There are four curves shown in the figure. Two curves describe the response of the center of the panel RMS (W_c/h), and the other two curves describe the response of the point corresponding to the maximum thermal static deflection, say RMS (W_a/h). Since the location of the thermal maximum deflection corresponds to RMS (W_{max}/h) only at the lower range of excitation pressure levels, subscript "a" is used rather than "max." It is seen from Figure 5.16 (and explicitly shown in Figure 5.17) that the point at which the maximum thermal static deflection coincides with the maximum RMS of the random response is in the range of excitation pressure level RMS (p) from 0 to approximately 0.22 psi (note: RMS (p) = 0.22 psi is greater than SPL = 120 dB and smaller than SPL = 125 dB). Above RMS (p) = 0.22 psi, the maximum RMS of random the response occurs at the panel center. In other words RMS (W_{max}/h) does not coalesce with RMS (W_c/h) at low levels of random pressure excitation, up to RMS (p) = 0.22 psi, where the thermal deflection has a prevailing impact on the panel response. As the excitation pressure increases, the response of the panel becomes dominated by the deflection caused by the acoustic load, and the maximum deflection migrates to the center of the panel. It also needs to be pointed out that in general there is no guarantee that the location of RMS (W_{max}/h) will always coincide with the location of RMS (ε_{max}).

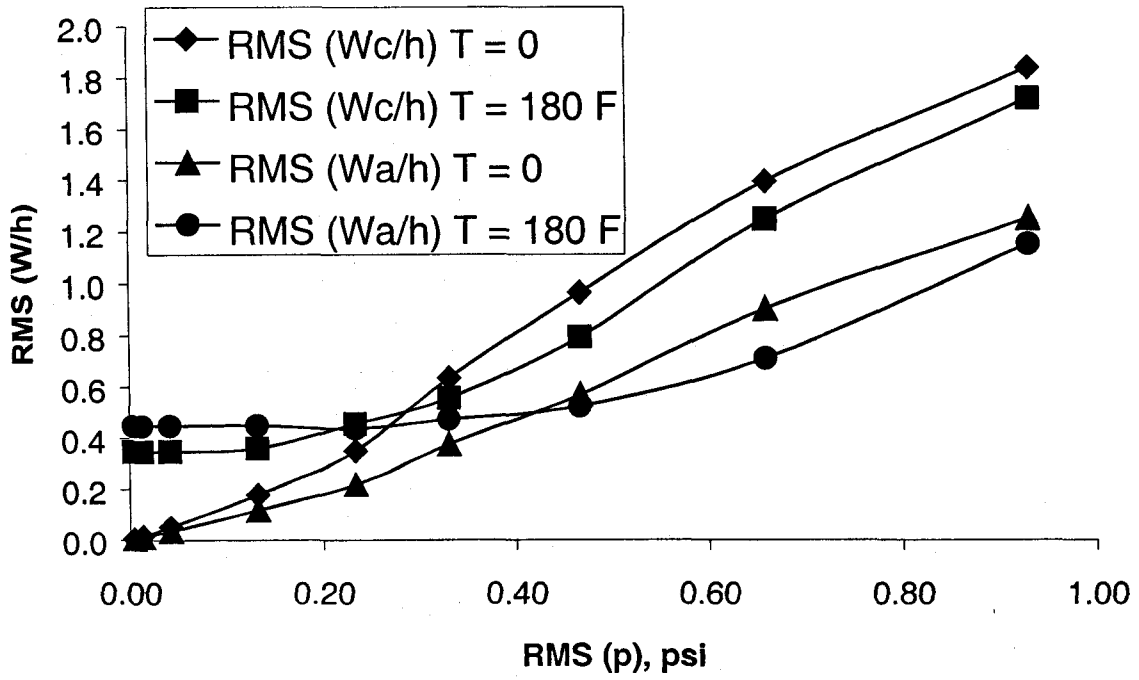

Figure 5.16 Random Response of (0/90) Graphite-epoxy Clamped Cylindrical Panel of R_x=75 in. at $\Delta T = 0$ and $\Delta T = 180°F$

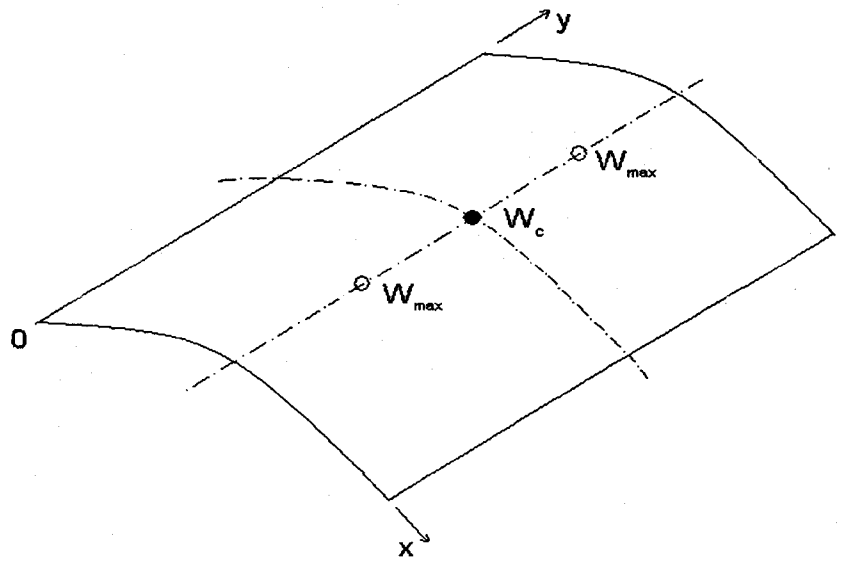

Figure 5.17 Clamped Panel at Elevated Temperatures of ΔT = 180 °F - Location of Maximum Deflection at Static Thermal Load, and Maximum RMS of Deflection at Low Level of Excitation Pressure up to RMS (p) = 0.22 psi

Moderate and large amplitude response characteristics in elevated temperature of ΔT=180 °F (100 °C) are presented in Figure 5.18, with the deflection time history, PSD, and PDF. For a moderate SPL of 110 dB, 4 modes can still be seen clearly in the PSD plot. It is observed that the first mode (1,1) and sixth mode (3,5) are suppressed, and the remaining four modes are shifted with respect to their linear frequencies. This is consistent with thermal static deflection having its maximum not at the panel center, but in the location corresponding to the second mode (1,3).

The fact that static thermal deflections (W_c/h) and (W_{max}/h) do not coincide must be accounted for, not only while attempting to estimate the RMS of maximum deflection, but also for fatigue life due to combined random pressure excitation and thermal loads. The location of the RMS of maximum strain must be sought on an individual basis.

For a curved panel of lamination (0/90), either fully simply supported or fully clamped, exposed to spatially uniform and constant through the thickness elevated temperature of up to ΔT = 180°F (100°C), no snap-thru phenomenon was detected. The bifurcation for a temperature increase of up to ΔT = 180°F was found only for the flat (0/90) laminated panels. Flat composite plates with antisymmetrical laminations were investigated by Mei et al.[35] and Dhaunait,[36] and are beyond the scope of this work. In general, it is seen that a skin panel should not be designed to work under snap-thru conditions, since this will significantly reduce the fatigue life of a structure.[36]

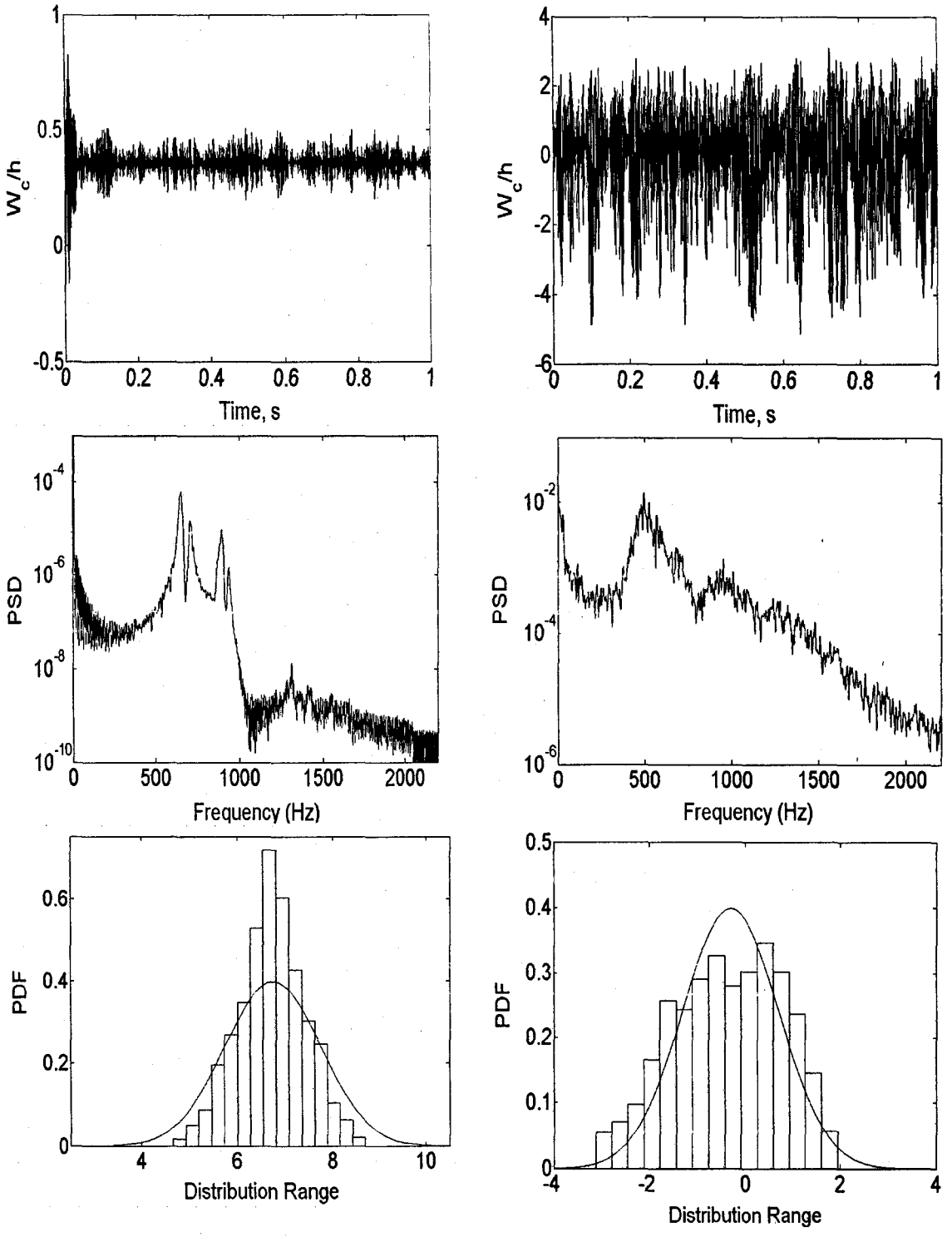

Figure 5.18 Random Response of (0/90) Graphite-epoxy Clamped Cylindrical Panel of R_x = 75 in. at ΔT=180 °F (100 °C): (a) SPL = 110 dB, (b) SPL = 137 dB

5.2.2.2 Microphone In-flight Recorded Pressure Fluctuation Versus White Noise

The in-flight recorded random pressure fluctuations described previously in Section 4.7.2 are now used as the excitation. As outlined before the overall sound pressure level of the in-flight recorded pressure fluctuation is 163.014 dB, what for cut-off frequency of f_c = 2048 Hz corresponds to truncated white noise of SPL = 129.901 dB. Panel dimensions and material properties are the same as these presented in Section 5.2.1.3, with coefficients of thermal expansion introduced in Section 5.2.2.1. Also, similar to the previous section, the 6-mode solution was used. Table 5.14 presents the comparison of RMS (W_{max}/h) for two different lamination stacking sequences used previously in Section 5.2.2.1, and Table 5.15 presents a comparison for the clamped cylindrical shallow shell at room and at a uniformly elevated temperature of 180°F (100°C).

Table 5.14 Effect of Lamination on Random Response RMS (W_{max}/h) for Simply Supported Shallow Shell of R_x = 75 in. for Truncated White Noise and In-Flight Recorded Pressure Fluctuation

	(0/90)	(90/0)
White Noise	0.8509	0.7813
In-flight Data	1.0122	0.7896
Difference, %	15.9	1.1

Table 5.15 Effect of Uniformly Elevated Temperature on Random Response RMS (W_{max}/h) for clamped (0/90) Shallow Shell of R_x = 75 in. for Truncated White Noise and In-Flight Recorded Pressure Fluctuation

	$\Delta T = 0$	$\Delta T = 180°F$
White Noise	0.9132	0.7799
In-flight Data	1.0438	0.8939
Difference, %	12.5	12.8

Good agreement between the response to the truncated white noise and in-flight captured pressure fluctuation was found only for simply supported shell with (90/0) lamination stacking. For the three other cases investigated the difference ranged from 12.5 to 15.9 %. Therefore it was concluded that the same amount of energy carried by the excitation spectrum (equivalent area under PSD curve) provides relatively weak similarity conditions for excitation modeling, and the distribution of energy over the excitation bandwidth can significantly affect the response.

Attempting to interpret results of Table 5.15, it is important to realize that for unheated shallow shell panels, due to presence of the softening response characteristics originating from the combined effects of curvature and lamination stacking, the inbound part of the oscillation (negative W/h) exhibits larger deflections compared with the outbound part of the oscillation (positive W/h). For the heated shallow shell panel

however, the static thermal deflection shifts the equilibrium position towards positive deflection W/h, and therefore tends to make the response more symmetric in the sense that inbound and outbound deflections have comparable absolute values. As an example, let us consider a shallow shell oscillating at constant amplitude (assumed for simplicity). Due to compression in the inbound part of the oscillation and tension in the outbound part of oscillation, let us also assume that the amplitude ranges from $W_{max}/h = +0.5$ to $W_{min}/h = -1.0$. Now, let us assume that the panel is heated to a temperature resulting in the thermal static deflection of $\Delta W/h = +0.3$. Again, for simplicity, let us assume that this thermal static deflection is small enough, that the original amplitude of the oscillation is not affected, and is simply superimposed on the static thermal deflection. That results in $W_{max}/h = +0.8$ and $W_{min}/h = -0.7$. Now, compare the RMS of deflection at room and elevated temperature. They are 0.7906 and 0.7517, respectively implying that the thermal static deflection of $\Delta W/h = +0.3$ reduced the value of RMS (W_{max}/h) by over 5%. This argument is applicable for deflection, but not necessarily applicable for strains, since the positive thermal deflection will be associated with negative inplane strain.

Finally, a nonrectangular graphite-epoxy cylindrically curved panel (of $R_x = 100$ in. and $R_y = \infty$, where the longer edge is straight) with complicated boundary conditions, at elevated temperature with gradient across the thickness was studied to demonstrate the robustness of the present formulation. The geometry is shown in Figure 5.19. The left and top edges are clamped, and the bottom and right edges are simply supported. The thickness of the shell is $h = 0.050$ in. The uniform temperature increase is $\Delta T = 180$ °F (100 °C), the temperature gradient through the thickness is $\Delta T_h = 7.2$ °F (4 °C), so the outside surface has a temperature of 187.2 °F (104 °F). Based on the previously analyzed

rectangular study cases, lamination (90/0), resulting in the stiffening characteristics, is chosen. The location of the maximum RMS (W_{max}/h) is also shown in Figure 5.19. Random response was calculated for both – in-flight recorded pressure fluctuation and simulated truncated white noise. Additionally, to show the variation of the deflection upon the excitation pressure level, the response was recalculated for other levels of excitation pressure. A comparison of the response to in-flight recorded pressure fluctuations and the corresponding white noise, as well as the variation of panel deflection RMS (W_{max}/h) as a function of white noise excitation pressure level are presented in Table 5.16. The difference between the RMS (Wmax/h) for the truncated white noise and in-flight recorded random pressure fluctuation was 3.7%.

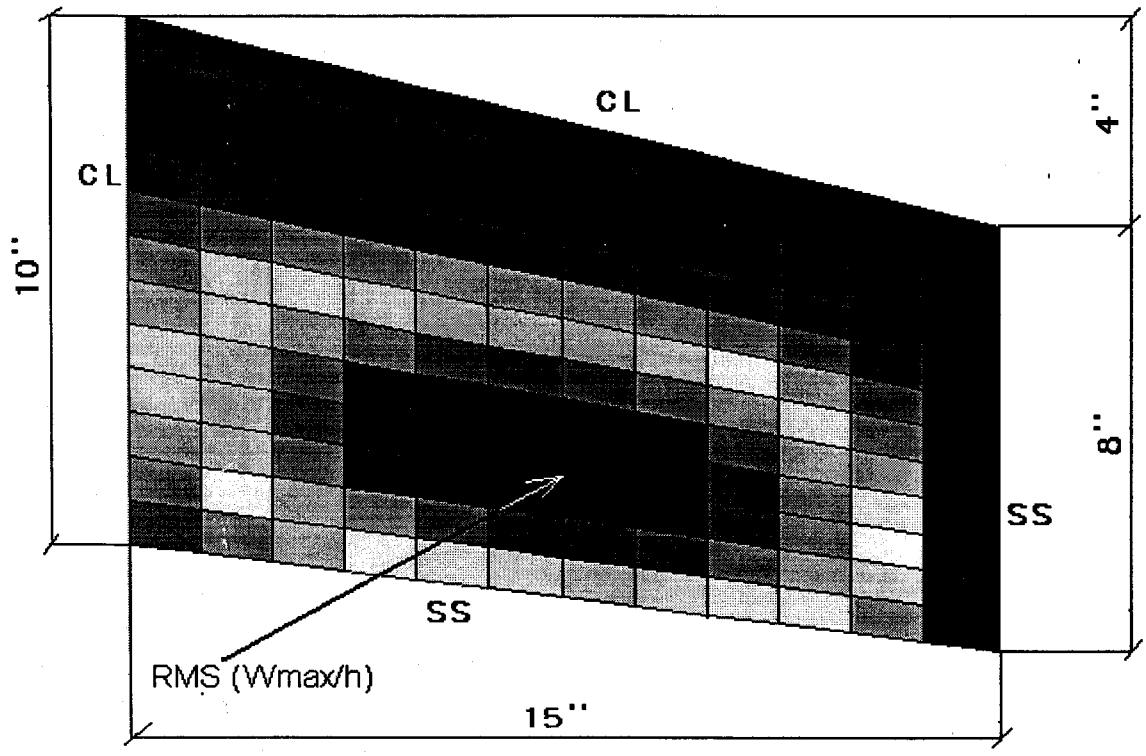

Figure 5.19 Nonrectangular Graphite-epoxy (90/0) Cylindrically Curved Panel with Complicated Boundary Conditions at Elevated Temperature with Gradient Through the Thickness

Table 5.16 RMS (W_{max}/h) of Nonrectangular Graphite-epoxy Cylindrical Panel with Complicated Boundary Conditions at Elevated Temperature with Gradient Across the Thickness

SPL dB	RMS (W_{max}/h)
90	0.4596
100	0.4612
110	0.4774
120	0.6172
125	0.8654
128	1.1336
131	1.5344
134	2.1186
137	2.9573
In-flight	1.4579
White noise	1.5147

5.2.3 Fatigue Life

In this section the maximum strain histories are obtained and are processed further in order to estimate fatigue life. Strain versus the number of cycles to failure curve (S-N curve) for graphite-epoxy composite is characterized[36] by $K=1.37x10^{28}$ and $\beta=9.97$. In order to investigate the influence of intensity of random acoustic excitation on the fatigue life of a curve panel, truncated white noise of different amplitudes was used. Fatigue life was predicted for cases of room and elevated temperatures. Then, the fatigue life based

on the response to in-flight recorded pressure fluctuations was calculated, for room and elevated temperatures. Finally, the results obtained for the in-flight recorded data are compared with the results of the corresponding truncated white noise.

5.2.3.1 Simulated Gaussian Bandlimited White Noise Excitation

RMS (ε_{max}) versus excitation pressure RMS (p) for a graphite-epoxy, simply supported cylindrical shallow shells of different radii were calculated and are presented in Table 5.17. It is found that for simply supported boundaries RMS (ε_{max}) occurs at the plate center.

Table 5.17 RMS (ε_{max}) for (0/90) Simply Supported Cylindrical Shells of Different Radii

SPL	RMS (p)	RMS (ε_{max}) x 10^{-3}		
dB	psi	$R_x = \infty$	R_x = 150 in.	R_x = 75 in.
90	0.0042	0.0018	0.0065	0.0214
100	0.0131	0.0059	0.0208	0.0626
110	0.0415	0.0237	0.0737	0.1385
120	0.1313	0.1680	0.3607	0.3136
125	0.2335	0.3186	0.6305	0.4430
128	0.3299	0.4832	0.7532	0.5048
131	0.4660	0.7651	0.8203	0.6456
134	0.6582	1.2073	0.9915	0.7738
137	0.9297	1.6297	1.1111	0.8914

It is seen that at low levels of excitation pressure, smaller radius R_x yields higher strains. The trend reverses as the excitation pressure increases, and at the two highest random pressure excitation levels considered (SPL = 134 and 137 dB), the flat panel experiences the largest strains while the most curved shell experiences the lowest strain.

In order to investigate the correlation between RMS (W_{max}/h) presented in Table 5.13, and RMS (ε_{max}), Table 5.18 presents statistical strain information.

Table 5.18 Statistics of the Panel Center Maximum Strain for (0/90) Simply Supported Cylindrical Shell of R_x = 75 in.

SPL dB	RMS (ε_{max}) x 10^{-3}	Mean x 10^{-4}	Variance x 10^{-4}	Skewness	Kurtosis
90	0.0214	0.0005	0.0185	0.0762	-0.1619
100	0.0626	0.0051	0.0601	0.1121	-0.1041
110	0.1385	0.0468	0.2418	0.2226	0.4091
120	0.3136	0.1666	1.7556	-0.3656	0.8145
125	0.4430	0.3719	3.0930	-0.6763	1.5445
128	0.5048	-0.1435	4.5884	-1.1241	1.8170
131	0.6456	-2.1583	8.3670	-1.2886	1.5660
134	0.7738	-5.3593	11.1809	-0.5436	-0.2876
137	0.8914	-8.4063	14.0605	-0.2337	-0.7527

All four statistical moments (mean, variance, skewness and kurtosis) exhibit very similar trendlines comparing deflection with strain.

Small and large amplitude strain response characteristics are presented in Figures 5.20a and 5.20b, respectively, with time histories, PSD, and PDF plots. The six lowest modes retained in the analysis are clearly seen on the PSD plot corresponding to low levels of excitation pressure. For higher excitation pressures there is only one broadened peak observed, and it moves toward higher frequencies with respect to the fundamental linear frequency. In the PDF plots, it is observed that both small- and large-amplitude responses reveal non-Gaussian characteristics.

Exploring the previously studied thermal case, in terms of deflection, shown in Figures 5.16 to 5.18 and presented in Section 5.2.2.1, the maximum strain RMS (ε_{max}) are presented in Table 5.19. At room temperature the maximum strain RMS (ε_{max}) occurs at x = 0 in., y = 7.5 in. and x = 10 in., y = 7.5 in. (at the midpoint on the straight edge of the panel). Location of the RMS (ε_{max}) at ΔT = 180 °F and high excitation pressure is the same, but at ΔT = 180 °F and low excitation pressure RMS (p) of up to 0.22 psi the maximum strain occurs at x = 5 in., y = 0 in. and x = 5 in., y = 15 in. (at the midpoint on the curved edge of the panel). At low to moderate levels of excitation pressure, random oscillation due to acoustic load is of small amplitude, and thermal deflection has a dominant role in the way the panel deforms. However, as the excitation pressure increases it overwhelms thermal static deflection and maximum strain change locations. At this point it is important to realize that even within such a small structural component like a single surface panel there can be more than one location of probable origin for a fatigue failure.

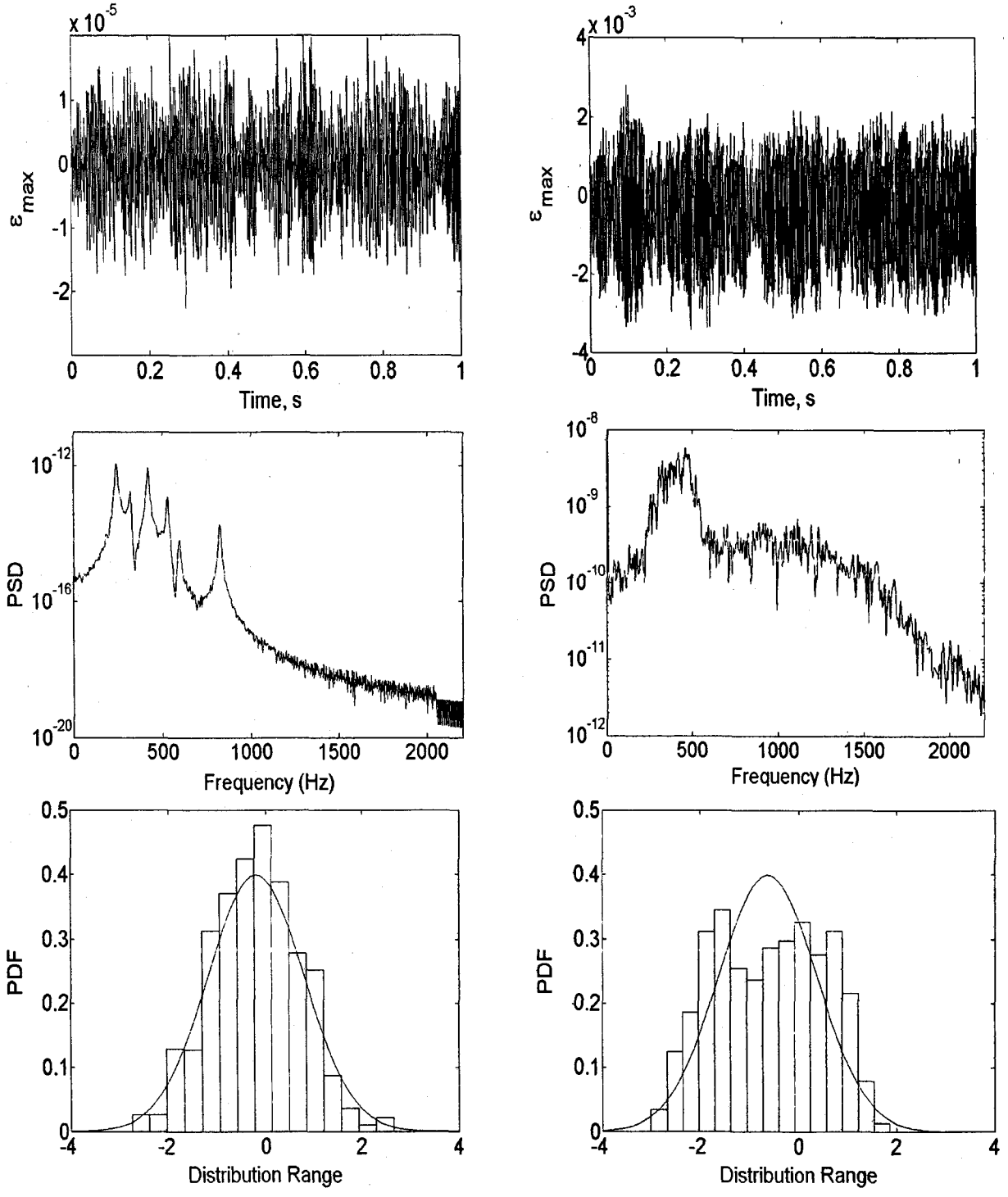

Figure 5.20 Strain Response of (0/90) Graphite-epoxy Simply Supported Cylindrical Panel of R_x = 150 in., (a) SPL=90 dB, (b) SPL=137 dB

Table 5.19 Maximum Strain RMS (ε_{max}) for Clamped Cylindrical Shell of R_x = 75 in. at Room and Elevated Temperature Raise of ΔT = 180 °F (100 °C) at SPL of 90, 120, 125 and 137 dB

SPL dB	ΔT °F	RMS (ε_{max}) x 10^{-3}	Location of RMS (ε_{max})
90	0	0.0324	x = 0 in., y = 7.5 in. and x = 0 in., y = 7.5 in.
	180	0.1410	x = 5 in., y = 0 in. and x = 5 in., y = 15 in.
120	0	0.3463	x = 0 in., y = 7.5 in. and x = 0 in., y = 7.5 in.
	180	0.4527	x = 5 in., y = 0 in. and x = 5 in., y = 15 in.
125	0	0.4598	x = 0 in., y = 7.5 in. and x = 0 in., y = 7.5 in.
	180	0.5938	
137	0	0.9187	x = 0 in., y = 7.5 in. and x = 0 in., y = 7.5 in.
	180	1.0307	

The differences in strain characteristics for small and large amplitude response at room temperature, and at uniform ΔT = 180 °F are presented in Figures 5.21 and 5.22, respectively. Six peaks can be easily identified at the low level excitation pressure (when thermal factor is not involved). For the same excitation pressure, but when the panel is heated, only 4 modes are clearly visible. The first mode (1,1) and the sixth mode (3,5) are suppressed, as was demonstrated previously in Figure 5.18a for the panel central deflection. At high levels of excitation pressure, only one broadened peak is observed for the room- and elevated- temperature environments. At elevated temperature however, the peak is "washed out" over a wider range of frequencies and its magnitude is higher.

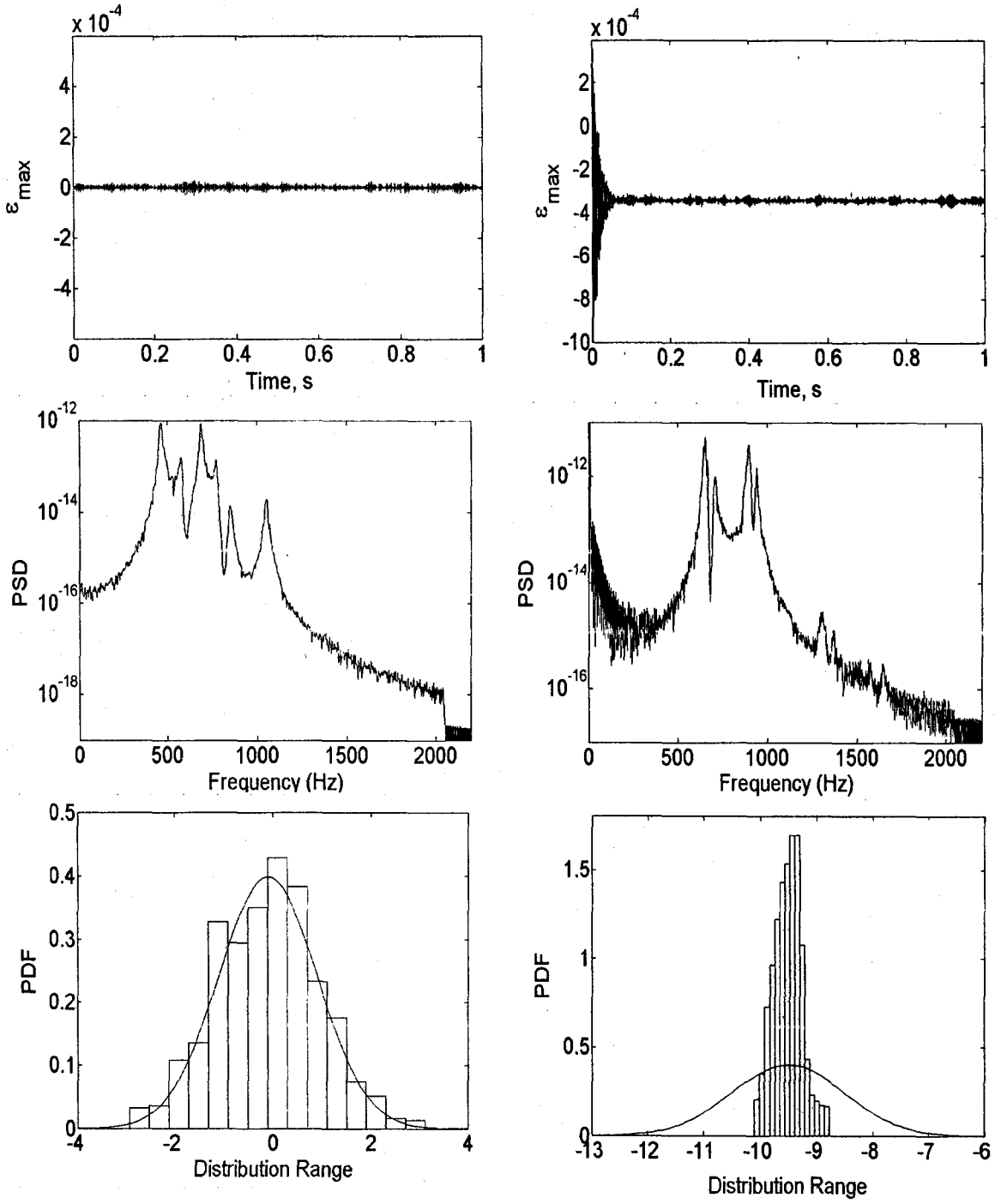

Figure 5.21 RMS (ε_{max}) of (0/90) Graphite-epoxy Clamped Cylindrical Panel of R_x = 75 in. at SPL = 90 dB, (a) ΔT=0, (b) ΔT=180 °F (100 °C)

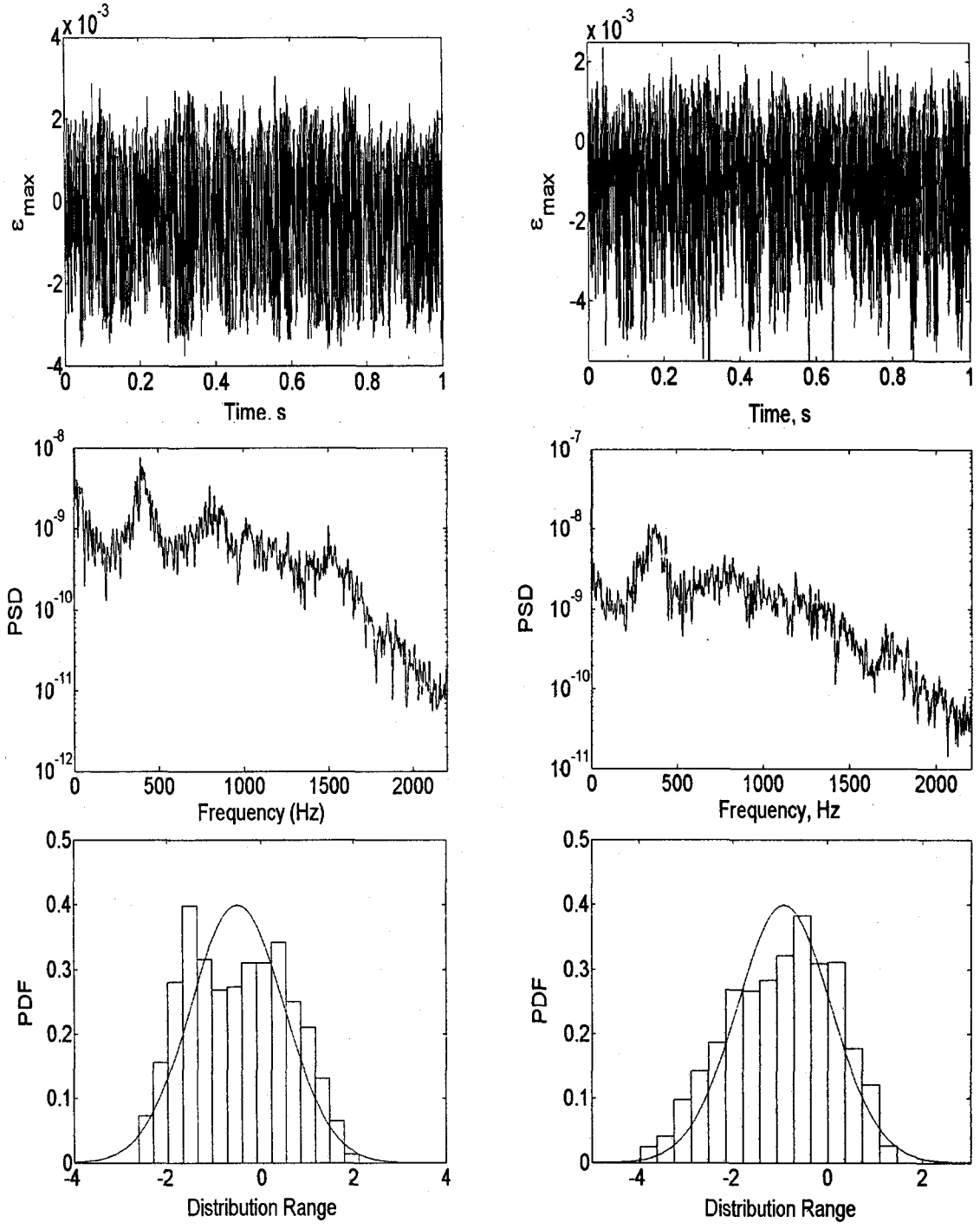

Figure 5.22 RMS (ε_{max}) of (0/90) Graphite-epoxy Clamped Cylindrical Panel of R_x = 75 in. at SPL = 137 dB, (a) ΔT=0, (b) ΔT=180 °F (100 °C)

A crucial step in fatigue life prediction is associated with the peak counting process. A comparison of the RFC method with the PTVC (simple max-min counting) is presented in Figure 5.23a and 5.23b, respectively, for low and high levels of excitation pressure. The influence of the temperature increase on the peak distribution is presented in Figure 5.24. Additionally, one case with a pronounced softening response characteristic is presented in Figure 5.25.

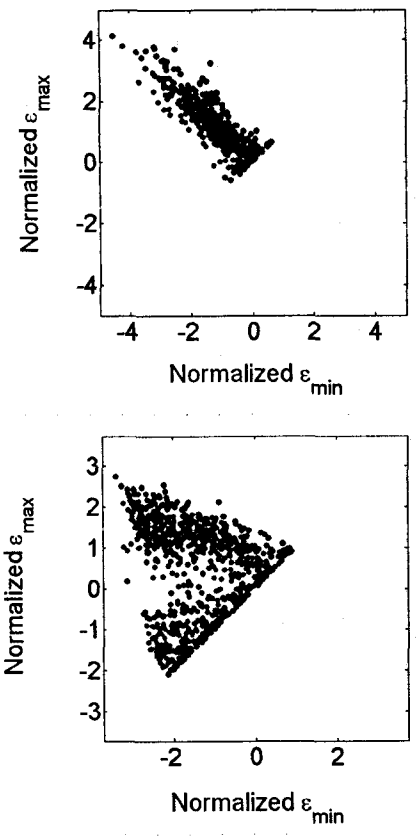

Figure 5.23a RFC for Clamped (0/90) Cylindrical Shell of R_x = 75 in. at Room Temperature and SPL = 90 dB (Top), and 137 dB (Bottom)

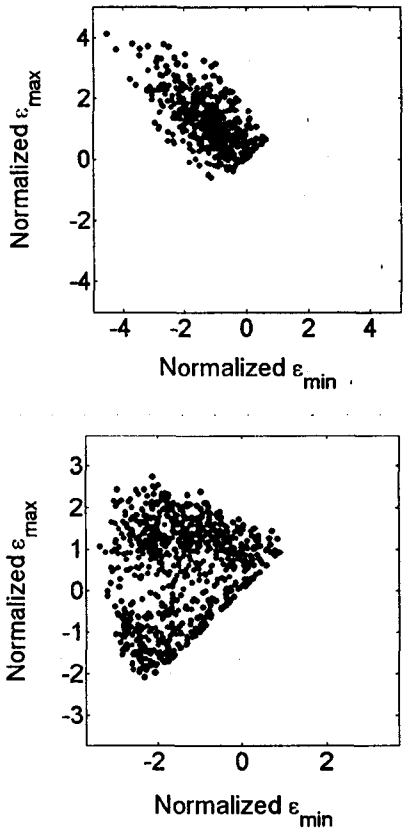

Figure 5.23b PTVC for Clamped (0/90) Cylindrical Shell of R_x = 75 in. at Room Temperature and SPL = 90 dB (Top), and 137 dB (Bottom)

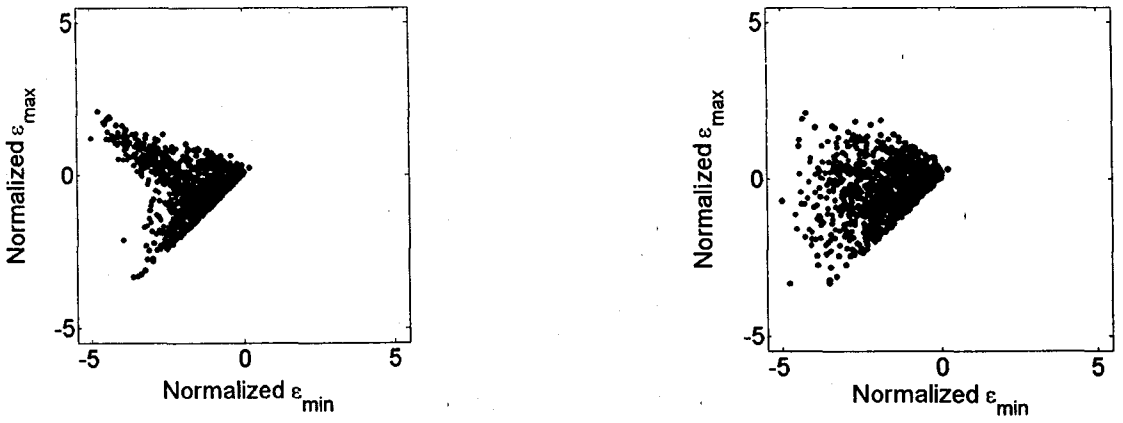

Figure 5.24 Peak Counting for Clamped (0/90) Cylindrical Shell of $R_x = 75$ in. at $\Delta T = 180°F$ (100°C) and SPL = 131 dB (a) RFC, (b) PTVC

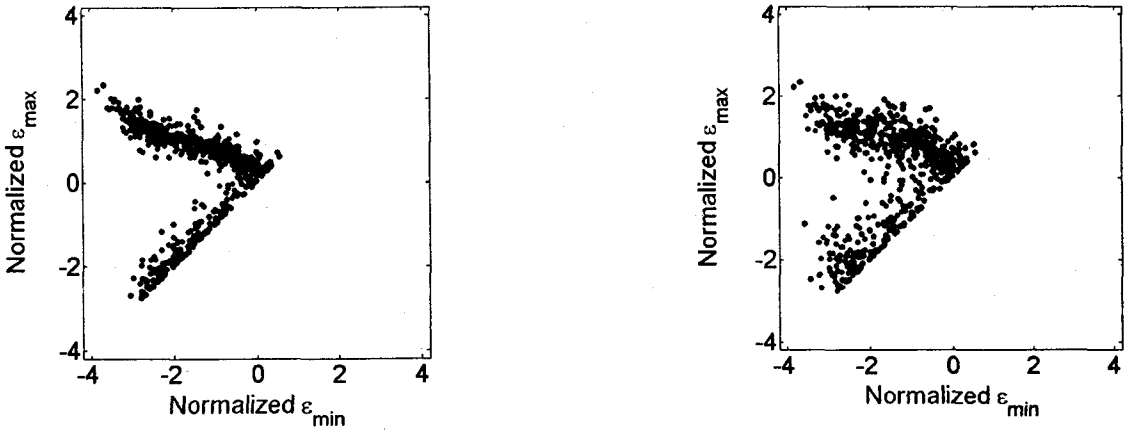

Figure 5.25 Peak Counting for Simply Supported (0/90) Cylindrical Shell of $R_x = 75$ in. at Room Temperature and SPL = 137 dB (a) RFC, (b) PTVC

As the response amplitude becomes larger, a broadened min-max distribution is observed. It is clearly seen that low amplitude vibration results in a narrowband peak distribution (along the anti-diagonal of the min-max matrix – see the upper plots of Fig.

5.23), while large amplitude vibration in the broadband distribution (along both the anti-diagonal and diagonal of the min-max matrix – see the bottom plots of Fig. 5.23). For the case of a heated panel (Figure 5.24) it is seen that the cloud of peaks is shifted towards the left bottom corner of the matrix as a result of compression introduced by thermal expansion. Figure 5.25 presents the peak counting for simply supported shell with (0/90) lamination and radius R_x = 75 in., which is the one with pronounced softening response characteristics. It is noticeable that the anti-diagonal data points in the min-max matrix are skewed. For each case presented in Figures 5.23 to 5.25 it is concluded that PTVC always results in a broader peak distribution in comparison with RFC.

The probability of up-crossing is also presented in Figures 5.26a and 5.26b for low and high levels of excitation pressure, respectively.

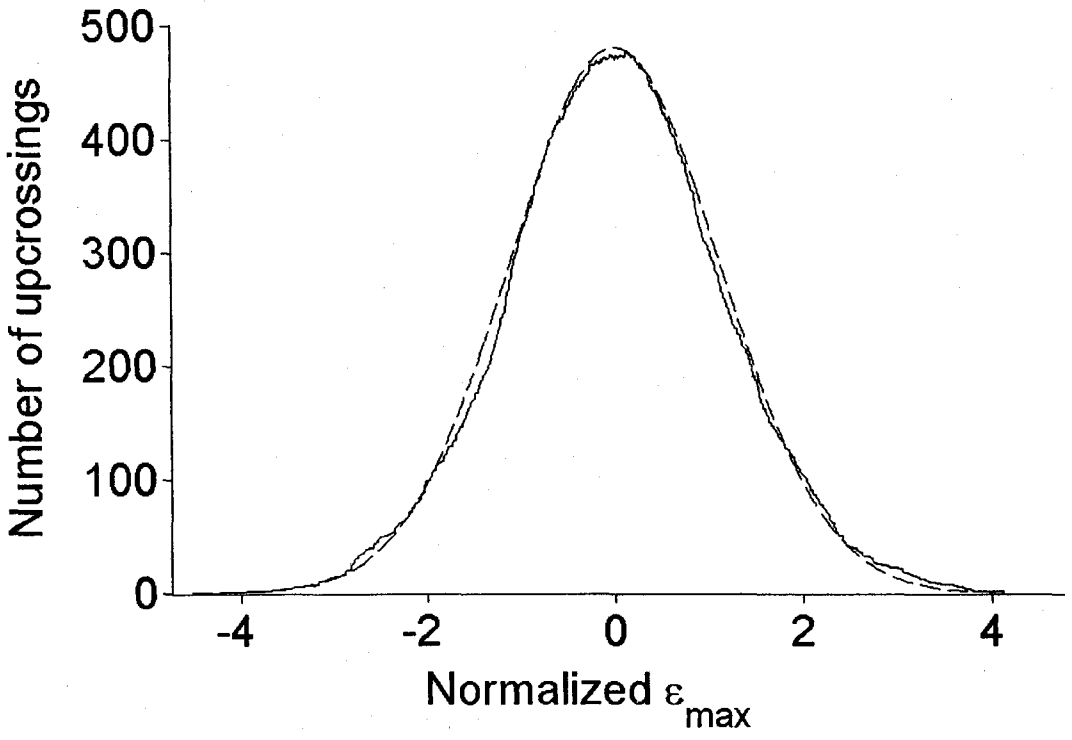

Figure 5.26a Probability of Up-crossing per 1 Second for Clamped (0/90) Cylindrical Shell of R_x = 75 in. at SPL = 90 dB (Dashed Line – Gaussian Distribution)

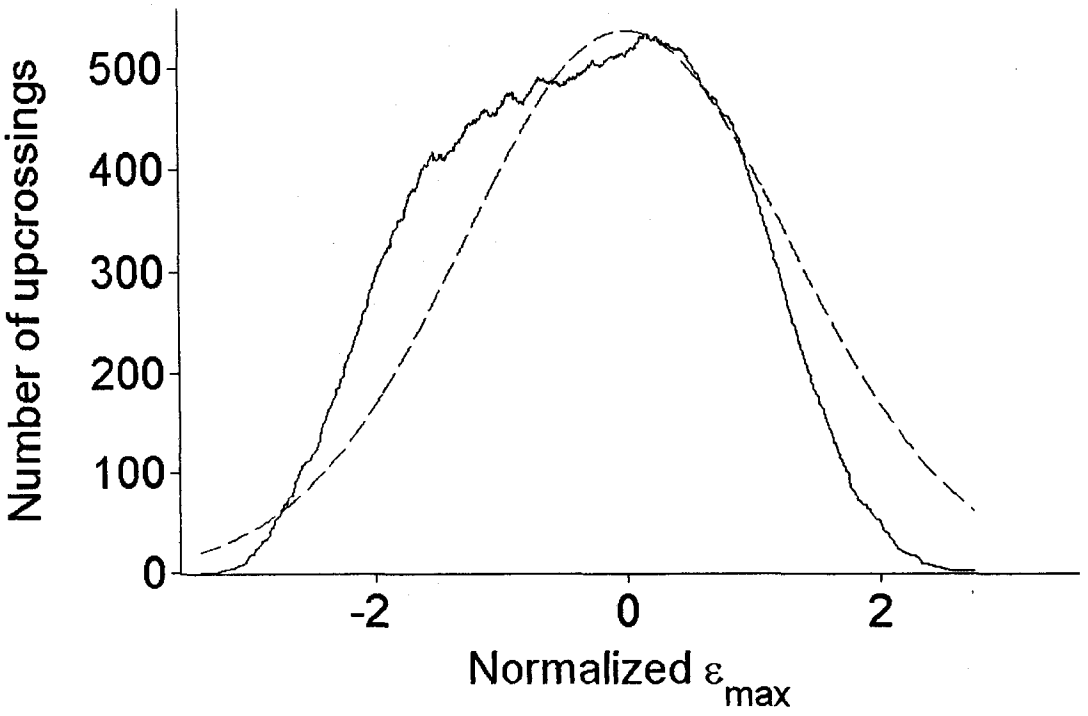

Figure 5.26b Probability of Up-crossing per 1 Second for Clamped (0/90) Cylindrical Shell of R_x = 75 in. at SPL = 137 dB (Dashed Line – Gaussian Distribution)

Probability of up-crossing is found to be Gaussian at the low excitation pressure level, but departures from the normal distribution as the excitation pressure increases.

Fatigue life for a variety of panel curvatures and excitation pressure levels for simply supported boundary conditions are presented in Table 5.20. A typical aircraft/spacecraft is usually designed to last for 25 to 30 years. Therefore fatigue life having cycle limits larger than 2.5 x 10^5 hours is considered to be "infinite" and consequently is of academic interest only. Nevertheless, some valuable conclusions can be drawn from the results presented. Based on the particular configurations of the panels presented in Table 5.20, it is seen that below SPL of 120 dB, sonic fatigue failure would not occur. Above this excitation pressure level it can be crudely estimated that doubling

the energy carried by the excitation spectrum (equivalent to SPL increase by 3 dB) the fatigue life is reduced by one order. It is generally observed that for lower levels of excitation pressure less curved panels will have longer fatigue lives. On the other hand, as the excitation pressure level increases, more curved panels perform better with respect to fatigue life. The curvature of a skin panel however is rarely a design freedom, since it is a result of aerodynamic and structural airframe design, as well as payload capacity. Therefore the focus and opportunity for optimization is seen to be shifted towards lamination stacking optimization.

Table 5.20 Fatigue Life (hrs.) for (0/90) Simply Supported Cylindrical Shells of Different Radii

SPL dB	$R_x = \infty$ in.	$R_x = 150$ in.	$R_x = 75$ in.
90	4.8152×10^{27}	3.1447×10^{22}	4.1079×10^{17}
100	3.5429×10^{22}	2.6233×10^{17}	2.6389×10^{13}
110	1.4653×10^{16}	7.4665×10^{11}	1.4349×10^{9}
120	1.6989×10^{7}	1.7103×10^{5}	3.6087×10^{5}
125	77,909	4,106	10,591
128	1,684	781	1,623
131	220	210	284
134	2.24	25.4	35.1
137	0.285	5.69	5.86

Since the influence of lamination stacking on fatigue estimation was obtained for both simulated white noise and microphone in-flight recorded data, the results for varying laminations are presented in the next Section (5.2.3.2).

5.2.3.2 Microphone In-flight Recorded Pressure Fluctuation Versus White Noise

The effect of lamination on RMS (ε_{max}) is presented in Table 5.21. It is seen that antisymmetrical lamination stacking (90/0) yields small strains for both types of random pressure fluctuations. The highest strain is obtained for a mirror stacking of (0/90) that previously was found resulting in the softening characteristics. Relatively similar solutions (difference of 1.8 %) for in-flight recorded and simulated pressure fluctuations were found only for the (90/0) panel. Panel of (0/90) stacking exhibits a substantial influence from pressure fluctuation type (11.8 %).

Table 5.21 Effect of Lamination on Random Response RMS (ε_{max}) x 10^{-3} for Simply Supported Shallow Shell of R_x = 75 in.

	(0/90)	(90/0)
White Noise	0.6272	0.5484
In-flight Data	0.7111	0.5582

The effect of temperature increase on RMS (ε_{max}) is presented in Table 5.22. For both room temperature and ΔT = 180 °F, large differences are found when comparing

responses from simulated and in-flight recorded pressure fluctuation. The differences in RMS (ε_{max}) are equal 10.1% and 6.6% for $\Delta T = 0$ and $\Delta T = 180°F$, respectively.

Table 5.22 Effect of Uniformly Distributed Temperature on Random Response RMS (ε_{max}) x 10^{-3} for Clamped (0/90) Shallow Shell of $R_x = 75$ in.

	$\Delta T = 0$	$\Delta T = 180°F$
White Noise	0.7494	0.8553
In-flight Data	0.8339	0.9158

Fatigue life estimates obtained for in-flight recorded pressure fluctuations and the equivalent truncated white noise are presented in Table 5.23.

Table 5.23 Comparison of Fatigue Life (hrs.) for In-flight and Simulated Pressure Fluctuations for Shallow Shells of $R_x = 75$ in.

Boundary Conditions	Lamination	Temperature Increase, °F	In-flight Data	Equivalent White Noise SPL = 129.901 dB
SS	(0/90)	0	29.2	321
SS	(90/0)	0	809	869
CL	(0/90)	0	3.29	5.52
CL	(0/90)	180	0.259	2.15

Fatigue life estimates differ substantially between white noise and microphone recorded in-flight pressure fluctuations. For all four configurations studied fatigue life calculated for in-flight pressure fluctuations was shorter than for the white noise analog. The most severe differences in fatigue estimates occurred for simply supported and clamped panels at room temperature and (0/90) lamination stacking, when their magnitudes were of order of one. The panel configuration that resulted in similar fatigue life estimates for simulated and in-flight measured pressure fluctuations was the simply supported panel of (90/0) lamination. This panel configuration was found previously to yield the smallest RMS strains. The potential for fatigue life extension can be exploited via proper stacking optimization can be appreciated by comparing results for simply supported panels. Fatigue lives for (0/90) and (90/0) lamination stacking differ 2.7x when simulated white noise was used to excite the structure, and by one order when in-flight recorded random pressure fluctuation was applied.

6. Conclusions

6.1 Free Vibration

The inplane inertia effect and coupling between bending and inplane modes play an important role in the large amplitude response of shallow shell panels. Analytical solutions fail to include these factors. This work has shown that the ratio between bending and inplane displacement in the linear case does not extend to nonlinear behavior due to the von Karman type nonlinearity. Therefore expressing the nonlinear system response in terms of linear coupled bending-inplane modes, that retains a fixed relation between the bending and inplane parts of the eigenvectors acts as a constraint on the system, introducing an excessive stiffening behavior. Also, the overstiff response of the formulation in linearly coupled bending-inplane modes may be due to the selected subset of modes and further investigation in this area is needed.

From the examples studied, it is concluded that inplane inertia may give completely different characteristics (hard- or soft-spring), while including multiple modes improves the accuracy of the nonlinear frequency estimates.

Flexibility of enforcing complicated boundary conditions and non-rectangular geometries of the panel promote the finite element approach with transformation into modal degrees of freedom as an essential tool, not only for random response[107] and sonic fatigue[108], but also for a variety of other surface skin panels response problems,[109] including flutter,[110] large thermal deflections[98,99] and even configurations with embedded smart materials, like piezoelectrics[111] or shape memory alloys.[112]

Since classical analytical methods fail to address inplane inertia, further investigation is needed in order to study its influence. Possible methods that can be used include:[113]

- more exhaustive verification by FE method in structural degrees of freedom,
- pseudo-analytical solutions with scaled inplane modes estimated by linear FE solutions and incorporated into a Galerkin procedure,
- experimental work.

6.2 Random Response and Fatigue Life

The multimode finite element large deflection formulation with transformation into modal coordinates for the shallow shell response subjected to combined thermal and random pressure loads was developed. Several cases were studied showing the influence of curvature, lamination sequence, boundary conditions and temperature change on the random response of shallow shells, with a primary focus on hardening vs. softening behavior. Modal convergence was sought and modal participation was determined. Statistics of the response were also determined and presented. Factors contributing to both softening and hardening response characteristics were determined and discussed. The concept of under-integration was used to calculate strains. The Rainflow Counting Method and S-N curves were combined by means of damage accumulation theory to estimate fatigue life. Results for simulated truncated white noise were obtained and compared with those calculated from in-flight recorded pressure fluctuations. Since only very short recordings of in-flight measured data were available, this work did not attempt to estimate random response or fatigue life for any particular aircraft design. The sole

intent here was to show, that white noise generated using similarity conditions based on integration of the power spectral density characteristic might be too simplistic in modeling accurately the excitation applied to an actual aerospace structure.

The cases studied in this work allow forming the following conclusions:

- For the same level of excitation pressure more curved panels yield smaller RMS (W_{max}/h) compared to those, which are more flat;

- The above conclusion does not extend into RMS (ε_{max}) behavior;

- For the same level of excitation pressure and the same panel dimensions, clamped boundary conditions result in shorter fatigue life compared to simply supported boundary conditions;

- Elevated thermal environment can significantly reduce fatigue life;

- Lamination stacking sequence has a substantial impact on the random response characteristics and fatigue life estimates. Lamination (90/0) compared to (0/90) yields smaller deflections and strains, and longer fatigue life;

Based on the experience built upon previous work regarding isotropic and symmetrically laminated composite flat plates, it was thought that linear dynamic response analysis would always yield conservative solutions. The softening characteristics of the dynamic response of shallow shell panels challenged this conclusion and the linear approach cannot be assumed always to result in over-design.

In the area of large amplitude random vibration, good agreement is not found between experimental and analytical work. The S-N curves being used for fatigue life estimation are based on experiments that were conducted either for pure bending or pure axial loads, as represented in Figures 6.1a and 6.1b, respectively.

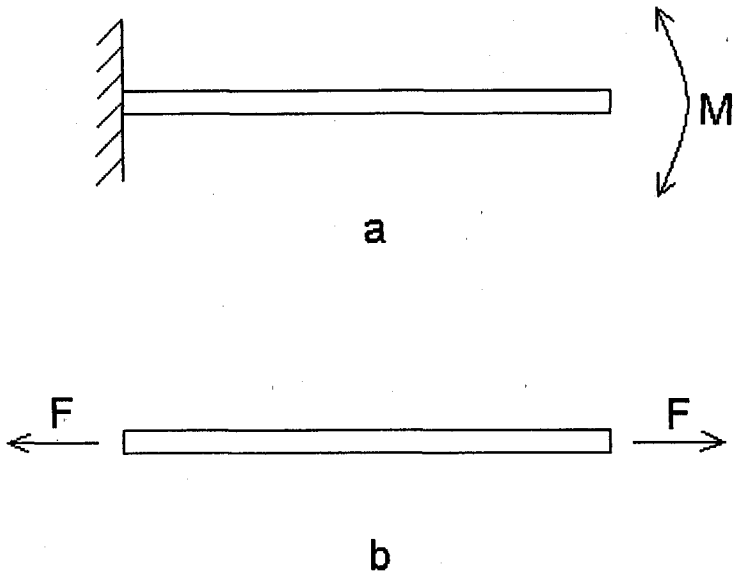

Figure 6.1 S-N curve estimation testing, (a) bending loads, (b) axial loads

The real state of strains however is much more complex and involves both types of loads – namely inplane and bending. Moreover, the relative contribution of the bending and inplane components to the total strain changes, as the amplitude of vibration and thermal static deflection change.[109] On the other hand future higher fidelity computational models should consider imperfections of curved panel geometry, non-uniform temperature distribution over the panel surface, nonlinear damping modeling, and also address optimal selection of modes used in the process of modal reduction. Therefore further research and development of both computational and experimental methods appear to be necessary in order to gain better confidence in results being obtained.

REFERENCES

[1] Leissa, A. W., "Vibration of Shells," NASA SP-288, Washington DC, 1973.

[2] Kraus, H., *Thin Elastic Shells*, John Wiley & Sons, Inc., New York, 1967.

[3] Libai, A., and Simmonds, J. G., *The Nonlinear Theory of Elastic Shells*, Cambridge University Press, Cambridge, UK, 1998, 2nd Edition.

[4] Liew, K. M., Lim, C. W., and Kitipornchai, S., "Vibration of shallow shells: A review with bibliography," *Applied Mechanics Review*, Vol. 50, No. 8, 1997, pp. 431-444.

[5] Cummings, E. A., "Large amplitude vibration and response of curved panels," *AIAA Journal*, Vol. 2, April 1964, pp. 709-716.

[6] Leissa, A. W., and Kadi, A. S., "Curvature effects on shallow shell vibrations," *Journal of Sound and Vibration*, Vol. 16, February 1971, pp. 173-187.

[7] Hui, D., "Influence of geometric imperfections and in-plane constraints on nonlinear vibrations of simply supported cylindrical panels," *Journal of Applied Mechanics*, Vol. 51, June 1984, pp. 383-390.

[8] Fu, Y. M., and Chia, C. Y., "Multi-mode non-linear vibration and postbuckling of anti-symmetric imperfect angle-ply cylindrical thick panels," *International Journal of Non-Linear Mechanics*, Vol. 24, No. 5, 1989, pp. 365-381.

[9] Raouf, R. A., and Palazotto, A. N., "On the non-linear free vibration of curved orthotropic panels," *International Journal of Non-Linear Mechanics*, Vol. 29, No. 4, 1994, pp. 507-514.

[10] Kobayashi, Y., and Leissa, A. W., "Large amplitude free vibration of thick shallow shells supported by shear diaphragms," *Journal of Non-Linear Mechanics*, Vol. 30, No. 1, 1995, pp. 57-66.

[11] Shin, D. K., "Large amplitude free vibration behavior of doubly curved shallow open shells with simply-supported edges," *Computers and Structures*, Vol. 62, No. 1, 1997, pp. 35-49.

[12] Abe, A., Kobayashi, Y., and Yamada, G., "Nonlinear vibration characteristics of clamped laminated shallow shells," *Journal of Sound and Vibration*, Vol. 234, No. 3, 2000, pp. 405-426.

[13] Tamura, H., and Matsuzaki, K., "Numerical scheme and program for the solution and stability analysis of a steady periodic vibration problem," *Japanese Society of Mechanical Engineering International Journal*, Vol. 39, No. 3, 1996, pp. 456-463.

[14] Pillai, S. R. R., and Rao, B. N., "Reinvestigation of non-linear vibrations of simply supported rectangular cross-ply plates," *Journal of Sound and Vibration*, Vol. 160, No. 1, 1993, pp. 1-6.

[15] Bhimaraddi, A., "Large amplitude vibrations of imperfect antisymmetric angle-ply laminated plates," *Journal of Sound and Vibration*, Vol. 162, No. 3, 1993, pp. 457-470.

[16] Alhazza, K. A., and Nayfeh, A. H., "Nonlinear vibrations of doubly-curved cross-ply shallow shells," AIAA-2001-1661, 42nd AIAA/ASME/ASCE/AHS/ASC Structures, Structural Dynamics, and Material Conference and Exhibit, Seattle, WA, April 2001.

[17] Shi, Y., Lee, R. Y. Y., and Mei, C., "Finite element method for non-linear free vibration of composite plates," *AIAA Journal*, Vol.35, No.1, 1995, pp. 159-166.

[18] Abdel-Motaglay, K., Chen, R., and Mei, C., "Nonlinear flutter of composite panels under yawed supersonic flow using finite elements," *AIAA Journal*, Vol. 37, No. 9, 1999, pp. 1025-1032.

[19] Bolotin, V., V., *Mechanics of Fatigue*, CRC Press, Washington, D.C., 1998.

[20] Niu, M., N., Y., *Airframe Structural Design*, Conmilit Press Ltd., 1988.

[21] Clarkson, B., L., "Review of Sonic Fatigue Technology," NASA Contractor Report 4587, Langley Research Center, VA, 1994.

[22] McGowan, P., R., "Structural Design for Acoustic Fatigue," ASD TDR 63-820, 1963.

[23] Ballentine, J., R., "Refinement of Sonic Fatigue Structural Design Criteria," AFFDL TR 67-156, 1967.

[24] Rudder, F., F., and Plumblee, H., E., "Sonic Fatigue Design Guide for Military Aircraft," AFFDL TR 74-112, 1974.

[25] Rudder, F., F., "Acoustic Fatigue Resistance of Internal Airframe Structures," AFFDL TR 71-107, 1971.

[26] Jacobson, M., J., "Sonic Fatigue Design Data for Bonded Aluminum Aircraft Structures," AFDDL TR 77-45, 1977.

[27] Thomson A., G., R., and Lambert, R., F., "Acoustic Fatigue Design Data," AGARD-AG-162-Part I, Neuilly n/Seine, France, 1969.

[28] Thomson A., G., R., and Lambert, R., F., "Acoustic Fatigue Design Data," AGARD-AG-162-Part II, Neuilly n/Seine, France, 1972.

[29] Thomson A., G., R.,and Lambert, R., F., "Acoustic Fatigue Design Data," AGARD-AG-162-Part III, Neuilly n/Seine, France, 1973.

[30] Thomson A., G., R., Lambert, R., F., "Acoustic Fatigue Design Data," AGARD-AG-162-Part IV, Neuilly n/Seine, France, 1975.

[31] Holehouse, I., "Sonic Fatigue Design Techniques for Advanced Composite Structures," AFWAL-TR-80-3019, Wright-Patterson AFB, OH, 1980.

[32] Arnold, R. R., and Vaicaitis, R. R., "Non-linear Response and Fatigue of Surface Panels by the Time Domain Monte Carlo Approach," WRDC-TR-90-3081, Wright-Patterson AFB, OH, 1990.

[33] Vaicaitis, R., and Kavallieratos, P., A., "Nonlinear Response of Composite Panels to random Excitation," 34th Structures, Structural Dynamics and Material Conference, La Jolla, CA, April 1993, pp. 1041-1049.

[34] Mei, C., and Chen, R., R., "Finite Element Nonlinear Random Response of Composite Panels of Arbitrary Shape to Acoustic and Thermal Loads Applied Simultaneously," WL-TR-97-3085, Wright-Patterson AFB, OH, 1997.

[35] Mei, C., Dhainaut, J. M., Duan, B., Spottswood, S. M. and Wolfe, H.F., "Non-linear Random Response of Composite Panels in an Elevated Thermal Environment," AFRL-VA-WP-TR-2000-3049, Wright-Patterson AFB, OH, 2000.

[36] Dhainaut, J. M., "Nonlinear Response and Fatigue Estimation of Surface Panels to White and Non-White Gaussian Random Excitation," Ph.D. Dissertation, Old Dominion University, Norfolk, VA, 2001.

[37] Lee, J., "Improving the Equivalent Linearization Technique for Stochastic Duffing Oscillators," *Journal of Sound and Vibration*, Vol. 186, No. 5, 1995, pp. 846-855.

[38] Rizzi, S. A., and Muravyov, A. A., "Improved Equivalent Linearization Implementations Using Nonlinear Stiffness Evaluation," NASA/TM-2001-210838, NASA Langley Research Center, Hampton, VA, March 2001.

[39] Rizzi, S. A., and Muravyov, A. A., "Equivalent Linearization Analysis of Geometrically Nonlinear Random Vibrations Using Commercial Finite Element Codes," NASA/TP-2002-211761, NASA Langley Research Center, Hampton, VA, July 2002.

[40] McEwan, M. I., Wright, J. R., Cooper, J. E., and Leung, A. Y. T., "A Finite Element / Modal Technique for Nonlinear Plate and Stiffened Panel Response Prediction," 42nd AIAA/ASME/ASCE/AHS/ASC Structures, Structural Dynamics, and Material Conference and Exhibit, AIAA-2001-1595, Seattle, WA, April 2001.

[41] Ng, C. F., and Clavenson, S. A., "High-Intensity Acoustic Tests of a Thermally Stressed Plate," *Journal of Aircraft*, Vol. 28, No. 4, 1991, pp. 275-281.

[42] Murphy, K. D., "Theoretical and Experimental Studies in Nonlinear Dynamics and Stability of Elastic Structures," Ph.D. Dissertation, Duke University, Durham, NC, 1994.

[43] Istenes, R., R., Rizzi, S., A., and Wolfe, H., F., "Experimental Nonlinear Random Vibration Results of Thermally Buckled Composite Panels," AIAA-95-1345-CP, 36th Structures, Structural Dynamics and Material Conference, New Orleans, LA, April 1995, pp. 1559-1568.

[44] Lighthill, M., J., "On Sound Generated Aerodynamically I; General Theory," Proceedings of Royal Society, A211, 1952, pp. 564-587.

[45] Lightill, M., J., "On Sound Generated Aerodynamically II: Turbulence as a Source of Sound," Proceeding of Royal Society, A222, 1953, pp. 1-32.

[46] Lansing, D., L., Drischler, T., J., Brown, J., S., and Mixson, J., S., "Dynamic Loading of Aircraft Surfaces Due to Jet Exhaust Imingment," AGARD CP-113, 1972.

[47] Scholton R., "Influence of The Ground on The Near Field Noise Levels of a Jet Supported V/STOL," AGARD CP-113, 1973.

[48] Coe, C., F., and Chyu, W., J., "Pressure Fluctuation Inputs and Response of Panels Underlying attached and Separated Supersonic Turbulent Boundary-Layers," NASA TM-X-62189, 1972.

[49] Coe, C., F., and Chyu, W., J., "Pressure Fluctuation Inputs and Response of Panels Underlying Attached and Separated Supersonic Turbulent Boundary Layers," AGARD CP-113, 1973.

[50] Bull, M., K., "Wall-Pressure Fluctuations Associated With Subsonic Turbulent Boundary-Layer Flow," *Journal of Fluid Mechanics*, Vol. 28, 1967, p. 719.

[51] Mixson, J., S., and Roussos, L., A., "Acoustic Fatigue: Overview of Activities at NASA Langley," NASA TM 89143, 1987.

[52] Thornton, E., A., *Thermal Structures for Aerospace Applications*, AIAA, Reston, VA, 1996.

[53] Van Driest, E., R., "The Problem of Aerodynamic Heating," *Aeronautical Engineering Review*, Vol. 15, No. 10, 1956, pp. 26-41.

[54] Truitt, R., W., *Fundamentals of Aerodynamic Heating*, Ronald Press, New York, 1960.

[55] Lee, J., "Large-Amplitude Plate Vibration in an Elevated Thermal Environment," *Applied Mechanics Reviews*, Vol. 46, Part 2, 1993, S242-254.

[56] Heldenfels, R., R., "Historical Perspectives on Thermostructural Research at the NASA Langley Aeronautical Laboratory from 1948 to 1985," NASA TM 83266, 1982.

[57] Stillwell, W., H., "X-15 Research Results with a Selected Bibliography," NASA SP-60, 1965.

[58] Staff of Johnson Space Center, "Space Shuttle," NASA SP-407, 1976.

[59] Caughey, T., K., "Derivation and Application of the FPK Equation to Discrete Nonlinear Dynamics Systems to White Random Excitation," *Journal Acoustic Society of America*, Vol. 35, November 1963, pp. 1683-1692.

[60] Soong, T., T., and Grigoriu, M., *Random Vibration of Mechanical and Structural Systems*, Prentice Hall, Englewood Cliffs, NJ, 1993.

[61] Lyon, R., H., "Response of Nonlinear String to Random Excitation," *Journal Acoustic Society of America*, Vol. 32, No. 8, 1960, pp. 953-960.

[62] Crandall, S., H., "Perturbation Techniques for Random Vibration of Nonlinear Systems," *Journal Acoustic Society of America*, Vol. 35, No. 11, 1963, pp. 1700-1705.

[63] Tung, C., C., Penzien, J., and Horonjeff, R., "Response of Supersonic Transport to Runway Roughness," *Journal of Airtransport Div.*, Proceedings ASCE, 1966, pp. 1-20.

[64] Nigam, N., C., *Introduction to Random Vibrations*, The MIT Press, Cambridge, MA, 1983.

[65] Iwan, W., D., and Yang, M., I., "Application of Statistical Linearization Techniques to Non-Linear Multi-Degree of Freedom Systems," *Journal of Applied Mechanics*, Vol. 39, June 1972, pp. 545-550.

[66] Booton, R., C., "The Analysis of Nonlinear Control System with Random Inputs," *Circuit Theory, IRE Transactions*, Vol. 1, 1954, pp. 32-34.

[67] Caughey, T., K., "Equivalent Linearization Techniques," *Journal Acoustic Society of America*, Vol. 35, No. 11, 1963, pp. 1706-1711.

[68] Atalik, T., S., and Utku, S., "Stochastic Linearization of Multi-Degree-of-Freedom Nonlinear Systems," *Earthquake Engineering and Structural Dynamics*, Vol. 4, 1976, pp. 411-420.

[69] Sakata, M., and Kimura, K., "Calculation of the Non-Stationary Mean Square Response of a Nonlinear System Subject to Non-White Excitation," *Journal of Sound and Vibration*, Vol. 73, 1980, pp. 333-343.

[70] Shinozuka, M., "Monte Carlo Solution of Structural Dynamics," *International Journal of Computers and Structures*, Vol. 2, 1972, pp. 855-874.

[71] Shinozuka, M., and Wen, Y., K., "Monte Carlo Solution of Nonlinear Vibration," *AIAA Journal*, Vol. 10, No. 1, 1972, pp. 37-40.

[72] Shinozuka, M., and Jan, D., M., "Digital Simulation of Random Processes and Its Applications," *Journal of Sound and Vibration*, Vol. 25, 1972, pp. 111-128.

[73] Vaicaitis, R., "Recent Advances of Time Domain Approach for Nonlinear Response and Sonic Fatigue," Proceedings 4th International Conference on Structural Dynamics, ISVR, University of Southampton, UK, July 1991, pp. 84-103.

[74] Vaicaitis, R., "Time Domain Approach for Nonlinear Response and Sonic Fatigue of NASP Thermal Protection Systems," Proceedings of 32nd Structures, Structural Dynamics and Material Conference, Baltimore, MD, April 1991, pp. 2685-2708.

[75] Lee, J., "Random Vibration of Thermally Buckled Plates: I. Zero Temperature Gradient Across the Plate Thickness," AIAA Progress Series in Aeronautics and Astronautics, edited by Thronton, E., A., 1995.

[76] Chen, P., C., Huang, C.-L., and Mignolet, M., P., "Fatigue Life Estimation of Thermally Buckled Composite Panels Subjected to Random Acoustic Loads," AIAA-2000-1748, 41st AIAA/ASME/ASCE/AHS Structures, Structural Dynamics, and Materials Conference, Atlanta, GA, April 2000.

[77] Dowling, N., E., "Fatigue Failure Predictions for Complicated Strain-Stress Histories," *Journal of Materials*, Vol. 7, 1972, pp. 71-87.

[78] Barrois, W., Ripley, E., L., *Fatigue of Aircraft Structure*, The Macmillan Company, NY, 1963.

[79] Matsushi, M., and Endo, T., "Fatigue of Metals Subject to Varying Stresses," Proceedings of Kyushu Branch of Japan Society of Mechanical Engineers, Fukuoka, 1968, pp. 37-40.

[80] Rychlik, I., "A New Definition of the Rainflow Counting Method," *International Journal of Fatigue*. Vol. 9, No. 7, 1987, pp. 119-121.

[81] Medsen, H., O., Krenk, S., and Lind, N., C., *Methods of Structural Safety*, Pretience Hall, Englewood Cliffs, NJ, 1986.

[82] Bolotin, V., V., *Prediction of Service Life Machines and Structures*, ASME Press, New York, 1989.

[83] Critchlow, W., J., McCulloch, A., J., Young, L., and Melcon, M., A., "An Engineering Evaluation of Methods for Prediction of Fatigue Life in Airframe Structures," ASD Technical Report 61-434, March 1963.

[84] Miner, M., A., "Cumulative Damage in Fatigue," *Journal of Applied Mechanics*, Vol. 12, 1945, pp. 159-164.

[85] Palmgren, A., "Die Lebensdaner von Kungellageru, Zeitshrift des Vereins Deutsher Ingenieure," Vol. 68, 1924, pp. 339-341.

[86] Degrieck, J., and Van Paepegem, W., "Fatigue Damage Modelling of Fibre-reinforced Composite Materials: Review," *Applied Mechanics Review*, Vol. 54, No. 4, 2001, pp. 279-300.

[87] Sarkani, S., "Nonlinear Damage Accumulation in Stochastic Fatigue of FRP Laminates," PMC2000-302, 8th ASCE Specialty Conference on Probabilistic Mechanics and Structural Reliability, Notre Dame, IN, July 2000.

[88] Ochi, M., K., and Ahn, K., "Probability Distribution Applicable to Non-Gaussian Random Process," *Probabilistic Enginnering Mechanics*, Vol. 9, 1994, pp. 255-264.

[89] Winterstein, S., R., "Nonlinear Vibration Models for Extremes and Fatigue," *Journal of Enginnering Mechanics*, ASCE, Vol. 114, No. 10, 1988, pp. 1772-1790.

[90] Dirlik, T., "Application of Computers in Fatigue Analysis," Ph.D. Dissertation, University of Warwick, 1985.

[91] Tessler, A., and Hughes, T., "A Three-Node Mindlin Plate Element With Improved Transverse Shear," *Computer Methods in Applied Mechanics and Engineering*, vol. 50, 1985, pp. 71-101.

[92] Tessler, A., "A C^0 – Anisoparametric Three-Node Shallow Shell Element," *Computer Methods in Applied Mechanics and Engineering*, vol. 50, 1985, pp.71-101.

[93] Wood, R.D., Schoefler, B., "Geometrically Nonlinear Analysis – A Correction of Finite Element Notation," *International Journal of Numerical Methods in Engineering*, Vol. 13, pp. 635-642, March 1978.

[94] Rektorys, K., *Survey of Applicable Mathematics*, Kluwer Academic Publishers, Dordrecht, The Netherlands, 1994.

[95] Bishop, N. W. N., and Sherratt, F. "Fatigue Life Prediction from Power Spectral Density Data. Part 1, Traditional Approaches and Part 2, Recent Developments," *Environmental Engineering*, Vol. 2, No. 1 and 2, 1989.

[96] Przekop, A., Azzouz, M. S., Guo, X., Mei, C., and Azrar, L., "Multimode Large Amplitude Free Vibrations of Shallow Shells Considering Inplane Inertia," AIAA-2003-1772, Proceedings of 44th AIAA/ASME/ASCE/AHS Structures, Structural Dynamics, and Materials Conference, Norfolk, VA, April 2003.

[97] Chen, R., R., and Mei, C., "Thermomechanical Buckling and Postbuckling of Composite Plates Using the MIN3 Elements," AD-Vol. 41/PVP-Vol. 293, Buckling and Postbuckling of Composite Structures, Iternational Mechanical Engineering Congress and Exposition, ASME, Chicago, IL, 1994, pp. 39-53.

[98] Shi, Y., and Mei, C., "Coexisting Thermal Postbuckling of Composite Plates with Initial Imperfection Using Finite Element Modal Method," AIAA 96-1467-CP, Proceedings 37th SDM Conference, Salt Lake City, UT, April 1996, pp. 1355-1362.

[99] Shi, Y., Lee, Y., Y., and Mei, C., "Thermal Postbuckling of Composite Plates Using the Finite Element Modal Coordinates Methods," *Journal of Thermal Stresses*, Vol. 22, 1999, pp. 595-614.

[100] Barlow, J., "Optimal Stress Locations in Finite Elements Models," *International Journal for Numerical Methods in Engineering*, Vol. 10, 1976, pp. 243-251.

[101] Cook, R., D., Malkus, D., S., and Plesha, M., E., "Concepts and Applications of Finite Element Analysis," John Wiley & Sons, New York, 1989.

[102] Rychlik, I., and Lindgren, G., "WAVE Analysis Toolbox – A Tutorial (Version 1.1)," University of Lund, Sweden, 1995, not published

[103] Bolotin, V., V., *Random Vibration of Elastic Systems*, Martinus – Nijhoff, Dordrecht, The Netherlands, 1984

[104] Chiang, C., K., "A Finite Element Large Deflection Multiple-Mode Random Response Analysis of Complex Panel with Initial Stress Subject to Acoustic Loading," Ph.D. Dissertation, Old Dominion University, Norfolk, VA, 1983.

[105] Abdel-Motagalay, K., Duan, B., and Mei, C., "Nonlinear Response of Composite Panels Under Combined Acoustic Excitation and Aerodynamic Pressure," *AIAA Journal*, Vol. 38, No. 9, September 2000.

[106] Paul, D. B., "Large Deflections of Clamped Rectangular Plates with Arbitrary Temperature Distributions," Vol. 1, AFWAL-TR-81-3003, Wright-Patterson AFB, OH, 1982.

[107] Przekop, A., Guo, X., Azzouz, M. S., and Mei, C., "Large Amplitude Response of Shallow Shells to Acoustic Excitation," 8th International Conference on Recent Advances in Structural Dynamics, Southampton, UK, July 2003.

[108] Przekop, A., Guo, X., Azzouz, M. S., and Mei, C., "Nonlinear Response and Fatigue of Shallow Shells to Acoustic Excitation Using Finite Element," AIAA-2003-1710, 44th AIAA/ASME/ASCE/AHS Structures, Structural Dynamics, and Materials Conference, Norfolk, VA, April 2003.

[109] Azzouz, M. S., Guo, X., Przekop, A., and Mei, C., "Comparison of PDE/Galerkin and Finite Element Modal Methods for Nonlinear Aerospace Structure," AIAA-2003-1856, 44th AIAA/ASME/ASCE/AHS Structures, Structural Dynamics, and Materials Conference, Norfolk, VA, April 2003.

[110] Azzouz, M. S., Przekop, A., Guo, X., and Mei, C., "Nonlinear Flutter of Curved Panels Under Yawed Supersonic Flow Using Finite Element," AIAA-2003-1516, 44th AIAA/ASME/ASCE/AHS Structures, Structural Dynamics, and Materials Conference, Norfolk, VA, April 2003.

[111] Azzouz, M. S., Przekop, A., Mei, C., and Azrar, L., "Finite Element Analysis of Rotating MFC/AFC Actuators," 6th Mechanics Congress of Tanger, Morocco, April 2003.

[112] Guo, X., Przekop, A., Mei, C., and Lee, Y. Y., "Thermal Buckling Suppression of Composite Laminates Using SMA for Supersonic Vehicle Application," Fifth International Congress on Thermal Stresses and Related Topics, Blacksburg, VA, June 2003.

[113] Mei, C., "Is the Inplane Inertia Important for Large Amplitude Vibration of Thin Plates and Shallow Shells?" proposal submitted to AFOSR, January 2003, unpublished.

Appendix A – Simulation of Truncated White Noise

The Matlab® code used to generate the white random pressure samples

```
NPT=2^14
Fmax=2048 %Hz
N=2048;
% use simload
SPL=129.901
[rdm,step]=simload(SPL,NPT,Fmax,N);

[n_rdm,nn] = size(rdm);
sum_psi = 0.0;
for i=1:n_rdm
   sum_psi = sum_psi + (rdm(i))^2;
end
rms_psi = sqrt(sum_psi/n_rdm)

figure(100)
t=0:step:(NPT-1)*step; t=t';
h = findobj(gca,'Type','patch');
set(h,'FaceColor','b','EdgeColor','w')
subplot(3,1,1)
plot(t,rdm)
set(gca,'FontSize',12)
xlabel('Time,sec')
ylabel('psi')
%   title('Random Noise Time history')
subplot(3,1,2)
[Pxx,freq] = pwelch(rdm,[],[],NPT,1/step);
%   plot(freq,10*log(Pxx))
semilogy(freq,Pxx)
set(gca,'FontSize',12)
xlabel('Frequency (Hz)')
ylabel('PSD (psi^2/Hz)')
axis([0 2200 1e-10 1e-2])

subplot(3,1,3)
range=-5.0:0.1:5.0;
RMS=sqrt(rdm'*rdm/length(rdm));
r_mean=mean(rdm);
var=sqrt(moment(rdm,2));
skew=moment(rdm,3)/var^3;
kurt=(moment(rdm,4)/var^4)-3;
```

```
p_gauss=1/sqrt(2*pi)*exp(-0.5*((range-r_mean)).^2);
psi_norm=rdm/std(rdm);
[n,psi_val]=hist(psi_norm,30);
minx=min(psi_val);
maxx=max(psi_val);
delta_x=(maxx-minx)/30;
for i=1:30
  pos_den(i)=n(i)/NPT/delta_x;
end
bar(psi_val,pos_den,1.0,'w')
hold on;
plot(range,p_gauss);
set(gca,'FontSize',12)
axis([-4 4 0 0.5]);
xlabel('Distribution Range (psi)')
ylabel('PDF (1/psi)')

Wpp_in=8.41438*10^(-18+SPL/10);
Wpp_ou=mean(Pxx(1:N));
disp('PSD Error in %')
Error=((Wpp_in-Wpp_ou)/Wpp_in)*100
```

```
function [y,DT]=simload(SPL,NPT,FMAX,N) %DT:step
NN=NPT*2;
X=zeros(NN,1);SP=zeros(3500,1);W=zeros(3500,1);
R=zeros(NN,1);

SPP=8.41438*power(10,-18+SPL/10);
DW=FMAX*2*pi/N;
SP(1:N+1)=SPP/pi/2;
W(1:N+1)=(0:N)*DW;
DT=N/FMAX/NPT;

ISEED=12357; %round(sum(10000*clock));
rand('state',ISEED);
R=rand(N,1);
j=sqrt(-1);
for i=2:N+1
   X(i)=sqrt(2*DW*SP(i))*exp(-R(i-1)*2*pi*j);
end

YY=fft(X,NPT);
y=real(YY(1:NPT));
```

Appendix B – WAVE Analysis Toolbox for Matlab®

B.1 – Turning Points Subroutine

```
function [tp, ind] = data2tp(x,h,wdef);
%DAT2TP Finds the turning points from data
%       optionally rainflowfiltered.
%
% CALL:  [tp ind] = dat2tp(x,h,wdef);
%
%       x  = two column data matrix with sampled times and values.
%
%       tp = a two column matrix with time and turning points.
%
%       ind = indices to the turning points in the original sequence.
%
%       h  = a threshold;
%            if  h<0, then  tp=x;
%            if  h=0, then  tp  is a sequence of turning points (default);
%            if  h>0, then all rainflow cycles with height smaller than
%                     h  are removed.
%
%     wdef = defines the type of wave. Possible options are
%               'mw' 'Mw' or 'none'. Default is 'none'.
%               If wdef='none' all rainflow filtered min and max
%               will be returned, otherwise only the rainflow filtered
%               min and max  which define a wave according to the
%               wave definition will be returned.
%
% Example:
%   x = load('sea.dat'); x1 = x(1:200,:);
%   tp = dat2tp(x1,0,'Mw'); tph = dat2tp(x1,0.3,'Mw');
%   plot(x1(:,1),x1(:,2),tp(:,1),tp(:,2),'ro',tph(:,1),tph(:,2),'k*')
%
%  See also: findcross, findrfc, tp2rfc, dat2tc

% Tested on: matlab 6.0, 5.3, 5.2, 5.1

% History:
% Revised by jr 03.04.2001
% - added example, updated info
% Modified by Per A. Brodtkorb 07.08.98
% This is a modified version which is about 20 to 30 times faster than
% the version of dat2tp in WAT (performance on a pentiumII 233 MHz
% with 32 MB ram and Matlab 5.0 under Linux). The reason is
```

```
% that this version does not save x to disk. Instead it passes
% the arguments directly to the executeable file.
% This new version is also more flexible. It is able to return the
% indices to the turningpoints
% (This is useful when determining the wave steepness etc...).


xn=x;

[n m]= size(xn);
if n<m
  b=m;m=n;n=b;
  xn=xn';
end

if n<2,
  error('The vector must have more than 2 elements!')
end

istime=1;

switch m
  case 1, x2=xn; istime=0;
  case 2, x2=xn(:,2);% dimension OK!
  otherwise, error('Wrong dimension of input! dim must be 2xN, 1xN, Nx2 or Nx1
')
end

if ((nargin<3) | isempty(wdef)),
  wdef='none';
end

if (nargin<2) | isempty(h),
   h=0;
end

if h<0
  tp=xn;
  ind=(1:n)';
  disp('Warning: h<0, the original data is returned')
  return
end

dx=diff(x2); %derivative
if 1, % finds indices to turningpoints
 ind=findcross(dx,0) + 1 ;
```

```
else % if findcross does not work use this

 %indices to local max/min + possible inflectionpoints
 %ind =find((((dx(1:(n-2))>=0) .* (dx(2:(n-1))<0)) |((dx(1:(n-2))<=0) .* (dx(2:(n%-
1)) > 0))) ) +1;

 ind=find(dx(2:(n-2))==0);
 for ix=1:length(ind),
   dx(ind(ix)+1)=dx(ind(ix));% avoiding inflection points
 end

 %indices to local max/min ( without inflectionpoints)
 ind =find( (((dx(1:(n-2))>=0) .* (dx(2:(n-1))<0)) | ...
    ((dx(1:(n-2))<=0) .* (dx(2:(n-1)) > 0))) ) + 1 ;
end
clear dx
if length(ind)<2,
  tp=[];
  return;
end

% In order to get the exact up-crossing intensity from rfc by
% mm2lc(tp2mm(rfc))  we have to add the indices
% to the last value (and also the first if the
% sequence of turning points does not start with a minimum).

if  x2(ind(1))>x2(ind(2)),
 % adds indices to  first and last value
 ind=[1; ind ;n];
else %adds index to the last value
 ind=[ind; n];
end

if h>0
   ind1=findrfc(x2(ind),h);
   ind=ind(ind1);
end


Nm=length(ind); % number of min and Max


switch wdef  % switch wdef
 case {'mw','Mw'},
   % make sure that the first is a Max if wdef == 'Mw'
   % or make sure that the first is a min if wdef == 'mw'
```

```
  if xor((xn(ind(1))>(xn(ind(2)))),strcmp(wdef,'Mw')),
    ind=ind(2:Nm);
    Nm=Nm-1;
  end

  % make sure the number of minima and Maxima are according to the wavedef.
  % i.e., make sure Nm=length(ind) is odd
  if ~(mod(Nm,2)), % if Nm is even do
    ind(Nm)=[];
    Nm=Nm-1;
  end

 case {'none'}% do nothing
 otherwise, error('Unknown wave definition')
end

tp=xn(ind,:);
```

B.2 – Crossing Rate Subroutine

```
function lc=tp2lc(tp,def,plotflag,sa)
%TP2LC  Calculates the number of upcrossings from the turning points.
%
% CALL: lc = tp2lc(TP,def,plotflag,sa);
%
%     lc = a two column matrix with levels and number of upcrossings. [mx2]
%     TP = the turning points.                    [nx2]
%
%    def = 1, only upcrossings.
%          2, upcrossings and maxima (default).
%          3, upcrossings, minima, and maxima.
%          4, upcrossings and minima.
%
%plotflag = 0, no plotting
%          1, plot the number of upcrossings overplotted
%             with Rice formula for the crossing intensity
%             for a Gaussian process (default).
%
%
%    sa  = standard deviation of the process
%          (Default estimates it from the number of upcrossings)
%
% See also: lcplot

% Tested  on Matlab  5.3
%
% History:
% Created by PJ (Pär Johannesson) 09-Jan-2000

% Check input arguments

ni = nargin;
no = nargout;
error(nargchk(1,4,ni));

if ni<2, def=[]; end
if ni<3, plotflag=[]; end
if ni<4, sa=[]; end

% Get min-max cycles
mM = tp2mm(tp);
% Get level crossings
%lc = cc2lc(mM,def,plotflag,sa);
lc = cc2lc(mM,def,0,sa);
```

B.3 – Rainflow Cycles Counting Subroutine

```
function  [RFC,RFC1,res,def] = tp2rfc(x,def,RFC0,res0)
%TP2RFC Finds the rainflow cycles from the sequence of turning points.
%
% CALL:  [RFC,RFC1,res] = tp2rfc(tp,def,RFC0,res0);
%                 RFC = tp2rfc(tp);
%
% Output:
%  RFC     = Rainflow cycles (residual included).      [N,2]/[N,4]
%  RFC1    = Rainflow cycles (without resudual).       [N1,2]/[N1,4]
%  res     = Residual.                                 [nres,1]/[nres,2]
%
% Input:
%  tp      = Turning points.                           [T,1]/[T,2]
%  def     = Choice of definition of rainflow cycles   [struct array]
%  def.res = Treatment of residual.
%          'up':   Count min-to-Max cycles,    (default)
%                  gives correct number of upcrossings.
%          'down': Count Max-to-min cycles,
%                  gives correct number of downcrossings.
%          'CS':   Cloormann/Seeger method,
%                  gives all closed hysteresis loops.
%                  This method is identical to the French AFNOR recommendation,
%                  and the ASTM standard (variant called simplified version).
%  def.time = 0: Don't store time of max and min. (default)
%           1: Store the time when the maxima and minima occured in columns 3-
4.
%  def.asymmetric = 0: gives the symmetric RFC (default),
%                 1: gives the asymmetric RFC (or From-To RFC), time order
between
%                    maximum and rainflow minimum is preserved.
%  RFC0    = Rainflow cycles (without resudual).       [N0,2]/[N0,4]
%  res0    = Residual.                                 [nres0,1]/[nres0,2]
%
% Calculates the rainflow cycles (RFC) for the sequence of turning points,
% by using the so-called 4-point algorithm.
%
% It is possible to split the signal into smaller parts, and calculate
% RFC part by part. It can be especially useful for long signals.
% We count the first part and for the second part we continue counting
% from previously counted 'RFC0' with residual 'res0':
%  [RFC1,RFC0,res0] = tp2rfc(tp(1:1000,:));      % Firts 1000 points
%  [RFC2] = tp2rfc(tp(1001:end,:),[],RFC0,res0); % Point 1001 to end
% This shall give the same result as (i.e. ARFC=ARFC2)
%  [RFC] = tp2rfc(tp);                           % Calculate all at once
```

```
%   sum(RFC~=RFC2)                          % Shall return  [0 0]
%
% This routine doesn't use MEX, Fortran or C codes, only matlab code.
%
% Example:
%   x = load('sea.dat'); tp=dat2tp(x);
%   RFC1=tp2rfc(tp);      % Default (min-to-Max cycles in residual)
%   ccplot(RFC1)
%   RFC2=tp2rfc(tp,'CS'); % Compare with AFNOR/ASTM standard
%   [I,J] = find(RFC1(:,1)~=RFC2(:,1) | RFC1(:,2)~=RFC2(:,2));
%   hold on,plot(RFC1(I,1),RFC1(I,2),'b+',RFC2(I,1),RFC2(I,2),'rx'), hold off
%
% See also: findrfc, dat2tp, rfcfilt, tp2arfc

% Further examples:
%   % Rainflow cycles with time
%   def.res='up'; def.time=1; % Store times
%   RFC=tp2rfc(tp,def); RFC(1:10,:), ccplot(RFC)
%
%   % For long signals it is possible to split the input in smaller parts
%   [dummy,RFC0,res0] = tp2rfc(dat2tp(x(1:5000,:)));     % First part
%   [RFC3] = tp2rfc(dat2tp(x(5001:end,:)),[],RFC0,res0); % Second part
%   % RFC3 shall be the same as RFC1. Check this!
%   ccplot(RFC1), hold on,plot(RFC3(:,1),RFC3(:,2),'r.'), hold off

% Tested  on Matlab  5.3
%
% History:
% Revised by PJ 26-Jul-2000
%   New format of def.
%   Added input 'RFC0' and 'res0'. New output 'RFC1' and 'res'
%   Now supports AFNOR and ASTM standards for rainflow counting.
% Created by PJ (Pär Johannesson) 2000-01-04
%   Uses same syntax as 'tp2rfc' in WAT

% Check input arguments
ni = nargin;
no = nargout;
error(nargchk(1,4,ni));

if ni < 2, def=[]; end
if ni < 3, RFC0=[]; end
if ni < 4, res0=[]; end

% Check input def
def0=def;
```

```
if ~isempty(def)
 if ischar(def)
  def.res = def0;
 end
end

% Set default values
if ~isfield(def,'res')
 def.res = 'up';
end
if ~isfield(def,'time')
 def.time = 0;
end
if ~isfield(def,'asymmetric')
 def.asymmetric = 0;
end

% Count rainflow cycles
if no<2
 ARFC = tp2arfc(x,def,[],res0);
else
 [ARFC,ARFC1,res] = tp2arfc(x,def,[],res0);
end

% Convert to symmetric RFC ?
if def.asymmetric == 0 % Symmetric rainflow cycles
 RFC = make_symmetric(ARFC);
else
 RFC = ARFC;
end

% Add previously counted cycles (if any)
if ~isempty(RFC0)
 RFC = [RFC0; RFC];
end

% Rainflow cycles without residual
if no>2,
 if def.asymmetric == 0 % Symmetric rainflow cycles
  RFC1 = make_symmetric(ARFC1);
 else
  RFC1 = ARFC1;
 end
 % Add previously counted cycles (if any)
 if ~isempty(RFC0)
  RFC1 = [RFC0; RFC1];
```

```
  end
end


function RFC = make_symmetric(ARFC)

  I = ARFC(:,1)>ARFC(:,2);
  [N,M]=size(ARFC);
  if M == 2 % No time
    J=1;
  else      % Time of occurances is stored in column 3:4
    J=[1 3];
  end
  RFC = ARFC;
  RFC(I,J) = ARFC(I,J+1);
  RFC(I,J+1) = ARFC(I,J);
```

B.4 – Peak Through Valley Counting Subroutine

```
function [mM,Mm] = tp2mm(tp)
% TP2MM Calculates min2Max and Max2min cycles from a sequence of turning
points
%
% CALL:  [mM,Mm] = tp2mm(TP);
%
%   mM  = a two column matrix with the min2Max count.
%   Mm  = a two column matrix with the Max2min count.
%   TP  = a two column matrix with the sequence of turning points.
%
% Example:
%   TP = dat2tp(x);
%   [mM,Mm] = tp2mm(TP);
%   ccplot(mM);
%
% See also: dat2tp, cc2cmat, ccplot

% Tested  on Matlab  5.3
%
% History:
% Updated by PJ 19-Oct-2000
%   Two versions existed (in 'onedim' and 'cycles')!
%   Removed version in 'onedim'
%   Now handles vectors
% Revised by PJ (Pär Johannesson) 01-Nov-1999
%   updated for WAFO
% Copied from WAT Ver. 1.2

[n m]= size(tp);
if n<m
  b=m;m=n;n=b;
  tp=tp';
end

if n<2,
  error('The vector must have more than 1 elements!')
end

switch m
  case {1, 2},  % dimension OK!
  otherwise,
    error('Wrong dimension of input! dim must be 2xN, 1xN, Nx2 or Nx1 ')
end
```

```
if tp(1,m)>tp(2,m)
  im = 2;
  iM = 1;
else
  im = 1;
  iM = 2;
end

% Delete first point if it is a maximum
%if tp(1,m)>tp(2,m)
%  tp = tp(2:n,:);
%  if tp(1,m)>tp(2,m)
%    error('tp  is not a sequence of turning points.')
%  end
%end

% Count min-max and max-min cycles
n=length(tp);
mM=[tp(im:2:n-1,m) tp(im+1:2:n,m)]; % min-max cycles
Mm=[tp(iM:2:n-1,m) tp(iM+1:2:n,m)]; % max-min cycles
```

B.5 – Damage and Fatigue Subroutine

```
function D=cc2dam(cc,beta,K)
% CC2DAM   Calculates the total Palmgren-Miner damage of a cycle count.
%
% CALL: D = cc2dam(cc,beta,K);
%
%   D    = Damage.                                        [1xm]
%
%   cc   = Cycle count with minima in column 1 and        [nx2]
%          maxima in column 2.
%   beta = Beta-values, material parameter.               [1xm]
%   K    = K-value, material parameter. (Optional, Default: 1) [1x1]
%
% The damage is calculated according to
%   D(i) = sum ( K * S^beta(i) ),  with  S = (max-min)/2
%
% Example:
%   x = load('sea.dat'); TP=dat2tp(x); RFC=tp2rfc(TP);
%   bv = 3:8;
%   D = cc2dam(RFC,bv); plot(bv,D,'x-')
%
% See also: cmat2dam

% Tested on Matlab 6.0
%
% History:
% Revised by PJ  01-Nov-1999
% - updated for WAFO
% Created by PJ (Pär Johannesson) 1997
%   from 'Toolbox: Rainflow Cycles for Switching Processes V.1.0'


% Check input and otput

ni = nargin;
no = nargout;
error(nargchk(2,3,ni));

if ni < 3
  K=[];
end

% Set default values

if isempty(K)
```

```
  K = 1;
end

% Calculate damage

amp = abs(cc(:,2)-cc(:,1))/2;

n=length(beta); D=zeros(1,n);
for i=1:n
  D(i)=K*sum(amp.^beta(i));
end
```

CIRRICULUM VITA
for
Adam Przekop

DEGREES:

Doctor of Philosophy (Aerospace Engineering), Old Dominion University, Norfolk, Virginia, August 2003.

Master of Science (Aeronautical Engineering), Warsaw University of Technology, Warsaw, Poland, January 1998.

PROFESSIONAL CHRONOLOGY:

National Institute of Aerospace, Hampton, Virginia, Staff Scientist, June 2003 – present

Old Dominion University, Department of Aerospace Engineering, Norfolk, Virginia, Research Assistant, August 2000 – May 2003.

Energoprojekt, Warsaw, Poland, Investment and Development Specialist, March 1999 – June 1999.

Budoprojekt – Stomil, Piastow, Poland, Senior Production and Sales Specialist, May 1998 – April 1999.

CONSULTING:

Hampton Data Services Ltd., Surbiton, Surrey, Great Britain, Geodata Software and Remote Data Capturing Specialist, July 1994 – August 2000

Institute of Aeronautics and Applied Mechanics, Warsaw, Poland, Project Engineer, July 1997 – July 1999, State Committee for Scientific Research Grant # 9 T12C 040 12.

ACTIVITIES:

"From Aeromodeling to Aviation" Foundation, (non-profit), Warsaw, Poland, Board Member, March 1997 – present.

Aircraft Composite Structures Development and Production Ltd., Warsaw, Poland, Intern, June 1997 – July 1997.

SCHOLARLY ACTIVITIES COMPLETED:

Przekop, A., Guo, X., Azzouz, M. S., Mei, C., Large Amplitude Response of Shallow Shells to Acoustic Excitation, 8th International Conference on Recent Advances in Structural Dynamics, Institute of Sound and Vibration Research, Southampton, UK, July 2003

Guo, X., Przekop, A., Mei, C., Lee, Y. Y., Thermal Buckling and Postbuckling Analysis of SMA Embedded Plates, 5th International Congress on Thermal Stresses and Related Topics, Virginia Tech, Blacksburg, VA, June 2003 (submitted to Journal of Thermal Stresses for publication)

Azzouz, M. S., Przekop, A., Mei, C., Azrar, L., Finite Element Analysis of Rotating MFC/AFC Actuators, The 6th Mechanics Congress of Tanger, Morocco, April 2003

Azzouz, M. S., Przekop, A., Guo, X., Mei, C., Nonlinear Flutter of Curved Panels Under Yawed Supersonic Flow Using Finite Element, AIAA-2003-1516, 44th AIAA/ASME/ASCE/AHS/ASC Structures, Structural Dynamics, and Materials Conference, Norfolk, VA, April 2003

Przekop, A., Guo, X., Azzouz, M. S., Mei, C., Nonlinear Response and Fatigue of Shallow Shells to Acoustic Excitation Using Finite Element, AIAA-2003-1710, 44th AIAA/ASME/ASCE/AHS/ASC Structures, Structural Dynamics, and Materials Conference, Norfolk, VA, April 2003

Przekop, A., Azzouz, M. S., Guo, X., Mei, C., Azrar, L., Multimode Large Amplitude Free Vibrations of Shallow Shells Considering Inplane Inertia, AIAA-2003-1772, 44th AIAA/ASME/ASCE/AHS/ASC Structures, Structural Dynamics, and Materials Conference, Norfolk, VA, April 2003 (accepted for publication in AIAA Journal)

Azzouz, M. S., Guo, X., Przekop, A., Mei, C., Comparison of PDE/Galerkin and Finite Element Modal Methods for Nonlinear Aerospace Structure, AIAA-2003-1856, 44th AIAA/ASME/ASCE/AHS/ASC Structures, Structural Dynamics, and Materials Conference, Norfolk, VA, April 2003

Przekop, A., Testing of the Influence of the Curvature of the Cylindrical Shell on the Vibration Characteristics, Report submitted in fulfillment of Research Skill requirement, Old Dominion University, Norfolk, VA, January 2002, *unpublished*

Goraj, Z., Przekop, A., Flight Dynamics Analysis of a Glider in Symmetrical Motion – The Case Study for PW-5, The Archive of Mechanical Engineering, Vol. XLVII, No. 3, Warsaw, Poland, 2000

Rodzewicz M., Przekop, A., Experimental Investigation of the Load Spectrum and Fatigue Tests of the PW-5 World Class Glider, Technical Soaring, Vol. XXIV, No. 1, January 2000 (presented at XXV OSTIV Congress, Bayreuth, Germany,1999)

Rodzewicz, M., Przekop, A., Study of Elasticity Changes of the Composite Shell Caused by Structural Discontinuities, Proceedings of XXXVIII Congress - Modeling in Mechanics, Warsaw, Poland, 1999, *in Polish*

Rodzewicz, M., Przekop, A., Szybilski, J., Research into Load Factor and the Fatigue Tests of the PW-5 World Class Glider, Proceedinds of 8th Mechanics in Aviation Congress "ML-VIII", Warsaw, Poland, 1998, *in Polish*